INFLUENCE OF SYMMETRY ENERGY ON MASS SYMMETRIC AND ASYMMETRIC HEAVY ION REACTIONS

A THESIS

submitted to the

THAPAR INSTITUTE OF ENGINEERING AND TECHNOLOGY, PATIALA

for the degree of

DOCTOR OF PHILOSOPHY

IN THE FACULTY OF SCIENCE

By

Amandeep Kaur

Regn. No. 901312002

SCHOOL OF PHYSICS AND MATERIALS SCIENCE

THAPAR INSTITUTE OF ENGINEERING AND TECHNOLOGY

PATIALA-147004, PUNJAB (INDIA)

Dedicated to

My Beloved Parents

THAPAR INSTITUTE
OF ENGINEERING & TECHNOLOGY
(Deemed to be University)

CANDIDATE'S DECLARATION

I hereby certify that the work which is being presented in this thesis entitled "**INFLUENCE OF SYMMETRY ENERGY ON MASS SYMMETRIC AND ASYMMETRIC HEAVY ION REACTIONS** " is partial fulfillment of the requirements for the award of degree of Doctor of Philosophy and submitted in the School of Physics and Materials Science, Thapar Institute of Engineering and Technology, Patiala, is an authentic record of my own work carried out during a period from July 2013 to July 2018 under the supervision of **Dr. Suneel Kumar**, Professor and Head, Department of Physics, University Institute of Sciences, Chandigarh University, Gharuan (Mohali), Punjab. The matter presented in this thesis has not been submitted by me in part or full for the award of any other degree in any other university or institute.

Amandeep

(Amandeep Kaur)

Regn. No. 901312002

This is to certify that the above statement made by the candidate is correct to the best of our knowledge.

Supervisor

S Kumar

Dr. Suneel Kumar
Professor and Head
Department of Physics
University Institute of Sciences
Chandigarh University, Gharuan (Mohali)
Punjab (India)

Date: 23-07-18

Administrative Supervisor

O P Pandey

Dr. O. P. Pandey
Senior Professor
School of Physics and Materials Science
TIET
Patiala, Punjab (India)

Acknowledgments

Firstly, I would like to express my sincere gratitude to my supervisor Dr. Suneel Kumar for the continuous support during my Ph.D study and related research, for his patience, motivation, and immense knowledge. His guidance helped me in all the time of research and writing of this thesis. I could not have imagined having a better advisor and mentor for my Ph.D study.

I would like to express my sincere gratitude to Prof. Prakash Gopalan, Director, Thapar University and Shri Gurbinder Singh, Registrar, Thapar University, Patiala. I am also thankful to Dr. O. P. Pandey, Dean of Research and Sponsored Projects who is also my administrative supervisor for his constant moral support to accomplish this task and providing the possible research facilities in various disciplines.

I will always be deeply indebted to Dr. Manoj K. Sharma, Professor and Head, School of Physics and Materials Science, Thapar University, Patiala, for providing all the necessary facilities in the department. I extend my sincere thanks to Prof. Kulbir Singh for his constant motivation. Besides my advisor, I would like to thank the rest of my thesis committee: Dr. Manoj Sharma, Dr. Alka Upadhaya, and Dr. A. K. Lal, for their insightful comments and encouragement, but also for the hard question which incented me to widen my research from various perspectives.

I highly appreciate my lab mates Kamaldeep, Dr. Kirandeep Sandhu, Navjot, Sangeeta, Shoaib, Neeraj, Jagroop and many other research scholars here at Thapar University for their pleasant company and for making this experience an enjoyable and memorable one. On a more personal note, I would like to express gratitude to my dearest friends Ms. Indu Gupta, Ms. Neetu Bansal, Ms. Chandanpreet Kaur, Mr. Harjot Singh Purewal, Dr. Pooja Singla and Ms. Anju Bala. They have been the essential supporters throughout this journey.

I do not really have words to express my gratitude towards my parents (Sdn. Manjeet Kaur and S. Balbir Singh). I might not be the person I am today without your unconditional love, support and inspiration. I am indebted to my parents for their time, efforts and belief in me.

Last but not the least, I would like to pay high regards to Saraswati the Goddess of

knowledge who gave me some intellect and wisdom to reach where I am today.

Amandeep

Date: 23-07-18

Patiala

(Amandeep Kaur)

List of Publications :

A. International/National Journals :

1. Analyzing Fragment Production in Mass-Asymmetric Reactions as a Function of Density Dependent Part of Symmetry Energy.
   Amandeep Kaur, Deepshikha, Karan Singh Vinayak and Suneel Kumar,
   Physics of Atomic Nuclei **79**, 474 (2016).

2. On the global and local nuclear stopping in mass asymmetric nuclear collisions using density-dependent symmetry energy.
   Amandeep Kaur and Suneel Kumar,
   Indian Journal of Physics, **91**, 1095 (2017)

3. Density and Temperature Evolution in Mass Asymmetric Reactions.
   Deepshikha, **Amandeep Kaur**, Karan Singh Vinayak and Suneel Kumar,
   AIP Conference Proceedings **1728**, 020232 (2016).

B. Symposia/Workshops/Conferences:

4. Tracing technique to study the isospin mixing at intermediate energies.
   Amandeep Kaur
   Proc. of National Conference on Emerging Challenges in Nuclear and Many-body Physics, P-26, Page no. 31 (2014).

5. Optimization of initialization parameters in transport models: IQMD and QMD.
   Amandeep Kaur and Suneel Kumar,
   Zakopane Conference on Nuclear Physics, p.191 Sep. (2014).

6. On the stability of final stage fragments obtained through transport models.
   Amandeep Kaur, Rubina Bansal and Suneel Kumar,
   Proceedings of the DAE Symp. on Nucl. Phys. **59**, 458 (2014).

7. Thermalization in non-symmetric heavy ion reactions.
   Karan Singh Vinayak, **Amandeep Kaur** and Suneel Kumar,
   Proceedings of the 9th Chandigarh Science Congress, pp-60, page-257 (2015).

8. Neutron/Proton emission in mass-asymmetric intermediate energy heavy-ion collisions.

   Amandeep Kaur, Karan Singh Vinayak, Deepshikha and Suneel Kumar,

   Proceedings of the DAE Symposium on Nuclear Physics , Vol. 60, 458-459 (2015).

9. Interrelation between Energy of Vanishing flow and Transition Energy.

   Deepshikha, **Amandeep Kaur** and Suneel Kumar,

   Proceedings of the DAE Symposium on Nuclear Physics , Vol. 60 , 460-461 (2015).

10. pt dependence of light mass fragments at intermediate energies.

    Amandeep Kaur and Suneel Kumar,

    Proceedings of the National Conference on Recent Trends in Nuclear Physics, P-2, 19-20 (2016).

11. Isospin effects in transport models (simulation techniques) to study production of fragments and their flow.

    Amandeep Kaur and Suneel Kumar,

    AIP Conference Proceedings 2018 (under review).

Abbreviations

HICs	heavy ion collisions
EOS	equation of state
DDSE	density dependent symmetry energy
NN	nucleon-nucleon
QMD	quantum molecular dynamics
IQMD	isospin dependent quantum molecular dynamics
IBUU	isospin dependent boltzmann uehling uhlenbeck
BUU	boltzmann uehling uhlenbeck
SMF	Stochastic Mean Field
TDHF	Time Dependent Hartree Fock
ETDHF	Extended Time Dependent Hartree Fock
FNs	free nucleons
LMFs	light mass fragments
IMFs	intermediate mass fragments
MST	minimum spanning tree
MSTM	minimum spanning tree with momentum constraints
MDIs	momentum dependent interactions
SMD	soft momentum dependent
GDR	giant dipole resonance
GMR	giant monopole resonance
$< R_E^{global} >$	global nuclear stopping
$< R_E^{local} >$	local nuclear stopping

Contents

List of Figures

List of Tables

ABSTRACT

In the present study we intend to investigate the role of density dependent symmetry energy (DDSE) for mass symmetric and mass asymmetric nuclear reactions. The theoretical investigations are carried out utilizing microscopic quantum molecular dynamics (QMD) and isospin-dependent quantum molecular dynamics (IQMD) models. Author has made a descriptive analysis for fragment production, fragment yield, transverse flow and nuclear stopping (thermalization) subjected to the well established DDSE.

Initially, general introduction of the nuclear physics and blueprint of the present work have been discerned. Various predicted and observed phenomena at intermediate energies will be presented owing to their significant role to study heavy ion collisions (HICs) at intermediate energies. Then overview of mass symmetric and asymmetric HICs is given. The role of DDSE and its various forms on the dynamics of the reaction are discussed. The status of the available experimental and theoretical endeavors carried out by various collaborations for multifragmentation, nuclear stopping and anisotropic flow has also been summarized. Author has used primary models QMD and IQMD for the present investigation and has portrayed these in detail in the present work. Author has first analyzed the impact of initialization parameters (i.e. physics as well as technical) on multifragmentation and flow. The dependence of the observable on mean field potential parameters, Coulomb and symmetry potentials as well as the initialization conditions of the above mentioned two models have been considered.

Subsequently the most appropriate approach has been taken into account to ponder the direct impact of DDSE on multifragmentation in case of mass symmetric and mass asymmetric HICs. The effect of mass asymmetry on the fragment production is very much evident. The influence of DDSE can be surmised from the multiplicity of fragments produced from participant zone. The experimental information for nearly symmetric reaction has been compared with theoretical calculations. Attempts have been made to investigate the influence of DDSE on global and local nuclear stopping for mass symmetric and asymmetric nuclear reactions over a wide range of incident energies and impact parameters. It has been observed that global as well as local nuclear stopping is influenced by the mass asymmetry of the reaction firmly. Impact of DDSE has been noticed in local

nuclear stopping. Also, as the impact parameter increases, the global stopping decreases. Influence of impact parameter on nuclear stopping is more at higher energies.

At last, we present a viewpoint along with the conclusions and importance of the work done in this thesis.

Chapter 1

Introduction

" Arise ! Awake ! and stop not untill the goal is reached. "
.....Swami Vivekananda

1.1 Introduction

The progress of science is based on the work of countless discoveries. In 1896, Henri Becquerel contemplated the radiation transmitted by bright materials. He was captivated by Roentgen's current revelation of X-beams and searched for them in Uranium salts as well. However, something happened which was absolutely unexpected: Becquerel found that these salts emanate another type of radiation unique in relation to both glowing light and X-beams, which he called Uranic beams. This marked the beginning of the field of nuclear physics. The exploration of nuclear physics has prompted applications in various spheres such as nuclear power generation, magnetic resonance imaging (MRI), nuclear medicine, nuclear arms, materials science, and radiocarbon dating in archaeology and geology. Fig. 1.1 illustrates the applications of nuclear physics in today's world. However, some of the big queries in science today are still not addressed, for example, how the universe developed to its present state and where we as a whole originated from. In particular, the issues related to explosive scenarios, such as supernovae and X-ray bursters, exhibit before us the challenge of understanding the nuclear processes that power, such fiery outbursts and all the while synthesize a large number of the elements around us.

The intermediate energy heavy ion collisions (HICs) are signified as an exceptional means to investigate the behavior of nuclear matter by varying its density and thus leading to a gateway towards an inside story of nuclear matter in terms of temperature, pressure,

volume, isospin : the nuclear equation of state (EOS) [1,2]. Fig. 1.2 depicts the dynamics of HICs. The typical range of intermediate energy is 10 MeV/nucleon - 1 GeV/nucleon. The study of HICs in this energy domain is a strong field of research which is flourishing admirably. In many instances, it acts as a link between the branch of particle physics and nuclear physics. Therefore it bears the brunt that numerous subjects which are well known to specialists in one branch may not be commonplace to specialists in another branch. The nucleus forms an enticing laboratory to study two sorts of interacting fermions (neutrons and protons) in which the fundamental force is ineffectively comprehended. Also, it gives a critical proving ground for theoretical models that take the lead to anticipate the characteristics of nuclei. In the nucleus, the individual neutrons and protons can unequivocally direct its characteristics in general. The enormous developments made by the HICs in this field, in the present and the last few decades has achieved great developments, where the questions regarding the nuclear EOS of compressed nuclear matter, transport coefficients, in-medium cross-sections [3], the momentum dependence of the NN interactions [4,5] and their isospin reliance are well studied. The collective flow [6,7] (directed and elliptical) has revolutionized the analysis of the nuclear EOS and its dependence on isospin. The multi-fragmentation [8] and nuclear stopping [9] are well suited to study the nuclear matter interactions at low densities. In the investigation of hot dense matter, HICs at intermediate energies present excellent opportunities compared to other methods. Though, astrophysical phenomenon can provide only an indirect information regarding the neutron stars and supernova explosions [10–12], the intermediate energy reactions provide us an opportunity to understand the conditions which prevailed during the formation of the universe.

Under the high density and temperature conditions, it is possible to estimate the thermodynamic properties of firmly interacting nuclear matter produced in the early universe and learn about its properties. The learning is contingent on proper modelling of the collisions. Therefore, to think about these reactions, one requires not just the utilization of numerous standard techniques of nuclear physics, but also the improvement of new techniques and facilities intended to address the challenges posed by this field.

Fig. 1.3 shows the phase diagram of nuclear matter [13]. The state of a nucleus

Figure 1.1: The applications of nuclear physics in today's world.

relies on density and temperature analogous to the state of an agglomeration of atoms or molecules that rely upon pressure and temperature. The states of nuclei with minimal energy indicate fluid like qualities and acquire a density of 0.17 nucleons/fm^3. In simple customary form this relates to 270 trillion times the liquid water density. On the other hand, when the density and temperature is higher in HICs, quarks and gluons get deconfined. This plasma of quarks and gluons was the condition of the matter, soon after the big-bang before its condensation in hadrons as depicted in Fig. 1.3. Till now, pion condensation [14] and quantum transitions related to nuclear shape [15] have been useful in judging various transitions of a significant diverse character. The HICs at intermediate energies focuses on the theoretical description of liquid-gas phase transition where

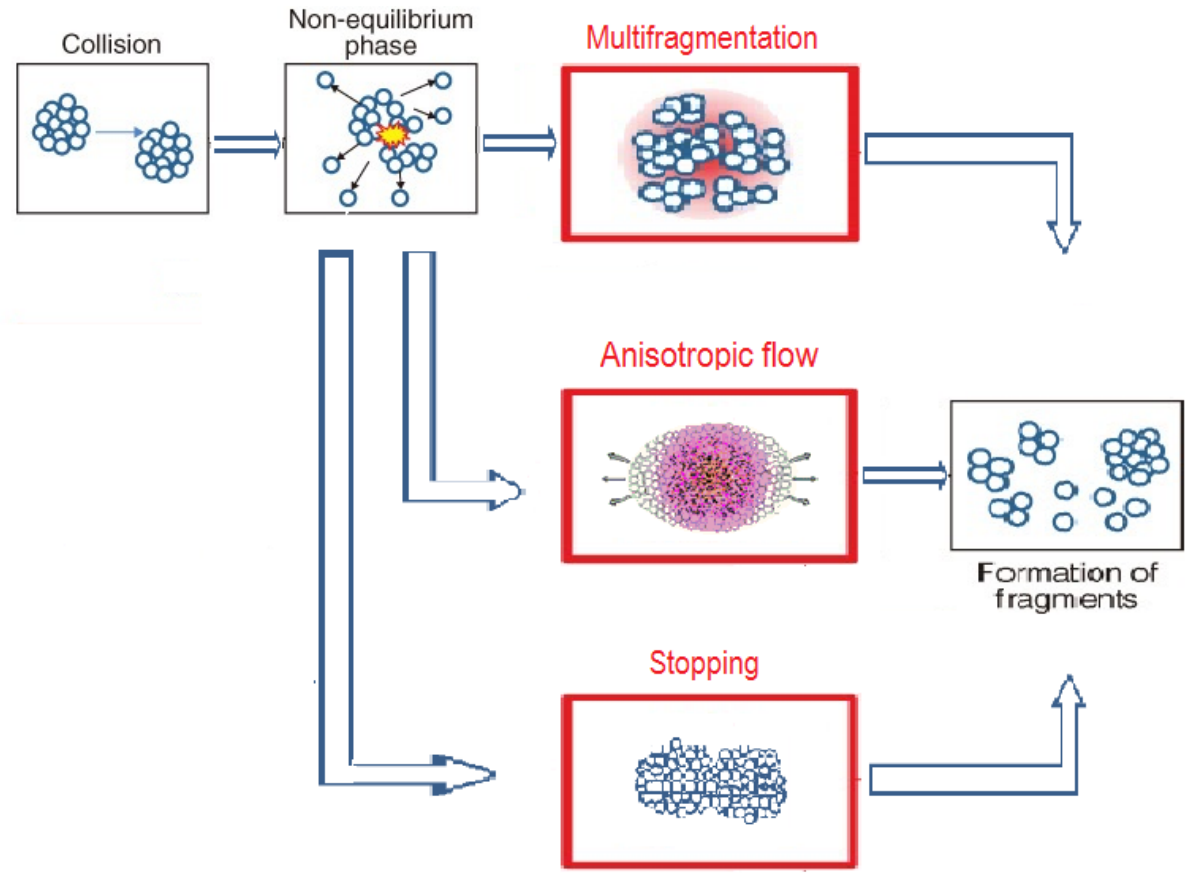

Figure 1.2: The various phenomena of HICs at intermediate energies.

dense nuclear matter (liquid) transitions drastically into dilute system (gaseous) [16]. The existence of phase transition has been indicated by several observables proposed in the literature.

In the laboratory, the main conceivable approach to heat nuclei to critical temperatures is by impacting them with other nuclei. Heating the nuclei to a temperature of a couple of MeV leads to the evaporation of a part of nuclear "liquid". Based on knowledge about the interactions among the nucleons, we realize that, the nuclear liquid additionally is characterized by its physical property called "latent heat of vaporization" much the same as water. Hence, a first-order phase transition ought to be experienced by the nuclei. At a basic point, called the critical point of nuclear matter, this liquid-gas coexistence is additionally anticipated to end. The experiments, especially at National Superconducting Cyclotron Laboratory (Michigan State University,USA), GANIL (France), Texas A and M University (USA), GSI (Germany), LNS (Italy) and other labs are conducted to

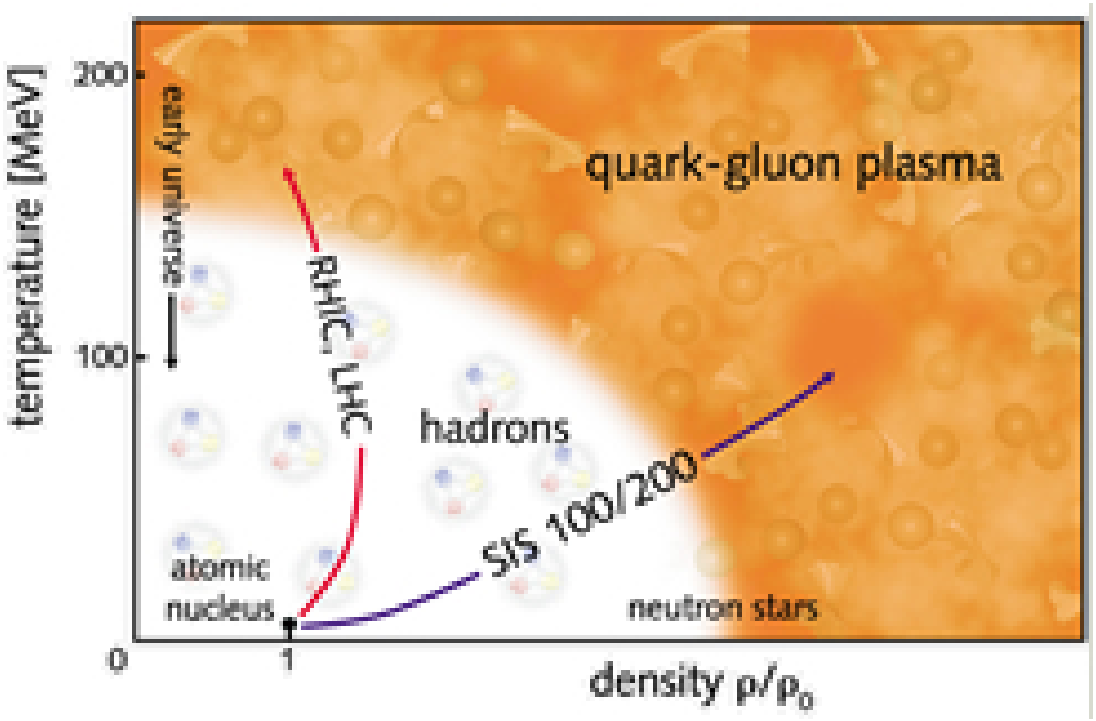

Figure 1.3: The phase diagram of dense matter. The quark-gluon plasma can be seen at high energy or density while the liquid-gas coexistence region can be seen around the nuclear matter saturation point. The figure has been taken from Ref. [13].

explore the existence of the critical point of nuclear matter and at what temperature and density it exists.

There are significant difficulties that nuclear researchers confront in their endeavors to investigate the nuclear EOS and the phase transitions. The time interval available for conducting the experiment is very small, about 10^{-21} seconds. Moreover, the measurement of these state variables (temperature, density and pressure) cannot be done directly. The signatures of a phase transition are difficult to figure out when there are just couple of basic constituents present (the number of nucleons is only few hundred). Despite these challenges, there has been a significant progress in this field. It has now become easy to measure the thermodynamic state variables and determine the critical point of nuclear liquid gas phase diagram. Recent investigations on nuclear fragmentation are prompting enhanced insight into this vital question. The heavy ion researchers considered that there is a possibility of more than one phase transition as depicted in Fig 1.3. Apart from phase transition from the nuclear liquid to a gas of nucleons, nucleons themselves

can experience a phase transition at significantly higher temperatures and densities. This state is called "quark-gluon plasma," similar to an atomic plasma in which electrons turn out to be noticeably free from atoms. The daunting task of setting up the environment for actualizing this phase transition and watching its signatures has been effectively carried out at BNL (Brookhaven National Laboratory), New York and at CERN (Conseil Europeen pour la Recherche Nucleaire), Switzerland. The Relativistic Heavy Ion Collider (RHIC) constructed at BNL, considers the study of this intriguing and one of a kind phase transition in the nuclear EOS as its primary goal.

Although it is difficult to understand the mechanics and thermodynamics of astrophysical phenomena like formation of the heavier elements after fusion reactions and neutron captures in the interiors of stellar bodies, but one should not be discouraged by the fact that we do not know all the answers. The nuclear EOS and compositions of neutron stars is in many ways related to DDSE [17]. The measurement of the masses or radii of these stars both experimentally and theoretically can strongly constrain the neutron star matter EOS. It needs to be mentioned here that neutron star with a maximum mass of 2.01 ± 0.04 solar mass has been observed to date and such measurements set an upper limit of $(3.74 \pm 0.15)\times10^{15}$ g/cm^3 on the maximum nuclear density [18, 19]. The present study focuses on the investigation of the role of DDSE around the high density zone achieved in both mass symmetric as well as mass asymmetric nuclear collisions. The symmetry energy will help us to gain an indirect information about the density and pressure reached in HICs. The high density achieved during the compression of nuclei in mass asymmetric system can be correlated with the density achieved during galaxy condensation. The chemical diversity of a galaxy is the result of expulsion of newly synthesized nuclei (either through products of nuclear fusion or species formed during explosion itself) by a supernovae. The neutron star which is formed at the center of a core-collapse supernova act as a gold mine if one has to study EOS of dense nucleonic matter. Moreover the radioactive ion beam facilities will also play its role in elucidating the distinct composition and modelling of nuclear forces more accurately in neutron stars.

1.2 Equation of state of nuclear matter

An equation of state (EOS) is a thermodynamic equation relating state variables which depict the phase of matter under a given layout of physical conditions. The most noticeable importance of EOS is to connect density of gases and liquids to temperatures and pressures. The nuclear matter EOS represents the connection between the thermodynamic variables, for example, pressure, density and temperature.

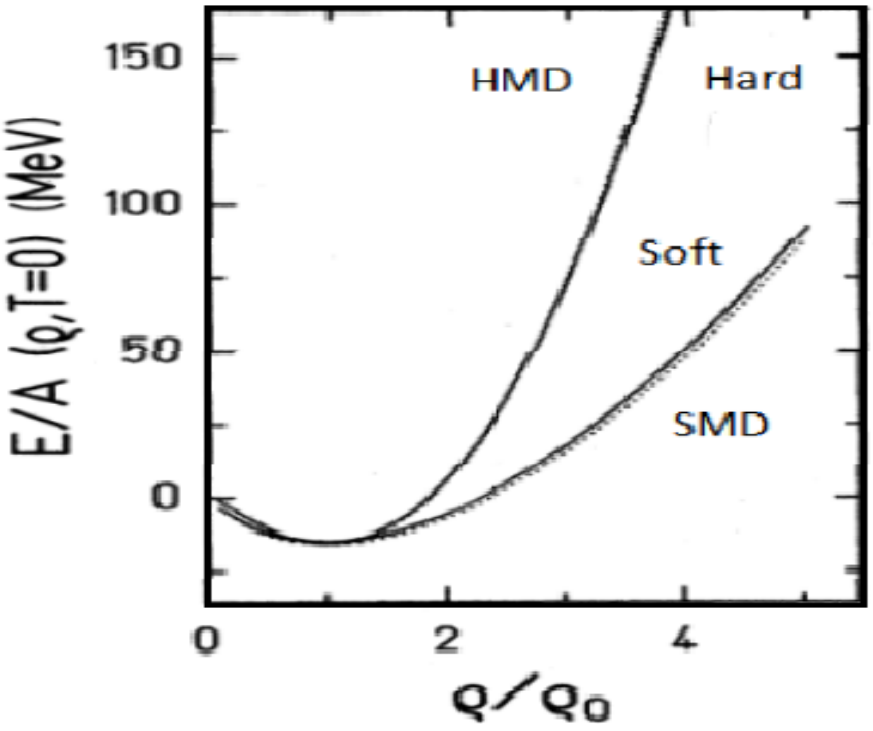

Figure 1.4: The possibility of four equation of states along with momentum dependent interactions in the compressibility diagram [23].

The elementary information about the nuclear EOS comes from the Bethe- Weizsacker binding energy formula [20, 21] that has contributions from the volume and surface terms as well as Coulomb potential and asymmetry of a nucleus. The binding energy is

$$E_B(A,Z) \;=\; a_v A - a_s A^{2/3} - a_c Z(Z-1)A^{-1/3} - a_a \frac{(A-2Z)^2}{A} + \delta a_p A^{-3/4} \qquad (1.1)$$

Here Z and A is the charge and mass of a nucleus. The details of these terms are available in [22].

The equation 1.1 gets modified for infinite nuclear matter where both the volume and the number of nucleons are considered to be infinite but their ratio remain fixed for the density at saturation stage. The binding energy per nucleon can be expressed as

$$\epsilon(\delta) = -\frac{E_B(A,Z)}{A} = -a_v + a_a\delta^2 \tag{1.2}$$

where $\delta = (N-Z)/A$ is the neutron-proton asymmetry. Here in equation 1.2, the Coulomb term, nuclear surface term and pairing term have been neglected. This expression now signifies that the binding energy per nucleon of the incompressible liquid drop (nucleus) of density $\rho_o = 0.16fm^{-3}$ is $a_v \approx 16$ MeV and an energy cost of $a_a \approx 32$ MeV in converting all protons to neutrons. However the information about the dependence of energy per nucleon on density and neutron-proton asymmetry is given by the nuclear EOS. The equation 1.2 further helps us in describing the nuclear EOS of an asymmetric nuclear matter which will be discussed in section 1.4.

The nuclear symmetry energy around ρ_0 is given by the expansion:

$$E_{sym}(\rho) = E_{sym}(\rho_0) + L\chi + \frac{K_{sym}}{2}\chi^2 + O(\chi^3) \tag{1.3}$$

where $\chi = \frac{\rho-\rho_0}{3\rho_0}$. Here, K_{sym} is the curvature and L is the slope parameter, which are given by:

$$K_{sym} = 9\rho_0^2\frac{d^2E_{sym}(\rho)}{\partial\rho^2}|_{\rho=\rho_0}, \qquad L = 3\rho_0\frac{dE_{sym}(\rho)}{\partial\rho}|_{\rho=\rho_0} \tag{1.4}$$

Both the parameters give information about DDSE around normal nuclear matter density, ρ_0. Therefore it carries vital information about the properties of DDSE at low as well as at high densities.

In order to characterize the nuclear EOS, the nuclear incompressibility is introduced which represents the stiffness of the nuclear matter against the changes in density and is defined as

$$K = 9\left[\frac{d}{d\rho}\left(\rho^2\frac{\partial(E/A)}{\partial\rho}\right)\right]_{\rho=\rho_0}, \tag{1.5}$$

Here, E/A is the energy per nucleon at normal nuclear matter density ρ_o. The two commonly used EOS (soft and hard with K= 200 MeV and 380 MeV respectively, along with MDIs) corresponding to two different incompressibilities [23,24] are depicted in Fig. 1.4.

For asymmetric nuclear matter, one can extract the value of incompressibility coefficient K_{asym} from the experimentally measured energies of isoscalar monopole vibrations

(GMRs) in nuclei [25]. Most recently, the value of K_{asym} has been obtained from measurements of isotopic dependence of the GMR in Sn isotopes having even mass in Ref. [26, 27] and is given by $K_{asym} = -550 \pm 100$ MeV. The values of K_{asym} proposed by some other groups are -320 ± 180 MeV [28] and $-566 \pm 1350 \sim 34 \pm 159$ MeV [29].

When the MDIs are introduced, one needs to alter the parameters of Skyrme interactions so that correct saturation properties of normal nuclear matter together with indistinguishable incompressibilities corresponding to soft and hard EOS could be obtained. The inclusion of momentum dependence in the new parameter sets gives rise to the incompressibilities called SMD and HMD, respectively.

When the nuclei first touch each other, they are cold. Because of NN collisions they form a dense and strongly interacting matter as a result, both entropy and temperature will increase. During the dismantling period, the temperature tumbles to a lower value because of the confused movement of nucleons and amid this development the route followed by this temperature slump is different. This infers that at a specific value of density, there are two distinct estimations of temperature, which implies that after the impact, the participant matter holds a colossal estimation of energy regardless of the possibility that we attempt to cool it to its original state as shown in Fig. 1.5.

Amid the expansion the density will tumble to a value where the constituents are not anymore interacting, this density is known as the freeze-out density [24]. When the magnitude of the densities in the nuclei is higher than those seen in ordinary nuclei, many of the neutron stars properties completely rely on the EOS. The EOS decides properties, for example, the mass range, the relationship between mass and radius , the outside layer thickness and the cooling rate [30, 31]. Investigations of many sources, for example, the monopole resonance in the finite nuclear matter, giant dipole resonance (GDR), nuclear collisions at high energy, supernovae, and neutron stars can be useful in obtaining information on the EOS.

The nuclear matter compressibility has received significant attention in the last few decades and a variety of methods have been employed to determine this fundamental property of matter. Various relativistic and non relativistic calculations were used to calculate the nuclear matter incompressibility. One of the approaches involves the calculations of

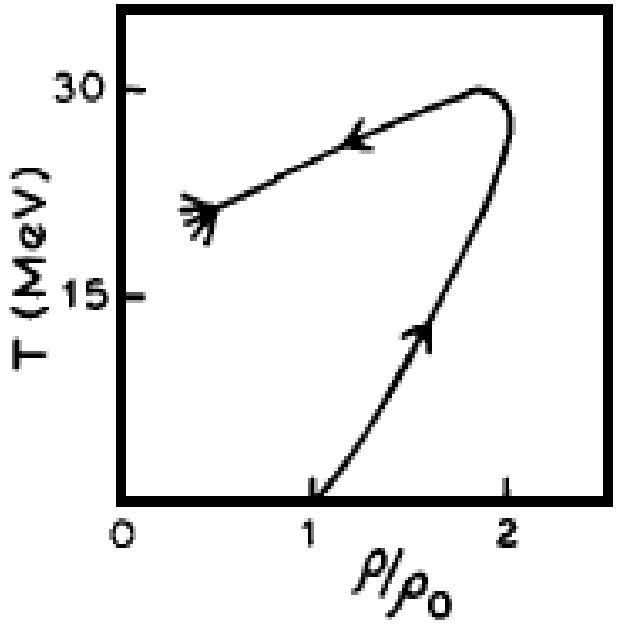

Figure 1.5: A conjecture for the evolution of temperature and density of nuclear matter in the course of a heavy-ion reaction [24] .

breathing mode giant monopole resonance (GMR). Several parameterizations of effective Lagrangians have been proposed, each one of them discerning portrayal of nuclear ground states and compressibility values in a relativistic mean field namely Dirac-Hartree structure. The NL-SH model of Sharma *et al.*, [32], TM1 of Sugahara and Toki [33], and NL1 of Rheinhard *et al.*, [34] are some of the models using this framework. The Gogny interactions adopted by Blaizot *et al.*, [35] and the Skyrme interactions adopted by Hamamoto *et al.*, [36] were useful in calculating compressibilities. Another effort in this direction was made by Falk *et al.*, [37] using Puff-Martin model and gave useful insights into nuclear compressibility and DDSE.

1.3 Mass symmetric and mass asymmetric nuclear reactions

The HICs can be categorized into mass symmetric and mass asymmetric collisions based on the number of nucleons present in the colliding partners. The reactions where the total

number of nucleons in the projectile nuclei and target nuclei is equal, are termed as mass symmetric nuclear collisions. In mass asymmetric collisions, the number of nucleons in the target and projectile are unequal.

The reaction dynamics of either type is influenced by various physical quantities, for example, the incident energy, impact parameter, NN cross section and the EOS.

It may perhaps be observed that when the conditions of input ingredients are similar both types of reactions respond in a very unique way. The mass asymmetry of a reaction is characterized by the constant $\tau \left(= \frac{A_T - A_P}{A_T + A_P}\right)$; where A_P and A_T are masses of the projectile and target separately. The $\tau = 0$ corresponds to mass symmetric collisions while $\tau \neq 0$ corresponds to mass asymmetric collisions. When the input ingredients are similar, the symmetric collisions respond differently as compared to mass asymmetric one. In mass symmetric reactions, the incident energy induces more compression while mass asymmetric reactions have insufficient compression in light of the fact that a considerable amount of excitation energy is in the form of thermal energy [38, 39]. It is worth specifying that a large number of endeavors for studying multifragmentation were restricted to symmetric colliding nuclei only [40, 41] however, only a few were reached out to the collisions of mass asymmetric target and projectile combinations [42, 43]. The asymmetry of a reaction studied experimentally can be as large as 0.89 (in the case of C + Au [44]). FOPI collaborations have also carried out a study on the mass asymmetric reactions of Ca + Au/Au + Ca [45, 46]. In the literature, a lot of isolated studies are available on the mass asymmetric reactions [45–47].

In mass asymmetric reactions, a considerable amount of energy is deposited as thermal energy. The primary NN collisions leads to the formation of a fireball and a couple of these nucleons navigate through the bigger nucleus. As these nucleons experience secondary collisions they energize the bigger nucleus. Fig 1.6 depicts the dynamics of mass symmetric and asymmetric reaction. After the overlapping stage, repulsion is generated among the nucleons of the projectile and the target. When these nucleons (projectile) move through the target, they encounter a forceful transverse thrust along with rotation of the nuclear matter. When the incident energies are high, collisions at central geometry prompts the total blowout of the system, while collisions at peripheral geometry are considered as fragmentation mechanisms. In case of collisions at peripheral geometry in general, the

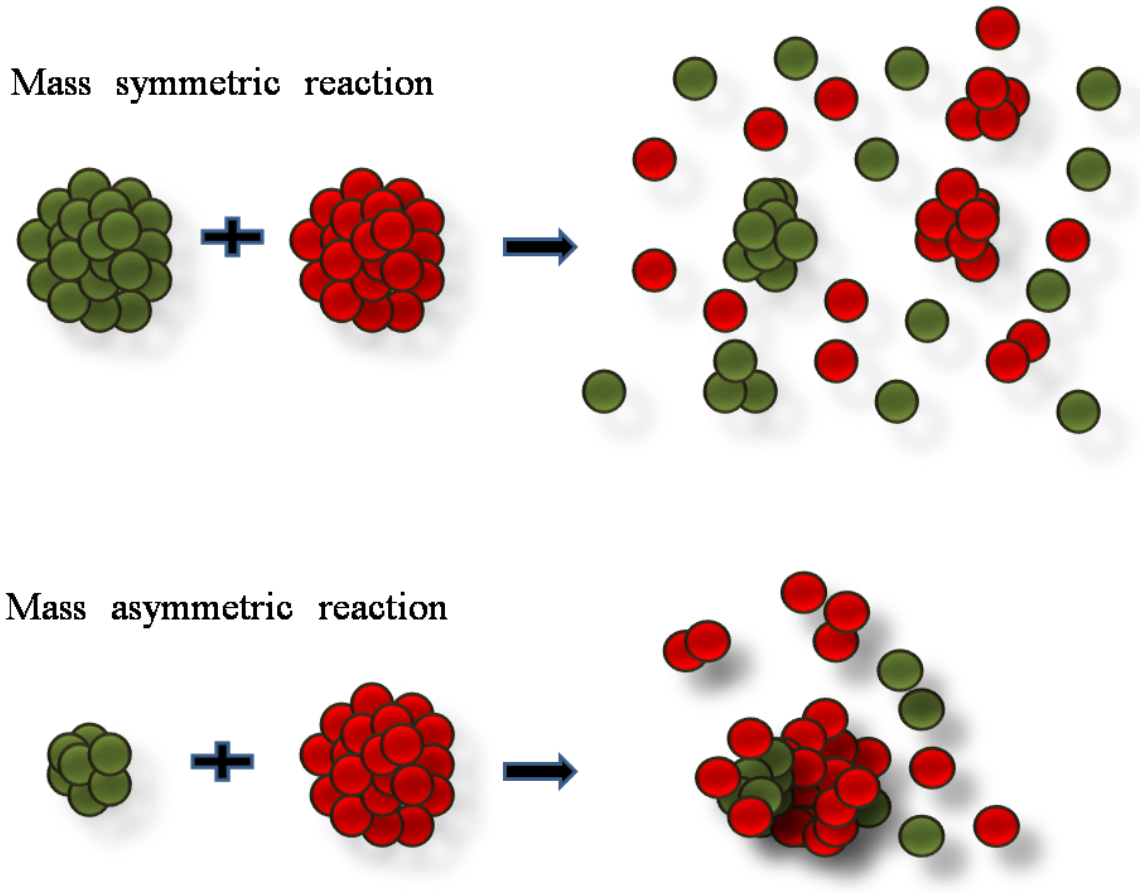

Figure 1.6: The dynamics of mass symmetric and mass asymmetric reaction .

projectile and target scarcely brush each other and furthermore, if a mass asymmetric collision is looked upon, the lighter nuclei have a tendency to pivot around the heavier system. Fig. 1.7 illustrates the dynamics of mass asymmetric collisions at a fixed impact parameter (peripheral in this case). At central collisions, the projectile and target nucleons get enough space to communicate with each other and thermalization occurs.

As the impact parameter is increased, the degree of thermalization lessens in comparison to the previous case. As the impact parameter is further increased, the projectile has a tendency to whirl around the target. For a fixed impact parameter (peripheral collision here) the rotational effect of the projectile and target nucleons can be clearly seen in Fig 1.7. Higher the mass asymmetry, more will be the rotational effect. At a point when the nuclear matter is exposed to high compression, higher density developed in the midst of the reaction will be distinctive for different colliding nuclei. The density achieved in the central area of target and projectile for $\tau = 0.3$ is marginally more than that of the case

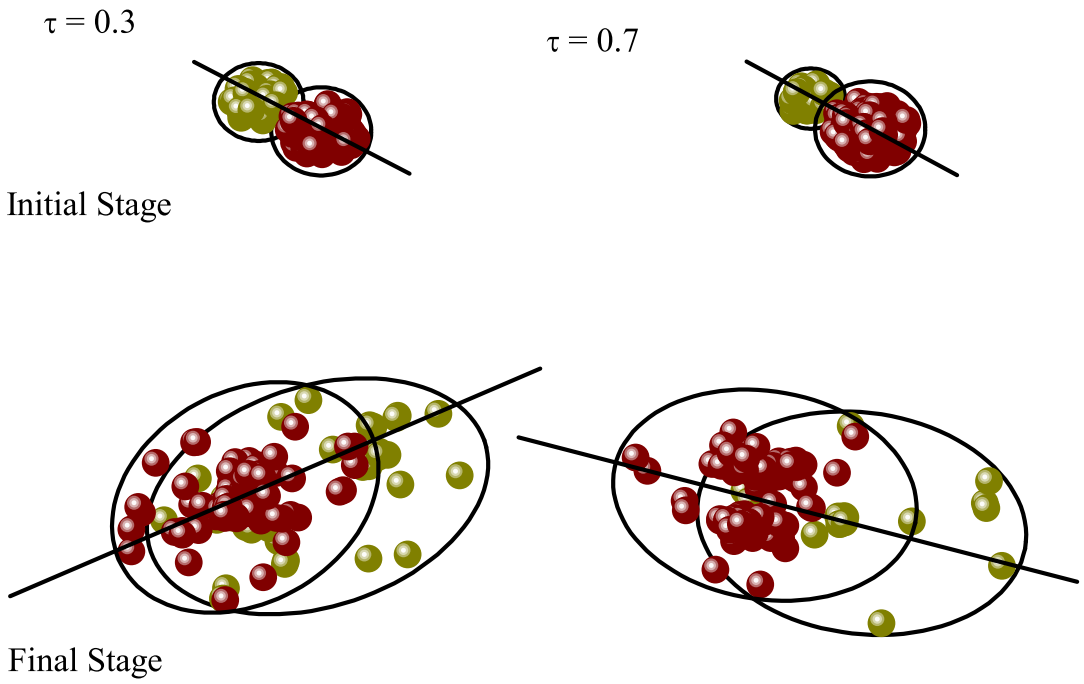

Figure 1.7: The effect of mass asymmetry on the dynamics of the reaction at fixed impact parameter.

for $\tau = 0.7$.

Fig. 1.8, shows the dynamics of mass asymmetric reaction ($\tau = 0.7$) at three different energies (50 MeV/nucleon, 150 MeV/nucleon and 600 MeV/nucleon) and at a fixed impact parameter (scaled) of $\hat{b} = 0.6$. Due to mass asymmetry, the spatial and momentum distribution of nucleons becomes non uniform. This is because the number of nucleons in projectile and target are different in comparison to symmetric nuclear reactions. Hence, the contribution of the spectator and participant matter will likewise be different for all the reactions. For a given mass asymmetry, as the incident energy increases the distribution of projectile and target nucleons becomes more and more non spherical due to the unequal transfer of energy among nucleons. At low energy i.e. 50 MeV/nucleon, the distribution is less non-spherical whereas at 600 MeV/nucleon the distribution is highly non-spherical. During the initial stage of the reaction, the two nuclei are boosted towards

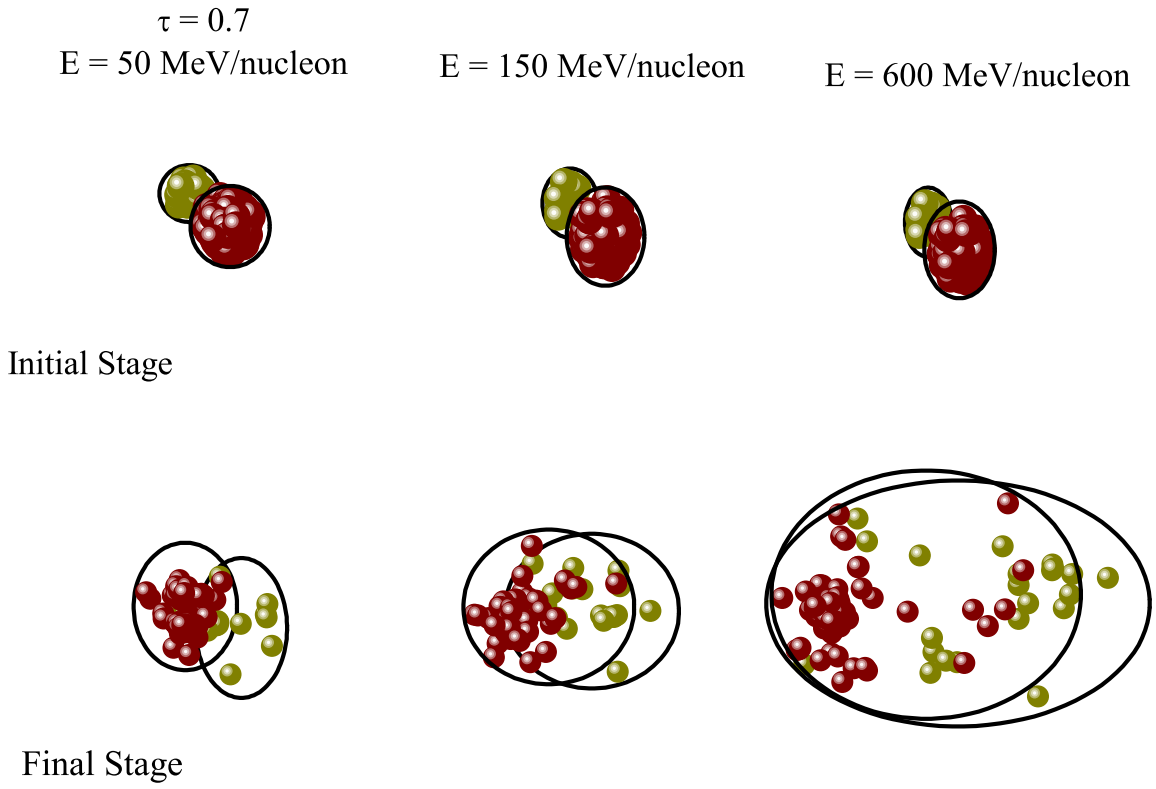

Figure 1.8: The incident energy dependence of the dynamics of mass asymmetric reaction

.

each other and appear to be Lorentz contracted. More the incident energy, more is the contraction as visible in the figure. When nuclei of a mass-asymmetric collision system have a tendency to slam into each other, density starts to build up in the overlapping domain of projectile and target and the uninteracted parts of the nuclei remain as such. The dissipation of compressional and surface energy outwards from the overlapping zone (participant zone) leads to the excitation of the uninteracted remnants (spectators). The participant nucleons of the projectile transfer its momentum to the combined system (participant zone) which moves forward with a velocity lesser than incident energy of projectile. This participant zone then equilibrates and expands isotropically in its center of mass region [48]. As evident from the figure, more the incident energy pumped into the system, higher will be the value of maximum density achieved, resulting in large number

of collisions among the nucleons.

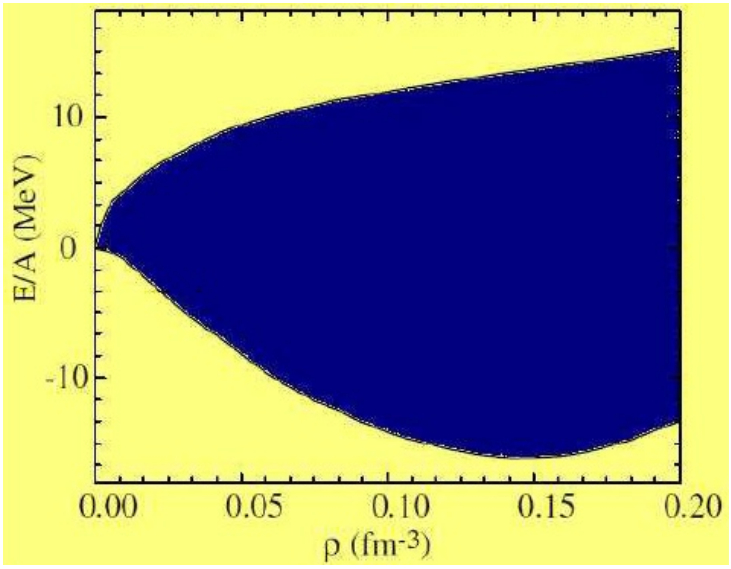

Figure 1.9: The figure depicts the concept of symmetry energy. The energy density for pure neutron matter is illustrated by top line and symmetric nuclear matter is illustrated by lower line. The difference of two lines is the symmetry energy [51].

1.4 Symmetry energy and its various forms

The nuclear EOS involves learning of the diversified properties of nuclear matter: saturation density, incompressibility K(ρ), energy per nucleon $E(\rho)$ (ρ is density), the symmetry energy and its density content, namely, the symmetry coefficient $E_{symm}(\rho)$ and all the higher symmetry derivatives. The nuclear symmetry energy which directs significant features of nuclei and neutron stars is described as the difference between the binding energy of symmetric nuclear matter (equal proton and neutron numbers) and that of pure-neutron matter [49, 50]. It is taken as 32 MeV corresponding to density of normal nuclear matter, $\rho_0 = 0.17 fm^{-3}$.

In other words, it illustrates the propensity of nuclei to have greater binding energies (E/A) for symmetric systems.

Various theoretical approaches, for example, the Brueckner-Hartree-Fock (BHF) and the Dirac-Brueckner-Hartree-Fock (DBHF), Skyrme Hartree-Fock (SHF) and the rela-

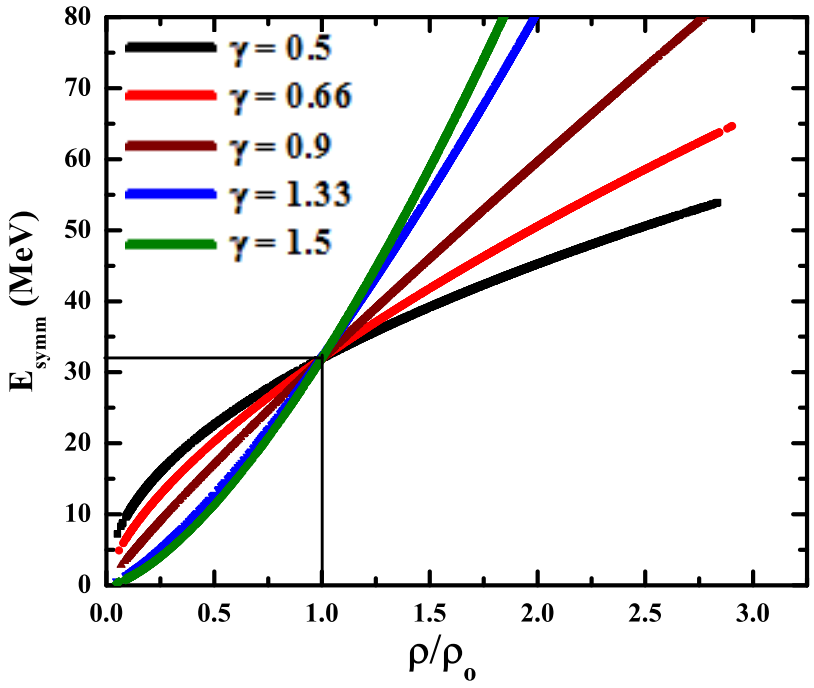

Figure 1.10: A pictorial representation of symmetry energy for different values of $\gamma = 0.5$, 0.66, 0.9, 1.33 and 1.5.

tivistic mean field (RMF) calculations can be used to resolve the symmetry energy [49,51]. Specifically, various cutting edge experiments will be committed to the investigation of the DDSE in the near future.

The Fig. 1.9 depicts an elementary outline of the idea of symmetry energy. The energy density for pure neutron matter is depicted by top line and symmetric nuclear matter is depicted by lower line. The difference of two lines is the symmetry energy, which express the impact of isospin on energy density of nuclear matter .

Initially, Brueckner and Gammel estimated the symmetry energy for small neutron excess which was later more correctly demonstrated by Brueckner and Dabrowski [52].

The fourth term $\frac{a_A(N-Z)^2}{A}$, in equation 1.1 signifies the symmetry energy.

The energy per particle of an asymmetric nuclear matter with density ρ and an isospin asymmetry $\delta_A = (\rho_n - \rho_p)/\rho$, can be determined by a parabolic law [49], i.e.,

$$E_{sym}(\rho, \delta_A) = E_{sym}(\rho, 0) + E_{sym}(\rho)\delta_A^2, \tag{1.6}$$

where $E_{sym}(\rho,0)$ denotes energy per particle of symmetric nuclear matter and $E_{sym}(\rho)$

represents the symmetry energy [49]. $\rho = (\rho_n + \rho_p)$ is the total density (where ρ_n and ρ_p are the neutron and proton densities respectively). $\delta_A = (\rho_n - \rho_p)/\rho = 0$ represents symmetric nuclear matter where $\rho_n = \rho_p$. Neutron-rich and proton-rich matter will be characterized,respectively, by $\delta > 0$ and $\delta < 0$.

The equation given below provides us the parameterization for the DDSE:

$$E_{sym}(\rho) = E_{sym}(\rho_0)\left(\frac{\rho}{\rho_0}\right)^{\gamma} \tag{1.7}$$

The value of γ determines the stiffness (or strength) of the symmetry energy at densities above and below the saturation density. The variation of symmetry energy with respect to γ is illustrated in Fig. 1.10.

1.4.1 Symmetry energy for mass symmetric and asymmetric reactions

The symmetry energy of nuclear matter is a basic property essential for diving into the structure of systems as assorted as the nucleus and the neutron star. Experimentally, the symmetry energy is not a straightforwardly quantifiable parameter and has to be derived in a refined way from observable that identify with the symmetry energy. Therefore, exploratory assurance of the symmetry energy is subject to how precisely a theoretical model reproduces experimental data. So far many experimental investigations of the symmetry energy have been performed. Li and Han [53] performed in all 28 analyses consisting of terrestrial laboratory experiments and astrophysical observations and presented nuclear symmetry energy and its slope at normal density of nuclear matter. The constraints on nuclear symmetry energy and its density slope indicate that the nuclear isovector potential and neutron proton effective k-mass splitting are near to their global averages of 29 MeV and 0.27δ respectively where δ is the neutron-proton asymmetry. However efforts are needed for further reducing the uncertainties using theoretical techniques in extracting the values from the experimental data. Some of the observable that can be utilized to extricate the symmetry energy are the fragment turnout(intermediate mass fragments and cluster production), pre-equilibrium emission, isoscaling constant, twofold neutron to proton ratio, isospin diffusion and isospin transport rate and neutron skin information [54]. Kowalski *et al.*, [55], inspected symmetry energy at very low densities (0.01 - 0.05) ρ_o by taking Zn + Mo, Au reactions at incident energy of 35 MeV/nucleon. It was concluded

that in order to analyze symmetry energy at such low densities, isoscaling examination of the light clusters ($A < 4$) can be utilized. At very low densities cluster formation becomes crucial and mean field estimations do not consider such effects. When the densities are higher than 0.2 - 0.3 ρ_o, the many body interrelation vanishes and the symmetry energy follows, the dependence anticipated by the mean field calculations. Furthermore, the theoretically decided DDSE is to a great extent unconstrained and its determination is still a challenge at densities higher than the normal nuclear matter density ($\frac{\rho}{\rho_0} > 1$). Its experimental determination at such densities have not been many and most of them are from dynamical model juxtaposition. However experimentally, the elliptic flow ratio of neutrons and protons and difference are considered to be sensitive probes of the high density behaviour of the symmetry energy. The results obtained from the existing FOPI data favor a moderately soft symmetry term corresponding to $\gamma = 0.9 \pm 0.4$ [56, 57]. It is additionally important to consolidate the part of isospin precisely for considerably more practical conjectures in transport model computations. The DDSE has a different role in mass symmetric and mass asymmetric nuclear collisions. The mass asymmetry in the colliding partners will alter the degree of thermalization accomplished amid the nuclear reaction. The mass-asymmetry affects the average density and temperature whereas the maximum temperature and density remain unaffected. The contribution of DDSE brings about an expansion of the average density for bigger estimations of stiffness factor γ. The trend is exceptionally complex in the high-density region, which turns out to be more disputable in the mass asymmetric reactions.

1.5 Observables to understand heavy ion collisions (HICs) at intermediate energies

1.5.1 Multifragmentation

Nuclear fragmentation was discovered almost many decades ago [58, 59] in the cosmic-ray studies as a mystifying phenomenon wherein relativistic protons collided with a target and contributed in the emission of slow nuclear fragments. Their masses were heavier than those of alpha particles, but lighter than those of fission fragments termed as intermediate mass fragments ($3 \leq Z \leq 30$). Later on (in the 1950s), this phenomenon was observed in the experiments at the accelerators by Perfilov, Lozhkin *et al.*, [60]. It is however only

with the advent of powerful 4π detectors [9] that real advances were made. The situation changed dramatically after 1982, when Jakobsson *et al.*, detected a diversified emission of the IMFs in emulsion illuminated by the carbon beam of 250 MeV/nucleon at the Bevalac (Berkeley) [38].

The NN interaction consists of two components as per their radial interdistance: a long-range attractive part and a very short-range repulsive part which includes the compressibility of medium. At excitation energies which are of the order of the binding energy of nuclei a bountiful emanation of nucleons and fragments is experimentally examined which is termed as multifragmentation [16]. When nuclei are excited, there is a slight deviation from their ground-state properties, but no change in the structural properties. At excitation energies of the order of 2-3 MeV/nucleon, the nuclei steadily expand by staying in a condition of thermodynamic balance. Amid this development, the nuclei enter into the locale of subsaturation densities, where are unstable towards density fluctuations, and separate the fragments also called droplet formation [61]. Therefore, a liquid-gas sort of phase transition is built up. This subject however is of significant open deliberation to what degree the fragmenting systems is truly equilibrated or still has a 'memory' of the prior stage [62]. Fig. 1.11 depicts the phenomenon of multifragmentation for both mass symmetric and mass asymmetric colliding partners. The density profiles for the reactions, ${}^{80}_{36}Kr + {}^{80}_{36}Kr$ ($\tau = 0$) (left column) and ${}^{24}_{13}Al + {}^{136}_{57}La$ ($\tau = 0.7$) (right column) at four different time scales (t =0.1 fm/c, t =10 fm/c, t=40 fm/c and t =200 fm/c) have been plotted. The first column corresponds to mass asymmetry ($\tau = 0$) and second column corresponds to ($\tau = 0.7$). At the initial stage (t =0.1 fm/c), the nuclei of a colliding system approach each other. At (t =10 fm/c), the participant zone starts to build up such that the density of the compressed matter becomes higher than the normal nuclear matter density. As evident from the figure, the relative values of density for mass symmetric reaction ${}^{80}Kr + {}^{80}Kr$ ($\tau = 0$) are in such a way that the density of the participant zone is nearly twice the value at the initial stage. Similar is the case with mass asymmetric reaction ${}^{24}Al + {}^{136}La$ ($\tau = 0.7$) for the present energy of 400 MeV/nucleon and scaled impact parameter, $\hat{b} = 0.0$. During the interaction period (t =40 fm/c) the overlapped compressed zone gets heated and starts expanding but remains connected with the spectators. At the freeze-out time, at about 200 fm/c, fragment formation takes

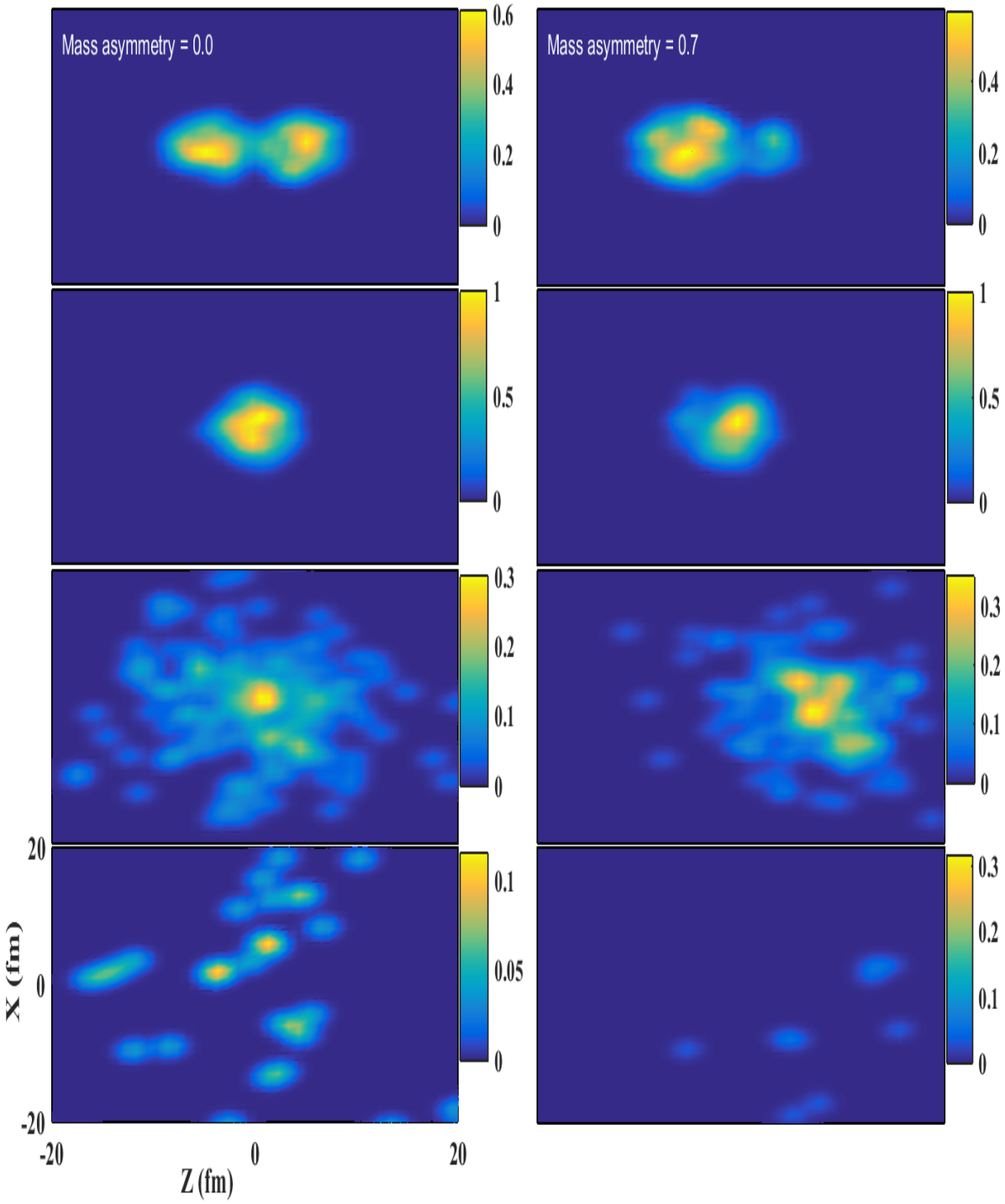

Figure 1.11: The multifragmentation process in mass symmetric and mass asymmetric reactions.

place in the mid-rapidity zone. The fragment formation takes place after expansion but few of them remain attached to the spectators for a longer time [63] till the freeze out stage is reached. The specific time scales chosen here help us understand the dynamics of

mass symmetric and mass asymmetric nuclear reaction more clearly. One can study the evolution of density by taking other time steps in a reaction also.

When the explosion of core-collapsing supernova and neutron star crust takes place dilute inhomogeneous baryonic matter is produced. The efforts done to understand the thermodynamic properties related to multifragmentation helps us to interpret the properties of this baryonic matter. This will be discussed in detail in Chapter 4.

1.5.2 Nuclear Stopping

Nuclear stopping is a basic observable of thermalization that rely vitally on reaction dynamics. The global nuclear stopping can be characterized as the randomization of one-body momentum space or deprivation of the memory of approaching nucleon with a certain momentum. Sometimes, this randomization is additionally identified with the thermalization of the nuclear matter in HICs. Nuclear stopping administers the measure of dispersed energy, the amplitude of large collaborative motion, and information about mechanisms like deep inelastic reactions, neck emission, and fusion reactions [9].

The pressure created because of the reaction tends to build the density and temperature of colliding nuclei which goes about as a genuine investigative logical platform for the nuclear matter EOS. It is critical to research whether an equilibrium is reached or not in a colliding system keeping in mind the end goal to acquire the information on EOS and the reaction mechanism accurately. One of the ways to deal with data on the stopping is by analyzing the rapidity density distributions of the ejected nucleons in the beam direction as well as transverse direction. When two nuclei are bombarded towards each other then three potential outcomes may be proposed:
(i) they either repel each other (full stopping).
(ii) there will be compression or blending of the two (stopping and mixing).
(iii) they will not interact or will pass by each other in that capacity without interaction (transparency).
Greater the density and temperature of nuclear matter, more is the nuclear stopping [64–66]. One can also say that full stopping prompts approximately complete thermalization (or equilibrium) in a collision. Likewise, the dynamics and energy deposition in

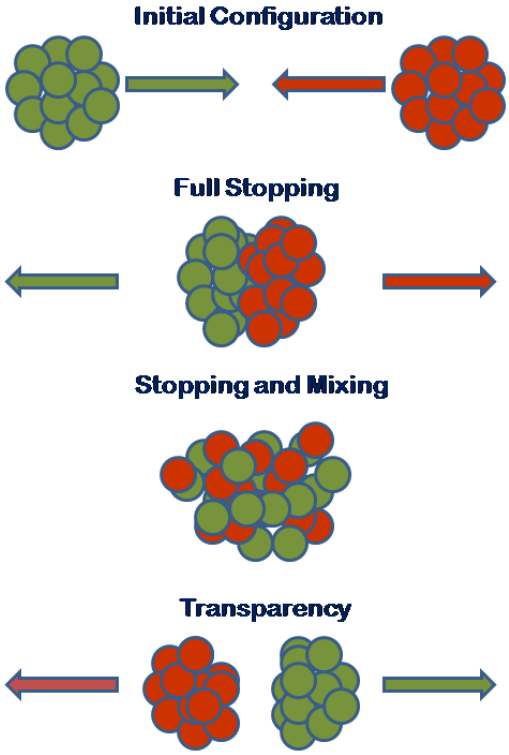

Figure 1.12: The representation of nuclear stopping at intermediate energies.

mass asymmetric reactions is quite different from mass symmetric reactions. Fig. 1.12 represents the phenomenon of nuclear stopping at intermediate energies. The asymmetry of colliding accomplices will fluctuate the degree of thermalization reached during the reaction. Unfortunately, the excited nuclear matter prevails for a brief interim. This in turn becomes difficult to extricate data about the nuclear forces and reaction dynamics in experiments. The detailed study about nuclear stopping will be discussed in Chapter 5.

1.5.3 Nuclear flow

Collective nuclear flow or the in-plane transverse momentum distribution of ejected nucleons, which can furnish details about the nuclear EOS, the symmetry energy and the HICs mechanism, has been contemplated systematically for over three decades. It has been considered efficiently as an element of beam energy, system mass, and impact parameter. Transverse flow delineates the rapidity dependence of the average in-plane transverse momenta of detected by-products of a collision. At lower beam energies (few MeV/nucleon),

the interactions between nucleons are ruled by the attractive part of the nuclear mean field due to which they are redirected to negative angles [67]. At higher beam energies (several hundred MeV-1 GeV/nucleon), the NN scattering and the repulsive part of the mean field dominate due to which the particles are radiated to positive angles [68–70]. At a specific intermediate bombarding energy, namely balance energy (E_{bal}), both the attractive and repulsive component of the interactions are expected to harmonize one another and the slope of flow crosses zeroes, changing its value from negative at low energies to positive at high energies [71]. The Coulomb interaction in HICs is relied upon to assume an overwhelming part in balance energy because of its repulsive nature. The balance energy is observed to be profoundly sensitive towards the nuclear EOS, the NN cross section [72, 73], system size [74], asymmetry of the reaction [75], the beam energy [76, 77], and the impact parameter [78, 79].

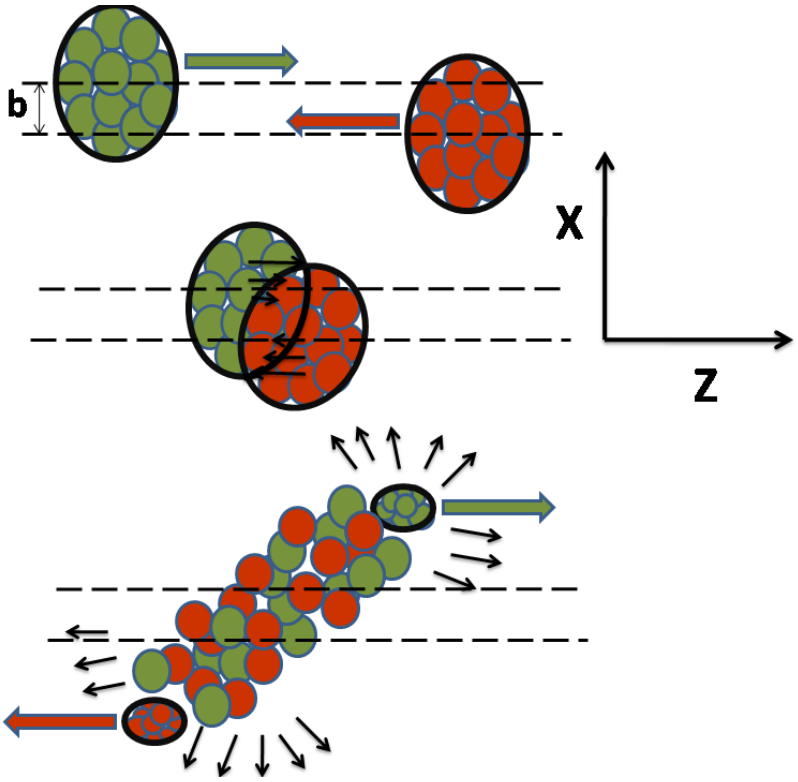

Figure 1.13: The representation of directed flow (v_1) for mass symmetric reactions at intermediate energies.

Fig. 1.13 and Fig. 1.14 depict the phenomenon of directed flow for mass symmetric and mass asymmetric collisions individually. In any case, the influence of mass asymmetry on transverse flow is distinctive. Rather than symmetric collisions, where the location of

the center of mass of combined system is known, this quantity is not known a priori in asymmetric nuclei experimentally. With the increment in mass asymmetry, the maximum density and compression achieved in the participant zone diminish, which reduces the NN collisions. Likewise, E_{bal} is found to increment with the increment in mass asymmetry and has been further specified in terms of mass power law.

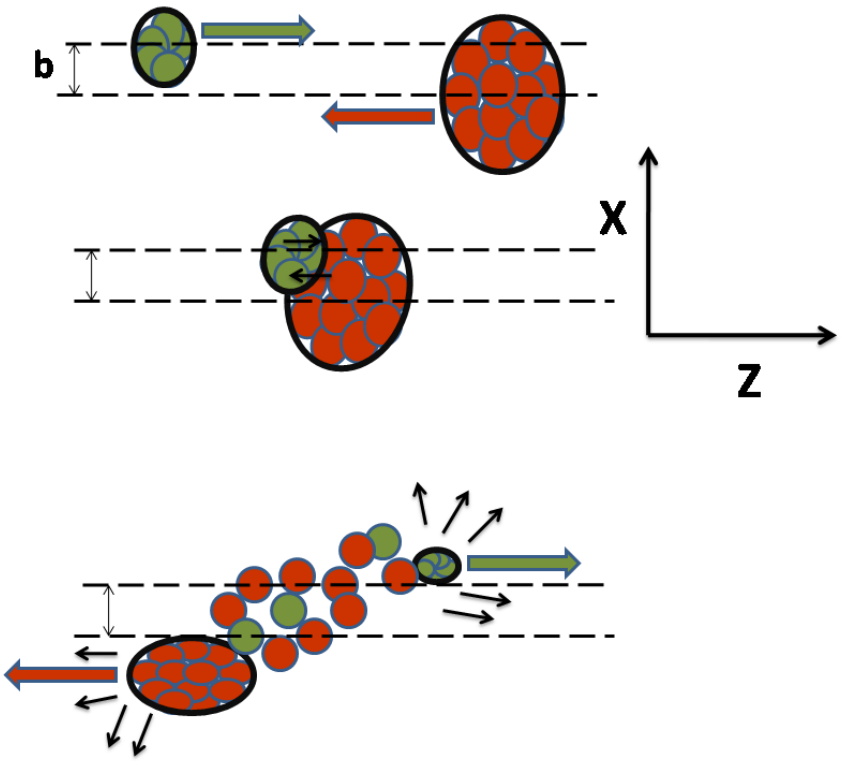

Figure 1.14: The representation of directed flow (v_1) for mass asymmetric reactions at intermediate energies.

1.5.4 Input parameters of the models and their relation to different observables

The theoretical study of the observable at intermediate energies is carried out using various transport models also called primary models along with clusterization techniques that are termed as secondary models. All the transport models have a common framework and vary however in the technicalities and the initialization of target and projectile. The input parameters of the model may be categorized into three types of parameters [80]:

(i)**Reaction Parameters**: incident energy, masses of the colliding nuclei, colliding geometry. They characterize the entire kinematics of a solitary event.

(ii) **Physics Parameters**: Gaussian width, parameters of potential involved, cross sections, collision term, Fermi momentum, Lorentz contraction of the coordinate distribution and so on. They compare to an itemized portrayal of interactions and might be altered to a sensible extent. These are the outcomes of comparisons being made between calculations and experiment.
(iii) **Technical Parameters**: minimum distance between two initialized nuclei, time step size, minimum collision distance and so forth. They are utilized to perform productive computations. The observables ought to be autonomous of them.

1.6 Experimental attempts

1.6.1 Experimental attempts for Multifragmentation

The first multifragmentation occasions, or all the more definitely, medium mass fragments $5 \leq A \leq 30$, were seen in collisions involving high energy proton beam, [81, 82] before the initiation of systematic studies that involved nucleus-nucleus collisions. The fragments were named as deep spallation products. In mid 80s investigations regarding multifragmentation were begun in HICs at intermediate energies [38]. An essential leap forward in the multifragmentation in this energy range was taken by utilizing 4π multidetector frameworks: ALADIN [83] and FOP1 [84,85] at GSI, AMPHORA at Grenoble [86], MINIBALL at MSU [87,88] and INDRA at GANIL [89]. A number of very informative studies were also performed by Purdue University group [82, 90] and Dubna group [91]. Purdue group, stated that the phenomenon of multifragmentation evolves the mixed liquid gas phase transition of nuclear matter. At the time of fragmentation the density becomes less than the density of normal nuclear matter. Warwick *et al.*, [92] concluded the fact that the multi-fragmentation is a dominant reaction channel if the incident energy is more than 35 MeV/nucleon.

The first accelerators to study multi-fragmentation were BEVALAC accelerator at Lawrence Berkeley Laboratory and Superconducting Cyclotron at MSU-NSCL, Michigan [93–97]. The main focus of the Berkeley group is the mass asymmetric nuclear reactions between energy range 50 to 110 MeV/nucleon. Its aim is to explore how the mass asymmetry entrance-channel affect reaction dynamics. Various pivotal denotations such

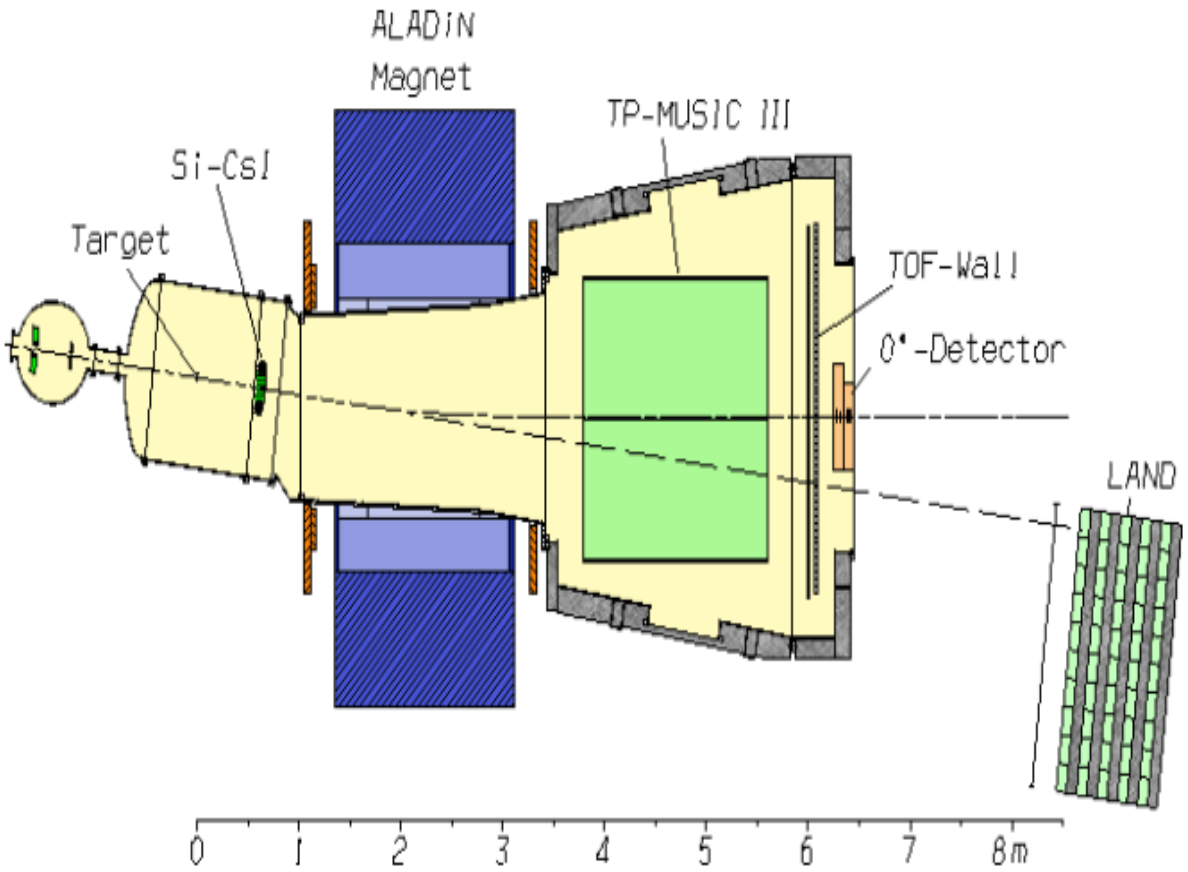

Figure 1.15: The cross sectional perspective of the ALADIN setup. The figure is taken from the Ref [100].

as symmetry energy, volume energy, entropy, surface energy, and so on [98, 99] for the asymmetric reactions are extricated in the energy region of 1 GeV/nucleon.

The ALADiN (A Large Acceptance Dipole magNet) [100] spectrometer was constructed to study projectile fragments created at relativistic energies. In the Fig. 1.15 beam entering from the left is first observed by the beam counters before arriving at the target. The entrance to the dipole magnet is surrounded by the Si-CsI(TI) array. The TP-MUSIC III detector and time-of-flight divider then follows and recognizes projectile fragments. Coincident neutrons produced roughly toward the course of the incident beam (dashed line) are identified with the Large Area Neutron Detector (LAND). The dash-dotted line represents the trajectory of beam particles after being deflected by an angle of 8^o. Freeze-out attributes of multifragmentation events delivered in central $^{129}_{54}$ Xe + $^{nat}_{50}$ Sn

reactions at various bombarding energies (50, 45, 39 and 32 MeV/nucleon) were assessed with the help of a simulation in light of the experimental information gathered by the 4π and INDRA multidetector. A quick rise in the fraction of nucleons discharged (in the vicinity of 32 and 45 MeV/nucleon) at freeze-out was derived. The presence of a constraint of excitation energy of nearly 3.0-3.5 MeV/nucleon for fragments was affirmed [101, 102]. Experimental data collected by the 4π multidetector INDRA was utilized to examine the IMFs ($Z \geq 3$) and light charged particle,LCP ($Z \leq 2$) generation in the collisions of $^{131}_{54}$Xe + $^{124}_{50}$Sn at semicentral and peripheral geometry and at incident energy of 50 MeV/nucleon. It was discovered that a considerable part of the observed LCPs and IMFs starts from the midvelocity zone. These fragments are believed to originate either from an instantaneous (preequilibrium) process or from a delayed however progressively affected emanation procedure [103].

Multi-fragment disintegration of $^{129}_{54}$Xe, $^{197}_{79}$Au and $^{238}_{92}$U projectiles in collisions with $^{9}_{4}$Be,$^{12}_{6}$C,$^{27}_{13}$Al,$^{64}_{29}$Cu, $^{115}_{49}$In, $^{197}_{79}$Au and $^{238}_{92}$U targets have been contemplated at energies lying between 400 and 1000 MeV/nucleon by using ALADIN forward-spectrometer at SIS. The dominant trait of the methodical arrangement of data is the Z_{bound} universality that is adhered to by the fragment multiplicities and interrelations. A linear scaling law is followed between the fragment multiplicity and the projectile mass [104]. In another study, the fragmentation phenomenon was examined by bombarding $^{197}_{79}$Au projectiles on the targets of $^{12}_{6}$C, $^{27}_{13}$Al and $^{64}_{29}$Cu at bombarding energy of $E = 600$ MeV/nucleon. Roughly all the projectile fragments with charge $Z \geq 2$ were detected using inverse kinematics method [105, 106]. Ogul *et al.,* [107] also studied the dependence of projectile fragmentation on N/Z with the ALADIN spectrometer. Radioactive ion beams of Sn and La were employed in order to explore many isotopic compositions. The global fragmentation observables depend weakly on the N/Z of the projectile whereas light fragments show a substantial dependence. Recently, Imal *et al.*, [108] have studied the production cross section and isotopic yield distributions of projectile like residues in the reactions $^{112}_{50}$Sn+$^{112}_{50}$Sn and $^{124}_{50}$Sn+$^{124}_{50}$Sn at GSI Laboratory and compared with the statistical multifragmentation model (SMM).

The National Superconducting Cyclotron Laboratory measured the interconnection between the multiplicities of detected IMFs and total charged particle for $^{84}_{36}$Kr + $^{197}_{79}$Au

reactions at beam energies from E = 35 to 400 MeV/nucleon. At central or near central geometry, fragment multiplicities are the highest for these impacts. The fragment production enhances up to $E \simeq 100$ MeV/nucleon, and then reduces at higher beam energies [88]. In another study multifragment deteriorations from $^{129}Xe +^{197} Au$ reaction at E =50 MeV/nucleon have been contemplated with a multidetector framework encompassing 88% of 4π in solid angle. The average number of IMFs ($Z = 3 - 20$) increments unequivocally as a component of charged particle multiplicity and achieves values greater than six for the most savage impacts. [109].

1.6.2 Experimental attempts for Nuclear Stopping

The level of nuclear stopping is an essential observable in deciding the result of a reaction and can be looked into by means of the rapidity distribution [110] and asymmetry of the momentum distribution of nucleons [111]. The experiment at the heavy-ion synchrotron SIS of GSI in Darmstadt, Germany, using the FOPI detector [112–114] presented the centrality dependence of the rapidity distribution of protons in isospin symmetric nuclear reactions with $A = 96$. Two stable isobaric nuclei having largest feasible N/Z difference,$^{96}_{44}$Ru + $^{96}_{40}$Zr were used. The results demonstrated incomplete mixing and partial transparency of the colliding nuclei at SIS energies. Even in the most central collisions and beam energy 0.4 and 1.5 GeV/nucleon, a global equilibrium is not attained.

A methodical investigation (excitation functions and system-size dependencies) of global stopping in the energy range extending from 0.09 to 1.93 GeV/nucleon was displayed by the FOPI collaboration. For the heaviest system, $^{197}_{79}$Au + $^{197}_{79}$Au, a plateau of maximal stopping is noticed reaching out from around 0.2 to 0.8 GeV/nucleon with a quick fall on both sides. The extent of stopping, which appears to remain essentially underneath the likelihood of a full stopping scenario, is observed to be exceedingly related to the quantity of sideward flow. This likewise gave a knowledge to comprehend in-medium impacts on mesonic and baryonic particles, since the effective densities in the early period of the collisions are required to be unequivocally identified with the extent of stopping [115]. Another investigation by the FOPI collaboration measured nuclear stopping for $^{58}_{28}$Ni+$^{58}_{28}$Ni, $^{129}_{54}$Xe+CsI, $^{40}_{20}$Ca+$^{40}_{20}$Ca, $^{197}_{79}$Au+$^{197}_{79}$Au and $^{96}_{44}$Ru +$^{96}_{44}$Ru reactions at incident energies running between 90 and 1930 MeV/nucleon [116, 117].

The experiments performed at the SIS synchrotron at GSI by FOPI and INDRA displayed consolidated information about excitation functions of stopping for $^{129}_{54}$Xe + $^{197}_{79}$Au reactions in the domain of energies from 40 MeV/nucleon to 1500 MeV/nucleon. They inferred that the flow-stopping correlation is associated with a density-pressure connection and it depicts a possibly fascinating requirement for microscopic simulations trying to extricate the nuclear EOS from HICs [118]. Nuclear stopping has also been explored in HICs at central geometry by interpreting kinematically accomplished events registered with the assistance of the 4π multidetector INDRA for an extensive assortment of symmetric reactions, $^{197}_{79}$Au+$^{197}_{79}$Au, $^{129}_{54}$Xe+ $^{118}_{50}$Sn, $^{58}_{28}$Ni+$^{58}_{28}$Ni. A quick decline is observed up to 40 MeV/nucleon (near Fermi energy) when stopping is plotted against the incident energy. For higher energies, the trend relies upon the mass of the combined system, demonstrating the rising involvement of two-body dissipation [119].

Lopez *et al.*, [120] assessed nuclear stopping from the measured isotropy ratio of protons for a vast collection of symmetric systems examined with the INDRA array at central geometry. They found that stopping is not complete, above E_{inc} = 30 MeV/nucleon, whatever the system size [120].

1.6.3 Experimental attempts for Transverse Flow

The 4π detectors namely, the Streamer Chamber [121] and the Plastic-Ball/Wall [122] at Bevalac in Berkeley gave the first experimental evidence for the occurrence of transverse flow [123]. The NSCL at Michigan State University, USA, firstly anticipated the isospin effects in the collective transverse flow for the systems $^{58}_{28}$Ni + $^{58}_{28}$Ni and $^{58}_{26}$Fe + $^{58}_{26}$Fe at an energy of 55 MeV/nucleon and observed that greater flow or negative deflection is displayed by neutron-rich system [124]. The energy of vanishing flow was found to be higher for neutron rich system at all colliding geometries. Ogilvie *et al.*, [125] reported on the experimental measurement of E_{bal} for $^{40}_{18}$Ar + $^{51}_{23}$V through NSCL. In an identical way, Krofcheck *et al.*, [126] stated the dissipation of transverse momentum flow in excitation function of $^{139}_{57}$La + $^{139}_{57}$La reactions and announced E_{bal} $\leq$50 MeV/nucleon for the same. Andronic *et al.*, [117] displayed experimental information on transverse flow in $^{197}_{79}$Au + $^{197}_{79}$Au collisions at semicentral geometry and incident energies from 90, 120, 150, 250, and 400 MeV/nucleon with broad phase-space coverage using the FOPI detector at GSI,

Darmstadt. In another investigation Andronic *et al.*, [127] introduced new experimental information on transverse flow for the systems $^{197}_{79}$Au + $^{197}_{79}$Au, $^{131}_{54}$Xe + $^{130}_{54}$CsI and $^{58}_{28}$Ni + $^{58}_{28}$Ni at beam energies extending from 90 to 400 MeV/nucleon. They examined the system and centrality dependence of integral and differential transverse flow of particles in accordance with charge. Another study (by FOPI collaboration) has been done by Trautmann *et al.*, [128] in which proton and neutron elliptic flows are measured and observed to be sensitive towards symmetry energy. As of late, FOPI collaboration measured the transverse rapidity distribution and radial flow in the reactions of $^{197}_{79}$Au + $^{197}_{79}$Au, $^{129}_{54}$Xe + $^{130}_{54}$CsI, $^{40}_{20}$Ca + $^{40}_{20}$Ca , $^{96}_{44}$Ru + $^{96}_{44}$Ru, $^{58}_{28}$Ni + $^{58}_{28}$Ni and $^{96}_{40}$Zr+$^{96}_{40}$Zr at central geometry and various bombarding energies running between 120 and 1.5 GeV/nucleon [116]. The directed flow of fragments for $^{64}_{28}$Ni + $^{64}_{28}$Ni, $^{70}_{30}$Zn + $^{70}_{30}$Zn and $^{64}_{30}$Zn + $^{64}_{30}$Zn systems is measured by Kohley *et al.*, [129] from NIMROD-ISiS (Neutron Ion Multiplicity for Reaction Oriented Dynamics with Indiana Silicon investigation Sphere) collaboration at Texas A and M University (TAMU) in the USA at 35 MeV/nucleon. The estimations have demonstrated that flow diminishes alongside an increment in the neutron content of a fragment.

1.7 Theoretical attempts

1.7.1 Theoretical attempts for Multifragmentation

Theoretically, there is little uncertainty that infinite nuclear matter experiences a transition from a liquid to a gaseous phase and supports a mixed phase equilibrium at temperatures up to around 17 MeV. The nuclear reaction being to a great degree erratic, the most direct way to infer the phase diagram appears to specifically think about it from the model in the wake of fitting the different parameters on the multifragmentation results. In the midst of the past couple of decades, the microscopic many-body approach and its relevance in nuclear physics has been improved significantly. These microscopic many-body approaches predominantly incorporate the non-relativistic BruecknerHartreeFock (BHF) approach [130–132], the relativistic DiracBruecknerHartreeFock (DBHF) approach [133–138], the self-consistent Greens function (SCGF) approach [139–141], and the variational many-body (VMB) approach [142–144]. Using statistical models one finds noteworthy fragmentation only if the densities diminish well beneath normal nuclear densities.

Subsequently, multifragmentation might be the test pointer that the critical/spinodal region in the phase diagram has been reached. The isospin effects in fragmentation were first studied by Zhang *et al.*, [145] for the reactions of $^{112,124}Sn + ^{112,124}Sn$ at 40 MeV/nucleon using IQMD model. The examination uncovered diverse scalings of IMFs with the quantity of neutrons and charged particles for above systems as is watched experimentally too. Liu *et al.*, [146, 147] also studied the isospin effects for the reactions of $^{76}_{30}$Zn + $^{40}_{18}$Ar, $^{76}_{36}$Kr + $^{40}_{20}$Ca, $^{120}_{54}$Xe + $^{40}_{20}$Ca, $^{120}_{48}$Cd + $^{40}_{18}$Ar at 100 MeV/nucleon and observed that neutron-poor system prompts huge number of IMFs contrasted with the neutron-rich systems. Peilert *et al.*, [148] researched diminished velocity correlation functions for fragments for the systems $^{56}_{26}$Fe + $^{197}_{79}$Au at 100 MeV/nucleon using the dynamical-statistical approach QMD + SMM. The emission time scales were under 500 fm/c and equivalent to the usual time a fragment requires to navigate a freeze-out volume of about five times the nuclear volume. Y. G. Ma *et al.*, [42] has examined the creation of fragments ($5 \leq A \leq 22$) for the reactions ^{40}Ar (25 to 150 MeV/nucleon) on ^{27}Al at central geometry by means of the molecular dynamical model. The distribtion of IMFs is discussed using power law function and exponential function.

M. Di Toro *et al.*, [149] studied the asymmetric effects in multifragmentation and depicted that dissipative heavy ion reactions, in particular fragment production reactions, at intermediate energies are rather sensitive to DDSE. The neutron-rich $^{124}_{50}$Sn + $^{124}_{50}$Sn and neutron-poor $^{112}_{50}$Sn + $^{112}_{50}$Sn reactions at 50 MeV/nucleon have been taken using stochastic transport approach. M. Colonna *et al.*, [150] examined the fragmentation properties of charge asymmetric systems at central geometry.

A comparative investigation of $^{100}Sn + ^{124}Sn$ and $^{100}Zn + ^{124}Sn$ collisions at incident energy of 30 and 400 MeV/ nucleon exclusively was carried out by B. A. Li *et al.*, [151]. The intensity of isospin transport/diffusion was considered by utilizing the rapidity distributions of free nucleons (FNs) and their isospin asymmetries. The effect of DDSE and MDIs on the production of fragments has been examined by Vinayak *et al.*, [152] for $^{197}Au + ^{197}Au$ for the full colliding geometry. The simulations infer a critical shift in the peak IMFs multiplicity. Kaur *et al.*, [47] exhibited an entire orderly theoretical investigation of multifragmentation for mass asymmetric reactions $^{16}_{8}$O+$^{136}_{54}$Xe, $^{28}_{14}$Si+$^{124}_{54}$Xe, $^{32}_{16}$S+$^{120}_{50}$Sn, $^{40}_{20}$Ca+$^{112}_{50}$Sn, $^{50}_{24}$Cr+$^{102}_{44}$Ru, $^{56}_{26}$Fe +$^{96}_{44}$Ru for the energies running between 50 and

600 MeV/nucleon by using both soft and hard nuclear EOS. A broad investigation of the fragmentation criterion of different mass asymmetric collisions was done by A. Sharma *et al.*, [153] by utilizing IQMD model and confronted their theoretical estimations with the accessible experimental information. In another investigation of the reactions of $^{40}_{18}$Ar+$^{45}_{21}$Sc and $^{84}_{36}$Kr+$^{197}_{79}$Au it was concluded that the onset of multifragmentation relies on the range of Coulomb forces and reaction asymmetry [154]. Puri *et al.*, [155,156] analyzed the fragment formation in $^{16}_{8}$O+$^{80}_{35}$Br collision at various incident energies extending from $E = 50$ MeV/nucleon to 200 MeV/nucleon. Recently, Wu *et al.*, [157] have talked about the competitiveness of symmetry and Coulomb potential for the mass asymmetric collision of $^{40}Ar + ^{197}Au$ at bombarding energies of 35, 50 and 100 MeV/nucleon. Their investigation uncovered that the above discussed competitiveness between the two potentials influence the emanation of FNs and LCPs in the projectile and target region.

The MDIs are additionally found to play an imperative role in multifragmentation [158–160]. The momentum dependence of interactions emphatically impact the production of fragments at peripheral geometry and the momentum fluctuations are valuable in figuring out the role of DDSE in proton/neutron rich systems. Zheng *et al.*, [161] have studied the de-excitation of an excited nucleus by using Gemini model. They found that the momentum fluctuation temperature shifts down due to sequential decay.

1.7.2 Theoretical attempts for Nuclear Stopping

Nuclear stopping administers a large portion of the dispersed energy and curbs the distinctive reaction procedures at various beam energies. To begin with, the first examination on nuclear stopping was done by Renfordt *et al.*, [123] for the system $^{40}_{18}$Ar+$^{207}_{82}$Pb at 0.772 Gev/nucleon at intermediate impact parameters in the vicinity of $b \sim 0.5b_{max}$ and announced complete nuclear stopping (and isotropy) for central collisions. Bauer *et al.*, [162] and Bertsch *et al.*, [163] have indicated that nuclear stopping in the HICs, is regulated by both the in-medium NN cross section as well as mean field, yet for this situation the mean field did not include symmetry potential. Zhang *et al.*, [164] directed a point by point examination of the wide excitation function of nuclear stopping with the help of IQMD model, and has been successful in accomplishing a decent concurrence with the INDRA and FOPI Collaborations experimental information.

E. Bonnet *et al.*, [119, 165] demonstrated that full nuclear stopping is accomplished for reactions at Fermi energies and that too for very central geometry. Central and midcentral collisions were researched, for the systems $^{129}_{54}$Xe + $^{119}_{50}$Sn at 25, 32, 39, 45, and 50 MeV/nucleon. B. A. Li *et al.*, [166] in their investigation hunt down potential probes of the isospin reliance of the in-medium NN cross sections. Liu *et al.*, [167] studied nuclear stopping for the reactions with various neutron proton ratios at incident energies extending from 15 MeV/nucleon to 150 MeV/nucleon. It is observed that, nuclear stopping is sensitive to in-medium NN cross section (its isospin dependence) but insensitive to symmetry term in the energy region starting from the Fermi energy to 150 MeV/nucleon. Q. Li *et al.*, [168] explored the reliance of nuclear stopping Q_{zz}/A and R on the isospin asymmetry of the original system, the isospin dependence of the medium correction of the two-body scattering cross section and the nuclear EOS (isospin-dependent part and incompressibility). Y. Zhang *et al.*, [169] investigated the effect of mean fields and in-medium NN scattering cross sections on flow and stopping by contrasting the outcomes of QMD computations with data on stopping, elliptical and directed flow. Fen Fu *et al.*, [170] researched the expansion speed and additionally the degree of nuclear stopping for $^{58}_{28}$Ni + $^{58}_{28}$Ni and $^{208}_{82}$Pb + $^{208}_{82}$Pb from 0.4 to and 1.2 GeV/nucleon using IQMD model and inferred that both have higher value for the heavier systems at full energy range. Yang *et al.*, [171] considered the entrance channel reliance of the isospin effects of nuclear stopping by utilizing an IQMD model with three various types of symmetry potentials. As of late Dhawan *et al.*, [41] explored the emanation of light complex particles, and degree of stopping for the reactions $^{197}_{79}$Au+$^{197}_{79}$Au , $^{20}_{10}$Ne+$^{20}_{10}$Ne, $^{139}_{57}$La+$^{139}_{57}$La, $^{40}_{20}$Ca+$^{40}_{20}$Ca, $^{93}_{41}$Nb+$^{93}_{41}$Nb and $^{58}_{28}$Ni+$^{58}_{28}$Ni at incident energies extending from 50 and 1000 MeV/nucleon utilizing hard EOS alongside free energy dependent NN cross section. Kumar *et al.*, [172, 173] conveyed an organized investigation of the influence of symmetry energy in the presence as well as absence of momentum-dependent interactions (MDI) on the global stopping. At low incident energies, the MDI and DDSE greatly affect the nuclear stopping.

Jain *et al.*, [174, 175] considered the impact of charge asymmetry and isospin-dependent cross section on nuclear stopping and multiplicity of FNs and LMFs for the reactions $^{124}_{m}$X+$^{124}_{m}$X, where m varies from 47 to 59 and for $^{40}_{n}$Y+$^{40}_{n}$Y, where n varies from 14 to 23. In their investigation, it was found that nuclear stopping depend firmly on

the isospin-dependent cross section. Vinayak *et al.*, [176] examined the impact of DDSE on nuclear stopping. Reactions were done for $^{40}_{20}$Ca+$^{40}_{20}$Ca, $^{58}_{28}$Ni+$^{58}_{28}$Ni and $^{124}_{50}$Sn+$^{124}_{50}$Sn for various isotopic compositions. It is observed that the nuclear stopping reduces with an increase in stiffness of DDSE. In Ref. [177] the density and temperature attained in HICs for various systems for different forms of the DDSE has been examined. Another effort was done by Kaur *et al.*, in Ref. [178] where nuclear stopping is analyzed in mass asymmetric reactions by keeping the combined mass of the system fixed. The reactions used were $^{56}_{26}$Fe + $^{96}_{44}$Ru ($\eta = 0.2$), $^{50}_{24}$Cr + $^{102}_{44}$Ru ($\eta = 0.3$), $^{40}_{20}$Ca + $^{112}_{50}$Sn ($\eta = 0.4$), $^{32}_{16}$S + $^{120}_{50}$Sn ($\eta = 0.5$), $^{28}_{14}$Si + $^{124}_{54}$Xe ($\eta = 0.6$), $^{16}_{8}$O + $^{136}_{54}$Xe ($\eta = 0.7$),. Maximum stopping is obtained for nearly symmetric reactions.

Jun Su *et al.*, [179] investigated the global nuclear stopping and the radial flow energy at Fermi energy for central impact parameter and defined a memory loss ratio to assess the residual memory and the deviation from the equilibrium.

1.7.3 Theoretical attempts for Transverse Flow

Stöcker *et al.*, [180] discussed strong-compression phenomena in fierce nucleus-nucleus collisions in nuclear fluid dynamics. Angular and energy distributions of fragments discharged from fast nucleus-nucleus collisions ($^{20}_{10}$Ne + $^{238}_{92}$U at 260, 400, and 800 Mev/nucleon) are computed with the utilization of nuclear fluid dynamics.

Li *et al.*, [181] have contemplated the isospin dependence of collective flow for the reactions $^{48}_{24}$Cr + $^{58}_{28}$Ni and $^{48}_{20}$Ca + $^{58}_{26}$Fe by using isospin-dependent Boltzmann-Uehling-Uhlenbeck (IBUU) model. Almost identical inferences are attained by Chen *et al.*, [182] by observing the flow of different fragments for the systems $^{58}_{28}$Ni + $^{58}_{28}$Ni and $^{58}_{26}$Fe + $^{58}_{26}$Fe at 55 MeV/nucleon. Li *et al.*, [183] also explored theoretically a new approach for estimating the strength of transverse flow in terms of the number of nucleons in the reaction plane emitted in the same and reverse directions of the flow.

Voloshin *et al.*, [184] examined the impacts of interplay of radial expansion of the thermalized system made in HICs and transverse flow. In another study, the function of MDIs in directed flow and its disappearance has been examined by Sood *et al.*, [185] for reactions at zero centrality over an extensive variety of masses running between 24 and 394. Gautam *et al.*, [186, 187] have concentrated on the impact of DDSE on flow and

balance energy.

Jain *et al.* [188] revealed the importance of MDIs and NN cross section on neutron-proton transverse flow for the systems $^{197}_{79}$Au + $^{197}_{79}$Au, $^{124}_{47}$Ag + $^{124}_{47}$Ag, $^{124}_{50}$Sn + $^{124}_{50}$Sn, $^{101}_{44}$Ru + $^{101}_{44}$Ru, $^{58}_{28}$Ni + $^{58}_{28}$Ni and $^{40}_{20}$Ca + $^{40}_{20}$Ca. Di Toro *et al.* [189] examined the neutron-proton directed and elliptic flow for the system $^{124}_{50}$Sn + $^{124}_{50}$Sn at beam energy of 1.5 GeV/nucleon. Recently, Bansal *et al.*, [190] have analyzed the part of momentum dependent EOS on directed flow and its disappearance.

Thus a lot of work has been done in examining multifragmentation, nuclear stopping and transverse flow in case of mass symmetric colliding systems but little attention has been paid towards mass asymmetric colliding systems. In the present work, we aim to look into the dynamics of mass asymmetric reactions, the density variations, isospin effects via. density dependent symmetry energy in the concerned systems. For this we have chosen multifragmentation and stopping as the two observables to be studied.

1.8 Organisation of thesis

The thesis arrangement is as follows:

In **Chapter 2**, a short study of different essential and optional models utilized as a part of the literature to examine the reaction dynamics has been presented. The QMD and IQMD models used to carry out the present investigation is talked about conscientiously. The chapter is trailed by clarification of different clusterization procedures.

In **Chapter 3**, the influence of input parameters on fragmentation observables has been analyzed by using two different dynamical transport models (QMD and IQMD). Author carried out an extensive survey of the different input ingredients in both the models. Our analysis reveals that the input parameters are mainly responsible for the difference between fragmentation observables like fragment yield, collision rate etc., calculated by using the phase space obtained from the two transport models. Our calculations show that isospin effects are important to study reaction dynamics. Therefore IQMD model has an edge over QMD model.

In **Chapter 4**, Author has performed a theoretical investigation of different mass-asymmetric reactions to access the direct impact of the DDSE on multifragmentation. The simulations have been performed for a specific set of reactions having same system mass and N/Z content, using IQMD model to estimate the quantitative dependence of fragment production on the mass-asymmetry factor (τ) for various symmetry energy forms. The dynamics associated with different mass-asymmetric nuclear reactions is explored and the direct role of symmetry energy is checked. Also a comparison with the experimental data (mass asymmetric reaction) is presented for different symmetry energy forms.

In **Chapter 5**, theoretical calculations have been performed within the framework of IQMD model to study a particular set of mass symmetric and asymmetric reactions (keeping total mass fixed) over an extensive variety of incident energies and colliding geometries. It has been observed that global as well as local nuclear stopping is strongly affected by the mass asymmetry of the reaction. Influence of density-dependent symmetry energy has been observed in local nuclear stopping. Global stopping decreases with the increase in colliding geometry. Effect of impact parameter on nuclear stopping is stronger at higher energies.

In **Chapter 6**, the outcomes are concluded followed by a future prospect of the work.

Chapter 2

Methodology

2.1 Introduction

The dynamics of HICs at intermediate energies is mainly commanded by the three ingredients, namely mean field, binary collisions and Pauli blocking. These ingredients play a major role at different bombarding energies and hence their knowledge is indispensable in obtaining information about the nuclear EOS. Undoubtedly, the Hartree-Fock (HF) approximation and Schrodinger equation serve as a beginning stage for any microscopic endeavor to describe nuclear structure and hence are suitable for low energy reactions [191–196]. Interestingly, Time-Dependent Hartree-Fock (TDHF) [197–199] calculations attempted to microscopically describe the dynamics of large nuclear systems, for example, HICs and fission. These calculations were very effective in depicting the scattering angles, fusion cross section, deep inelastic scattering, momentum transfer at energy $\leq$ 5 MeV/nucleon. This approximation fails, however at higher incident energies, because of absence of two body collisions. Later on, efforts have been reported in literature to update the original TDHF equation, viz. extended TDHF (ETDHF) [200] so as to incorporate the two body binary impacts by considering the remaining NN interactions. Erroneously, ETDHF cannot be utilized for the extensive calculations of HICs as it involves highly complex numerical implementation. On the other hand, contrary to the TDHF approach, the cascade model [201, 202] describes collisions at very high energy. It neglects mean field completely and take only NN collisions without taking Pauli-blocking into account. The HICs dynamics at intermediate energies feel necessity for an equal weightage of NN binary collisions and mean field. This calls for exact facts about the real (trajectory of nucleons) and imaginary (NN collisions) parts of the potential. The isospin degree of

freedom enters as real and imaginary part in terms of iso-vector (symmetry) potential, Pauli-blocking and in-medium NN cross-sections (isospin dependent), respectively.

In the accompanying segments, author first discusses in detail the QMD and IQMD models which create the phase space of nucleons. Different clusterization methods are talked about in the following part of this chapter.

2.2 QUANTUM MOLECULAR DYNAMICS MODEL (QMD)

The QMD [23] technique simulates HICs on an event-by-event premise, and consequently, include many-nucleon correlations. Along these lines, this model offers us a chance to determine not only one body observable but also many body phenomena like fragment formation. The primary QMD model was suggested by Aichelin and Stöcker [203]. Initial states of nuclei in terms of mean coordinates and momenta are assigned randomly so as to produce experimental ground state density profile and binding energy of the nucleus.

The model incorporates N-body correlations, an EOS and most essential quantum features, namely, the Pauli-principle, Stochastic scattering as well as particle production. It is based on an event by event method such that each event is simulated autonomous of other events.

2.2.1 Various Features of QMD model

QMD model involves three steps. Initially, one needs to create the nuclei. This procedure is called as *initialization*. It turns out to be important to make sure that our initialization do not destabilize the cold nuclei. For this, author will discuss some *initial checks for stability of nuclei.* Then nucleus is propagated under the influence of encompassing mean field. This method is called *propagation*. At last, the nucleons will undoubtedly impact in the event if they come excessively near to each other. This part is assigned as *NN collisions*. These NN collisions and mean field effects help in comprehending the role of *Pauli blocking*.

2.2.2 Initialization

QMD model goes beyond the conventional molecular dynamics approach by incorporating Pauli blocked collision term, so that the dynamics is identical to the manner in which actual motion in the nuclear system takes place. Further, spread out of each nucleon in space is denoted by the S-wave having Gaussian width, L fixed in the present model. In QMD model, the nucleons are characterized by Gaussian wave packets which associate by mutual two- and three-body forces. The model simulates the HICs by preserving the correlations and fluctuations between nucleons. Every nucleon is depicted by a rational state of the form

$$\psi_i(r,\ p_i(t),\ r_i(t)) \ = \ \frac{1}{(2\pi L)^{3/4}} exp\left[\frac{i}{\hbar}\ p_i(t)\cdot r \ - \ \frac{(r \ - \ r_i(t))^2}{4L}\right]. \tag{2.1}$$

The parameter L, is identified with the extension of the wave packet in phase-space. For more details related to L value, the reader can refer [80, 204–206]. The total N-body function is thought to be the immediate result of coherent states

$$\Phi \ = \ \prod\nolimits_i \psi_i(r,\ r_i, p_i, t). \tag{2.2}$$

Author does not utilize a Slater determinant (having $(A_P \ + A_T)!$ summation terms) and in this manner, disregard the anti-symmetrization. To start with, successful endeavors to simulate the HICs with anti-symmetrized states have been included for smaller systems [207–210]. As the model is semi-classical, so, in order to transit from quantum mechanical wave function to classical distribution function in phase space, the Wigner density distribution is used. The Wigner transforms of these coherent states are Gaussian in momentum as well as coordinate space. The Wigner density reads as

$$\begin{aligned} f_i(r,\ p, r_i(t),\ p_i(t)) \ &= \ \frac{1}{(2\pi\hbar)^3} \int e^{-\frac{i}{\hbar}p\cdot r_{12}} \psi_i(r + \frac{r_{12}}{2},\ t)\ \psi_i^*(r - \frac{r_{12}}{2},\ t) d^3 r_{12} \\ &= \ \frac{1}{(\pi\hbar)^3} e^{-(r\ - r_i(t))^2/2L}\ e^{-(p\ - p_i(t))^2 2L/\hbar^2}, \end{aligned} \tag{2.3}$$

where $r_i(t),\ p_i(t)$ characterize the center of the Gaussian wave packet in phase-space, while the squared width L is autonomous of the time. The density of i^{th} particle is

$$\begin{aligned} \rho_i(r) &= \int f_i(r,p,r_i(t),p_i(t))\ d^3p \\ &= \frac{1}{(2\pi L)^{3/2}}\ e^{-[r\ -\ r_i(t)]^2/2L}. \end{aligned} \tag{2.4}$$

The nucleus can be initialized by assigning the coordinates and momenta to all nucleons. In three dimensional space (inside a sphere of radius $R = 1.14\ A^{1/3}$, where A is the mass number of the nucleus under consideration), the centers of the Gaussian wave packet r_i are evenly distributed in polar coordinate by:

$$\begin{aligned} r &= R\ x_1^{1/3}, \\ cos\theta &= 1\ -\ 2x_2, \\ \phi &= 2\pi\ x_3, \end{aligned} \tag{2.5}$$

where $x_1,\ x_2,\ x_3$ are the random numbers. The coordinates of nucleons are discarded if the separation between them is less than 1.5 fm. The local Fermi momentum is given as

$$p_F(r_i) = \sqrt{-2mU(r_i)}, \tag{2.6}$$

where $U(r_i)$ is the local potential. The center of each Gaussian wave packet p_i is evenly distributed in polar coordinate

$$\begin{aligned} p_i &= p_F(r_i)x_4^{1/3}, \\ cos\theta &= 1\ -\ 2x_5, \\ \phi &= 2\pi x_6. \end{aligned} \tag{2.7}$$

where $x_4,\ x_5$ and x_6 are again random numbers. We dismiss those distributions where two nucleons are closer than some separation d_{min}. In other words, we require the fulfilment of the following condition

$$(r_i - r_j)^2 \, (p_i - p_j)^2 \geq d_{min}. \tag{2.8}$$

Taking into account the present criteria, 1 out of 50,000 initializations is acknowledged. As noted from Ref. [211–213], the phase-space distribution for the initialized nuclei in QMD concurs genuinely well with the experiments as well as with PPW+RPA approach (Pandharipande, Papanicolas and Wambach + Random phase approximation).

2.2.3 Propagation

Using relativistic kinematics, the effectively initialized nuclei are bombarded towards each other with appropriate center of mass velocity. This distribution is kept settled till the separation between the nuclei surfaces is 2 fm. By using a generalized variational rule, the equation of motion of the many body system is ascertained. One begins from the action

$$S = \int_{t_1}^{t_2} \mathcal{L}[\Phi, \Phi^*] d\tau, \tag{2.9}$$

having Lagrange function

$$\mathcal{L} = \langle \Phi | i\hbar \frac{d}{dt} - H | \Phi \rangle, \tag{2.10}$$

where the total time derivative incorporates the derivation with respect to the parameters.

$$\delta S = \delta \int_{t_1}^{t_2} \mathcal{L}[\Phi, \Phi^*] dt = 0. \tag{2.11}$$

The Hamiltonian H consist of a kinetic term and mutual interactions V_{ij}, which can be construed as the real part of the Brückner G-matrix. The time progression of the parameters is achieved by the condition that the action is stationary under permitted variation of the wave function. This produces an Euler-Lagrange condition for every parameter λ :

$$\frac{d}{dt} \frac{\partial \mathcal{L}}{\partial \dot{\lambda}} - \frac{\partial \mathcal{L}}{\partial \lambda} = 0. \tag{2.12}$$

This variation of the action produces the correct solution of the Schrödinger equation, only if the true solution of the Schrödinger equation is held in the confined arrangement of wave function $\psi_i(r, \ p_i(t), \ r_i(t))$. One should note here that the assemblage of wave

functions is not really a subspace of Hilbert-space, in this manner the superposition principle does not hold.

For the coherent states and a Hamiltonian of the form $H = \sum_i T_i + \frac{1}{2}\sum_{ij} V_{ij}$ (V_{ij} = potential energy, T_i = kinetic energy,), the Lagrangian and the variation can conveniently be figured out and we get:

$$\mathcal{L} = \sum_i \dot{r}_i p_i - \sum_{j\neq i} < V_{ij} > -\frac{3}{2Lm}, \tag{2.13}$$

$$\dot{r}_i = \frac{p_i}{m} + \nabla_{p_i} \sum_j < V_{ij} > \; = \; \nabla_{p_i} < H >, \tag{2.14}$$

$$\dot{p}_i = -\nabla_{r_i} \sum_{j\neq i} < V_{ij} >= -\nabla_{r_i} < H >, \tag{2.15}$$

with $r_i = r_i + \frac{p_i}{m}t$ and $\langle V_{ij}\rangle = \int d^3r_1 d^3p_2 \langle \psi_i^* \psi_j^* | V(r_1, r_2) | \psi_i \psi_j \rangle$.

These equations depict the time evolution and can be comprehended numerically. Hence, the variational principle reduces the time advancement of the n-body Schrödinger equation to the time advancement equations $6 \cdot (A_P + A_T)$. These equations have now demonstrated a similar structure as that of classical Hamiltonian equations.

$$\dot{p}_i = -\frac{\partial \langle H \rangle}{\partial r_i} \; ; \; \dot{r}_i = \frac{\partial \langle H \rangle}{\partial p_i}. \tag{2.16}$$

The numerical solution can be accomplished in the spirit of the classical molecular dynamics [214, 215]. The expectation value of total Hamiltonian can be perused as:

$$\begin{aligned} \langle H \rangle &= \langle T \rangle + \langle V \rangle \\ &= \sum_i \frac{p_i^2}{2m_i} + V_{Skyrme} + V_{Yuk} + V_{Coul} + V_{MDI}. \end{aligned} \tag{2.17}$$

where V_{Skyrme}, V_{Yuk}, V_{Coul} and V_{MDI} are, separately, the Skyrme (two and three body), Yukawa, Coulomb and momentum dependent potentials. The local Skyrme interaction is written as:

$$V_{Skyrme} = \frac{1}{2!} \sum_{j;i\neq j} V_{ij}^{(2)} + \frac{1}{3!} \sum_{j,k;i\neq j\neq k} V_{ijk}^{(3)}, \tag{2.18}$$

Here, $V_{ij}^{(2)}$ and $V_{ijk}^{(3)}$ are the two and three-body interactions. The two-body interactions when folded with the densities of both particles gives $V_{ij}^{(2)}$.

$$\begin{aligned}
\sum_{j;i\neq j} V_{ij}^{(2)} &= \sum_{j;i\neq j} \int f_i(r_i,p_i,t)\ f_j(r_j,p_j,t)\ V(r_i,r_j) \qquad (2.19)\\
&\quad \times d^3r_i\ d^3r_j\ d^3p_i\ d^3p_j,\\
&= \sum_{j;i\neq j} \int f_i(r_i,p_i,t)\ f_j(r_j,p_j,t)\ t_1\\
&\quad \times\delta(r_i-r_j) d^3r_i\ d^3r_j\ d^3p_i\ d^3p_j,\\
&= \sum_{j;i\neq j} t_1 \int f_i(r_i,p_i,t)\ f_j(r_j,p_j,t)\\
&\quad \times d^3r_i\ d^3p_i\ d^3p_j,\\
&= \sum_{j;i\neq j} t_1 \int \frac{1}{(\pi\hbar)^3} e^{-(r-r_i(t))^2/2L} e^{-(p-p_i(t))^2 2L/\hbar^2}\\
&\quad \times \frac{1}{(\pi\hbar)^3} e^{-(r-r_j(t))^2/2L}\ e^{-(p-p_j(t))^2 2L/\hbar^2}\ d^3r_i\ d^3p_i\ d^3p_j,\\
&= \sum_{j} t_1 \frac{1}{(4\pi L)^{3/2}} e^{-(r_i-r_j)^2/4L},\\
&= t_1 \sum_{j;i\neq j} \rho_{ij}. \qquad (2.20)
\end{aligned}$$

where

$$\rho_{ij} = \int d^3r\ \rho_i(r)\ \rho_j(r) = \frac{1}{(4\pi L)^{3/4}} e^{-(r_i-r_j)^2/4L}. \qquad (2.21)$$

The three-body interaction can be ascertained as follows :

$$
\begin{aligned}
\sum_{j,k;i\neq j\neq k} V_{ijk}^{(3)} &= \sum_{j,k;i\neq j\neq k} \int f_i(r_i,p_i,t)\ f_j(r_j,p_j,t)\ f_k(r_k,p_k,t)\ V(r_i,r_j,r_k) \\
&\quad \times d^3r_i\ d^3r_j\ d^3r_k\ d^3p_i\ d^3p_j\ d^3p_k, \\
&= \sum_{j,k;i\neq j\neq k} \int f_i(r_i,p_i,t)\ f_j(r_j,p_j,t)\ f_k(r_k,p_k,t)\ t_2 \\
&\quad \times\delta(r_i-r_j)\ \delta(r_i-r_k) d^3r_i\ d^3r_j\ d^3r_k\ d^3p_i\ d^3p_j\ d^3p_k, \\
&= \frac{t_2}{(2\pi L)^3\cdot 3^{3/2}} \sum_{j,k;i\neq j\neq k} e^{-\left[(r_i-r_j)^2+(r_i-r_k)^2+(r_k-r_j)^2\right]/6L}, \\
&= \frac{t_2}{(2\pi L)^3 3^{3/2}} \sum_{j,k;i\neq j\neq k} e^{-\left[(r_i-r_j)^2+(r_i-r_k)^2\right]/6L\times\frac{3}{2}}, \\
&= \frac{t_2\ (4\pi L)^{3/2\times 2}}{(2\pi L)^3\cdot 3^{3/2}} \left[\sum_{j\neq i} \frac{1}{(4\pi L)^{3/2}} e^{-(r_i-r_j)^2/4L}\right]^2, \\
&= \frac{t_2\ 2^3}{3^{3/2}} \left[\sum_{j\neq i} \rho_{ij}\right]^2 . \qquad (2.22)
\end{aligned}
$$

From above derivation, one can see that the three-body term depreciates to two body term. The finite range Yukawa term V_{Yuk} and a viable Coulomb interaction V_{Coul} are likewise included to account for different impacts and can be, read as:

$$V_{Yuk} = t_3 \frac{exp\{-|r_i-r_j|\}/\mu}{|r_i-r_j|/\mu}. \qquad (2.23)$$

$$V_{Coul} = \frac{Z_{eff}^2\ e^2}{|r_i-r_j|}. \qquad (2.24)$$

The Yukawa expression (with t_3= -6.66 MeV and μ=1.5 fm) has been included to enhance the surface properties of the interaction which are vital for multi-fragmentation. In nuclear matter where the density is consistent, the interaction density matches with the single particle density, $V_{loc}^{(2)}$, as well as $V_{Yuk}^{(2)}$,and are specifically proportional to $(\frac{\rho}{\rho_o})$. The three-body part $V_{loc}^{(3)}$ of the interaction corresponds to $(\frac{\rho}{\rho_o})^2$. In nuclear matter, the local potential energy has the form

$$V_{loc} = \frac{\alpha}{2}\left(\frac{\rho}{\rho_o}\right) + \frac{\beta}{\delta+1}\left(\frac{\rho}{\rho_o}\right)^2. \qquad (2.25)$$

There are two free parameters (α and β) and are fixed by the requirement that both the average binding energy ought to be -16 MeV and aggregate energy ought to have a minimum at normal nuclear matter density, ρ_o. With a specific end goal to examine the impact of different compressibilities, the above potential energy (eqn.2.25) can be generalized to

$$V_{loc} = \frac{\alpha}{2}\left(\frac{\rho}{\rho_o}\right) + \frac{\beta}{\delta+1}\left(\frac{\rho}{\rho_o}\right)^{\delta}. \tag{2.26}$$

This equation gives rise to the nuclear EOS which associate the pressure and energy [23, 216, 217]. In the investigation of HICs one generally utilizes the Skyrme parameterization of the nuclear EOS, containing two sets of parameters giving the same correct binding energy and saturation density, yet, two distinctive incompressibility K, one compares to soft EOS with $K = 200$ MeV (at smaller values of δ), another relates to hard EOS with $K = 380$ MeV (at bigger values of δ).

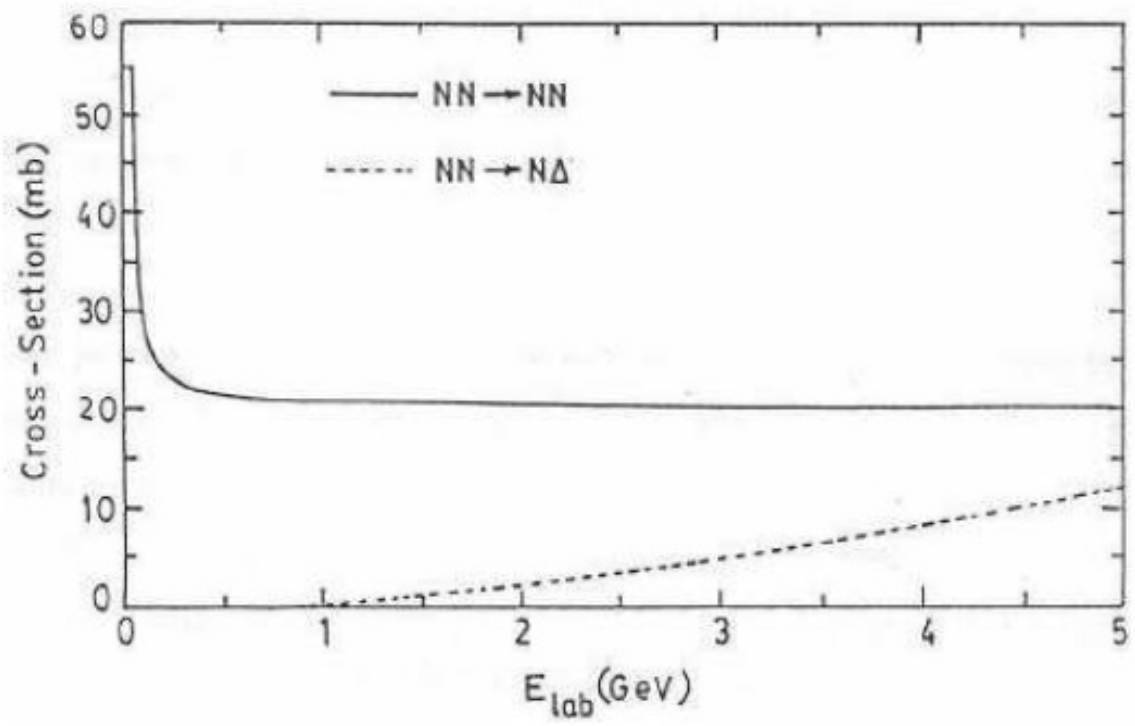

Figure 2.1: The Cugnon parameterization for the elastic (solid line) and inelastic (dashed line) cross sections of nucleon-nucleon scattering as a function of the incident energy E_{lab}. Figure is taken from Ref. [201].

Table 2.1: Parameters of static potentials [23]

K(MeV)	$\alpha(MeV)$	$\beta(MeV)$	δ	EOS
200	-356	303	1.17	Soft(S)
380	-124	70.5	2	Hard(H)
200	-390	320	1.14	SMD
380	-130	59	2.09	HMD

When the MDIs are presented, the parameters of Skyrme interactions need to be readjusted to have accurate saturation properties of normal nuclear matter and the similar incompressibility as those of hard and soft EOS. The new parameters set including momentum dependence are called SMD and HMD, individually. Table 2.1 lists these four sets of parameters along with the incompressibilities.

2.2.4 The nucleon-nucleon (NN) collisions

During the propagation, a collision is said to occur if two nucleons come in close proximity to each other. The impact of many body collisions is observed to be reasonably little, subsequently, we disregard the many body collisions [218,219]. The binary collisions in QMD model are dealt with in the same way as in BUU model. Two particles experience a collision, if they are nearer than a separation $\sqrt{\frac{\sigma^{tot}(\sqrt{s})}{\pi}}$.

This collision is furthermore subject to the satisfaction of Pauli principle. If the final state of scattered nucleons violates the Pauli principle, the collision is said to be blocked. Here $\sigma^{tot}(\sqrt{s})$ depict the total NN cross section and $\sqrt{s}$ implies center-of-mass energy and is characterized below. The employed cross sections in QMD model have been parametrized by Cugnon [201] on experimental data. All nucleons communicate with the same cross section irrespective of isospin. The total cross section ($\sigma^{tot}(\sqrt{s})$) is the sum of cross sections for elastic and inelastic channels.

$$\sigma_{tot} \;=\; \sigma_{el} \;+\; \sigma_{inel} \;=\; \sigma_{el} \;+\; \Sigma_{channels}\sigma_i \tag{2.27}$$

For elastic channels, the total and differential cross section (labeled as σ^{el}) is:

$$\sigma_{nn}^{(el)}(\sqrt{s}) = \begin{cases} 55(mb) & \text{if}\sqrt{s} < 1.8993 \\ \frac{35}{1+100(\sqrt{s}-1.8993)} + 20 & \text{if}\sqrt{s} \geq 1.8993, \end{cases} \tag{2.28}$$

with $\sqrt{s}$, the NN center of mass energy represented as:

$$\sqrt{s} = \sqrt{(E_1 + E_2)^2 - (P_1 + P_2)^2}. \tag{2.29}$$

Here E_i and P_i $(i,\ j = 1, 2)$ are the energy and momentum of a nucleon respectively. The angular distribution of these channels is given by [201]:

$$\frac{d\sigma}{dt} = ae^{bt}\ ; \qquad t = -2p^2(1 - cos\theta). \tag{2.30}$$

On the other hand, for inelastic channels, NN $\rightarrow$ N Δ the total cross section labeled as σ^{in} is expressed as

$$\sigma^{(in)}_{nn\rightarrow n\Delta}(\sqrt{s}) = \begin{cases} 0 & \text{if}\sqrt{s} < 2.015 \\ \frac{20(\sqrt{s}-2.015)^2}{0.015+(\sqrt{s}-2.015)^2} & \text{if}\sqrt{s} \geq 2.015. \end{cases} \tag{2.31}$$

The angular distribution of inelastic channels is considered to be invariant with respect to direction. The limit of $\sqrt{s}$=1.8993 GeV (in Eqn. 2.28) is based on the fact that the mass of two nucleons is roughly equal to 1.876 GeV. Therefore, for two colliding nucleons having very small velocity, a constant cross section (= 55 mb) is used. The mass limit of the inelastic channel (i.e. Δ formation in Eqn. 2.31) is based on the fact that mass of $\Delta(= N + \pi)$, is 1.076 GeV. Therefore, for $NN \rightarrow N\Delta$ channel, the outgoing mass should be at least 1.076 + 0.938 GeV.

The graphical representation of the elastic and inelastic components of the cross section is shown in Fig. 2.1. The energy dependence of the NN cross section exhibits that the elastic cross section drops strongly and saturates around 20 mb. On the other hand, the inelastic cross section increments straightly with incident energies. The NN cross section is dominated by the inelastic channels at high energies.

2.3 ISOSPIN-dependent QUANTUM MOLECULAR DYNAMICS MODEL (IQMD)

The IQMD model developed by Hartnack *et al.*, [80] is also a semi-classical model recreating HICs theoretically on an event by event premise, where nucleons of the colliding nuclei (target and projectile) interact by means of two and three body mutual interactions. As this model is based on dynamical picture and carries essential physics, and therefore it is

able to explain the phenomena of collective flow [187], multi-fragmentation [220], nuclear stopping [119], particle production [221] and isospin dynamics [186] etc. It treats the distinctive charge states of nucleons, deltas and pions. The isospin degree of freedom goes into the model by means of NN scattering cross section, Coulomb potential as well as symmetry potential (similar to that in IBUU model). Since it is an augmentation of the QMD model, so it also consists of three steps of initialization, propagation and collisions.

In IQMD model, a hadron is depicted in terms of single particle Wigner density

$$f_i(\vec{r},\vec{p},t) = \frac{1}{\pi^3\hbar^3} \cdot e^{-(\vec{r}-\vec{r_i}(t))^2\frac{2}{L}} \cdot e^{-(\vec{p}-\vec{p_i}(t))^2\frac{L}{2\hbar^2}}. \tag{2.32}$$

The hadrons propagate using classical Hamilton equations of motion:

$$\frac{d\vec{r_i}}{dt} = \frac{\partial\langle\ H\ \rangle}{\partial p_i} \ ; \ \frac{d\vec{p_i}}{dt} = -\frac{\partial\langle\ H\ \rangle}{\partial r_i} \tag{2.33}$$

where r_i and p_i (i= 1 to $A_T + A_P$, A_T and A_P being the mass of the target and projectile separately) are the position and momentum coordinates of individual nucleons and H stands for the Hamiltonian which is demonstrated by

$$\begin{aligned}\langle\ H\ \rangle = \langle\ T\ \rangle + \langle\ V\ \rangle &= \sum_i \frac{p_i^2}{2m_i} + \sum_i \sum_{j>i} \int f_i(r,p,t) V^{ij}(r',r) \\ &\times\ f_j(r',p',t) dr dr' dp dp'\end{aligned} \tag{2.34}$$

The in-medium NN interaction potential comprises of the real part of the Br*ü*ckner G-Matrix with an extra Coulomb interaction among the charged particles. Here V^{ij} contains a total of numerous terms: a contact interaction of Skyrme type with t_1 and t_2 parameters which are determined by the prerequisite that the Hamiltonian of above condition ought to reproduce the EOS in infinite nuclear matter restrains, a limited-range Yukawa term with $t_3 = -6.7$ MeV, Coulomb interaction potential, a momentum-dependent interaction with parameters $t_4 = 1.57$ MeV and $t_5 = 5 \times 10^{-4} MeV^{-2}$, and a symmetry contact interaction with a strength of $t_6 = 100$ MeV that distinguishes between protons and neutrons. The potential is represented as:

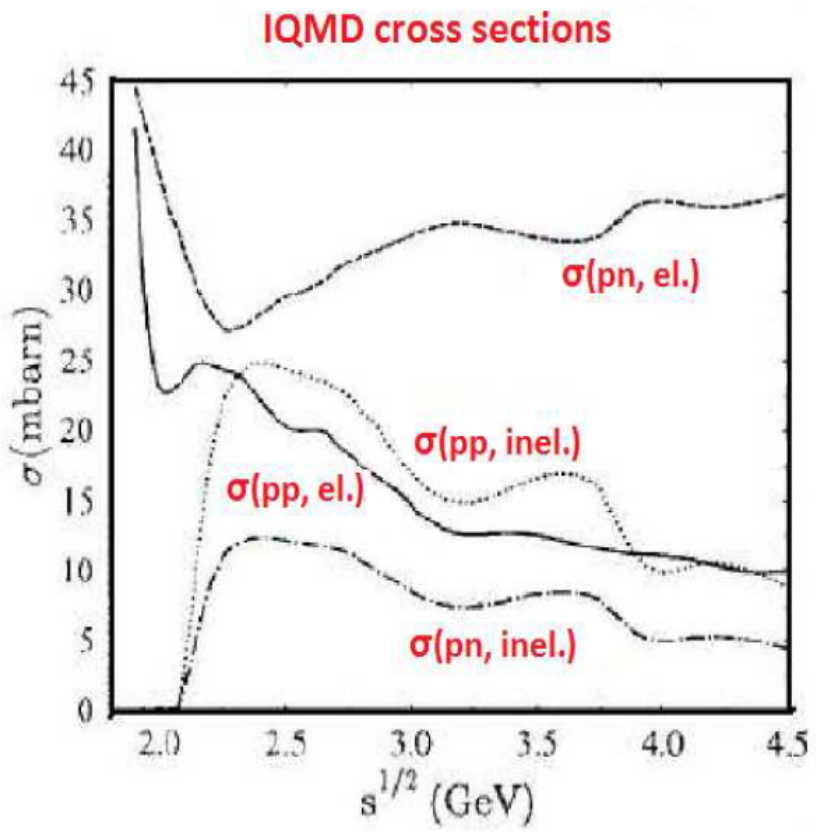

Figure 2.2: The elastic and inelastic cross-sections for proton-proton (pp) and proton- neutron (pn) utilized as a part of IQMD. The neutron-neutron (nn) cross-section is thought to be equivalent pp. The total cross-section is equivalent to entirety of elastic and inelastic cross-section. This figure is taken from Ref. [222].

$$
\begin{aligned}
V^{ij}(r'-r) &= V_{ij}^{Skyrme} + V_{ij}^{Yukawa} + V_{ij}^{Coulomb} + V_{ij}^{MDI} + V_{ij}^{Symmetry} \\
&= \left(t_1\delta(\vec{r}'-\vec{r}) + t_2\delta(\vec{r}'-\vec{r})\rho^{\gamma-1}\left(\frac{\vec{r}'+\vec{r}}{2}\right)\right) \\
&\quad + t_3\frac{exp(|\vec{r}'-\vec{r}|/\mu)}{(|\vec{r}'-\vec{r}|/\mu)} + \frac{Z_iZ_je^2}{|\vec{r}'-\vec{r}|} \\
&\quad + t_4 ln^2[t_5(\vec{p_i}'-\vec{p})^2+1]\delta(\vec{r_i'}-\vec{r}) \\
&\quad + t_6\frac{1}{\varrho_0}T_3^iT_3^j\delta(\vec{r_i}'-\vec{r_j})
\end{aligned}
\tag{2.35}
$$

where Z_i and Z_j indicate the charges of the i^{th} and j^{th} baryon and T_3^i and T_3^j are the corresponding isospin projection (i.e. 1/2 for protons and -1/2 for neutrons). The parameters μ and $t_1, ..., t_6$ are changed in accordance with the real part of the nucleonic

optical potential.

For ground state nucleus, the expectation value of the total Hamiltonian needs to be compared to its aggregate binding energy. On looking at the IQMD formalism and comparing it with the Bethe-Weizsacker mass formula it turns out to be certain that the volume energy is enhanced by kinetic energy $< T >$, the Skyrme interactions, and the MDIs, the surface and the volume energy by the Yukawa interaction, and the volume symmetry energy by the symmetry interactions [223]. Furthermore, parametrized free *np* and *pp* cross-sections are utilized in place of an averaged NN cross section. The respective strength of different cross-sections is depicted in Fig.2.2. The total cross-section is the aggregate of the elastic and all inelastic cross-sections.

$$\sigma_{tot} \;=\; \sigma el \;+\; \sigma_{inel} \;=\; \sigma_{el} \;+\; \Sigma_{channels}\sigma_i \tag{2.36}$$

The following inelastic reactions may impact the dynamics of the reaction and are explicitly considered:

$$\begin{aligned}
&N\;N \rightarrow\; \Delta\;N\;(hard-delta\;generation) \quad (a),\\
&\Delta \rightarrow\; N\;\pi\;(delta\;decay) \qquad\qquad\qquad (b),\\
&\Delta\;N \rightarrow\; N\;N\;(delta\;absorption) \qquad\quad (c),\\
&N\;\pi \rightarrow\; \Delta\;(soft-delta\;generation) \qquad (d).
\end{aligned} \tag{2.37}$$

Elastic $\pi\;-\;\pi$, $\pi\;-\;N$, $\pi\;-\;\Delta$, $\Delta\;-\;\Delta$, $\Delta\;-\;N$ scattering is most certainly not considered. The processes (a) and (d) and the elastic N-N collisions utilize experimental cross-sections [224, 225]. Unapproachable reactions like ΔN$\rightarrow\; NN$ are ascertained from their invert reactions (here $NN\;\rightarrow\;\Delta N$) using modified detailed balance formula [226]. However, the traditional method is only true for particles with boundless lifetimes (zero width). The elastic NN scattering angular distribution is taken to be [201]

$$\frac{d\sigma_{el}}{d\Omega} \;\approx\; exp\left[A(s)t\right], \tag{2.38}$$

where t is $-q^2$, the transverse momentum exchange and

$$A(s) \;=\; 6\frac{\left[3.65\left(\sqrt{s}-1.8766\right)\right]^6}{1+\left[3.65\left(\sqrt{s}-1.8766\right)\right]^6}. \tag{2.39}$$

Table 2.2: a(s) and b(s) as a function of the c.m. energy

$x = \sqrt{s}\ (GeV)$	$a\ (fm)$	b
2.104 - 2.12	$294.6(x-2.014)^{2.578}$	$19.71(x-2.014)^{1.551}$
2.12 - 2.43	$\frac{0.01224}{(x-2.225)^2 + 0.004112}$	$19.71(x-2.014)^{1.551}$
2.43 - 4.50	$\left(\frac{2.343}{x}\right)^{43.17}$	$33.14\ arctan(0.5404(x-2.146)^{0.9784})$

$\sqrt{s}$ is the c.m energy in GeV and A is given in $(GeV/c)^{-2}$.

The isospin degree of freedom has an imperative influence, particularly in the particle production. The employed inelastic channels $NN \rightarrow NN^*,\ N\Delta$ and $\Delta\Delta$ are dealt with in an undifferentiated manner. The parameterization proposed by Huber and Aichelin [227] is utilized: fitted differential cross-sections are extracted from one-boson-exchange (OBE) calculations:

$$\frac{d\sigma_{in}}{d\Omega} \approx a(s)exp\left[b(s)cos\theta\right]. \tag{2.40}$$

The $a(s)$ and $b(s)$ are functions of $\sqrt{s}$ and fluctuate in their definition for various interims of $\sqrt{s}$ (see table 2.2). θ is the polar angle.

2.4 Numerical Testing for the stability of nuclei for both QMD and IQMD model

One cannot expect the model calculations for heavy-ion collisions to be reliable, if the initialized projectile and target nuclei do not exhibit ground state properties. The nuclei prepared within transport model may start emitting nucleons after the lapse of hundred fm/c. Therefore, it is very important to make sure that our initialization does not destabilize the cold nuclei. Extensive tests were conducted by Heidelberg-Nantes-Frankfurt-Tubingen-Chandigarh groups to study the properties of different single nuclei. On the characteristic time scale of the nucleus-nucleus collision, the root mean square radius of nucleus should not change considerably, otherwise initialization of stable nucleus would not be valid. We have also carried out various checks by calculating the time evolution of root mean square radius and the momentum of four nuclei having mass from Ne to Au.

Fig.2.3 shows the time evolution of the root mean square radius profiles of IQMD model. Though there are oscillations around the mean value for the heavy nuclei, no nucleons are produced. On the other hand light nuclei (like Ne) are a little less stable.

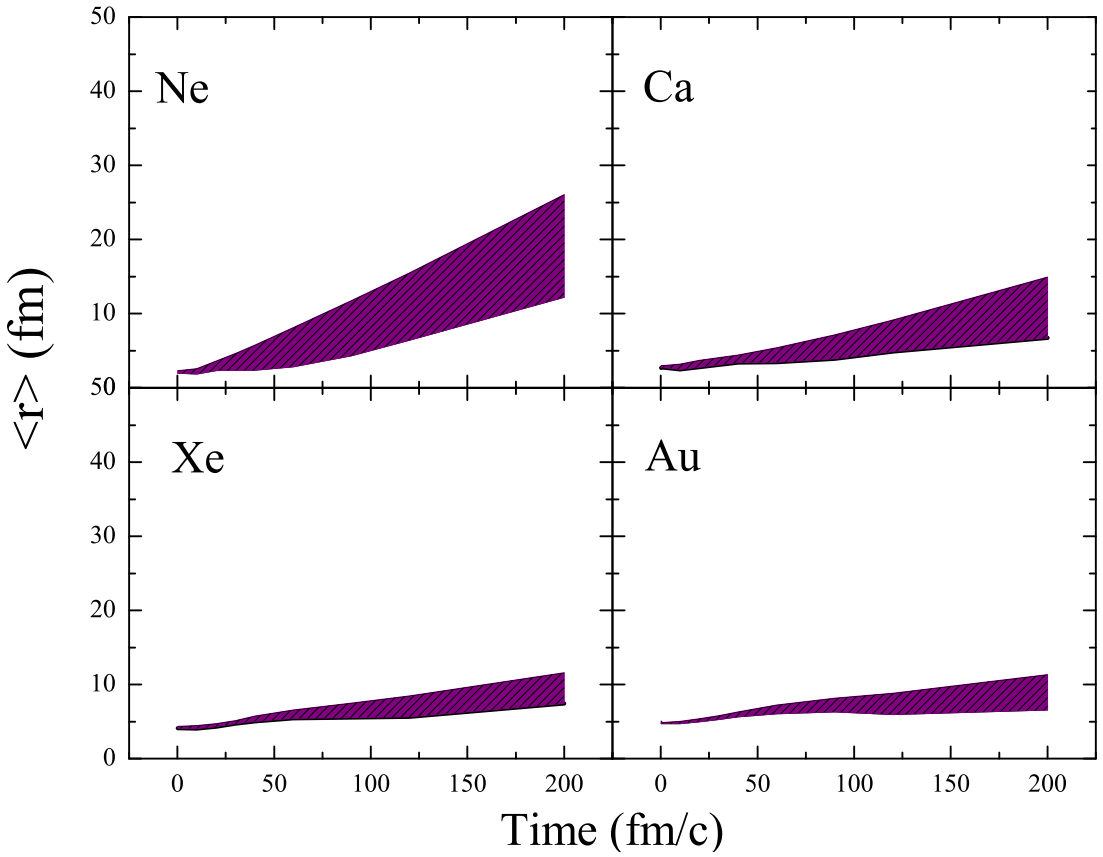

Figure 2.3: Time evolution of the root mean square radius of nuclei. For each nucleus we exhibit the radius for ten different initializations.

The emission of nucleons starts taking place at the time scale of 200 fm/c on the grounds that these light nuclei do not have appreciable local density. Nevertheless, one can see that most of the nuclei remain stable for a couple of hundred fm/c, which is adequate for the present calculations. The similar trend is for momentum profiles depicted in Fig.2.4.

The role of input ingredients of both the models on various observables is investigated in the next chapter.

2.5 Secondary models : Clusterization Algorithms

The models mentioned in the previous section are "primary models" that are used to create the phase-space of nucleons. Further, we need to have "secondary models" to clusterize the nucleons into fragments. These clusterization methods are discussed briefly in the following section.

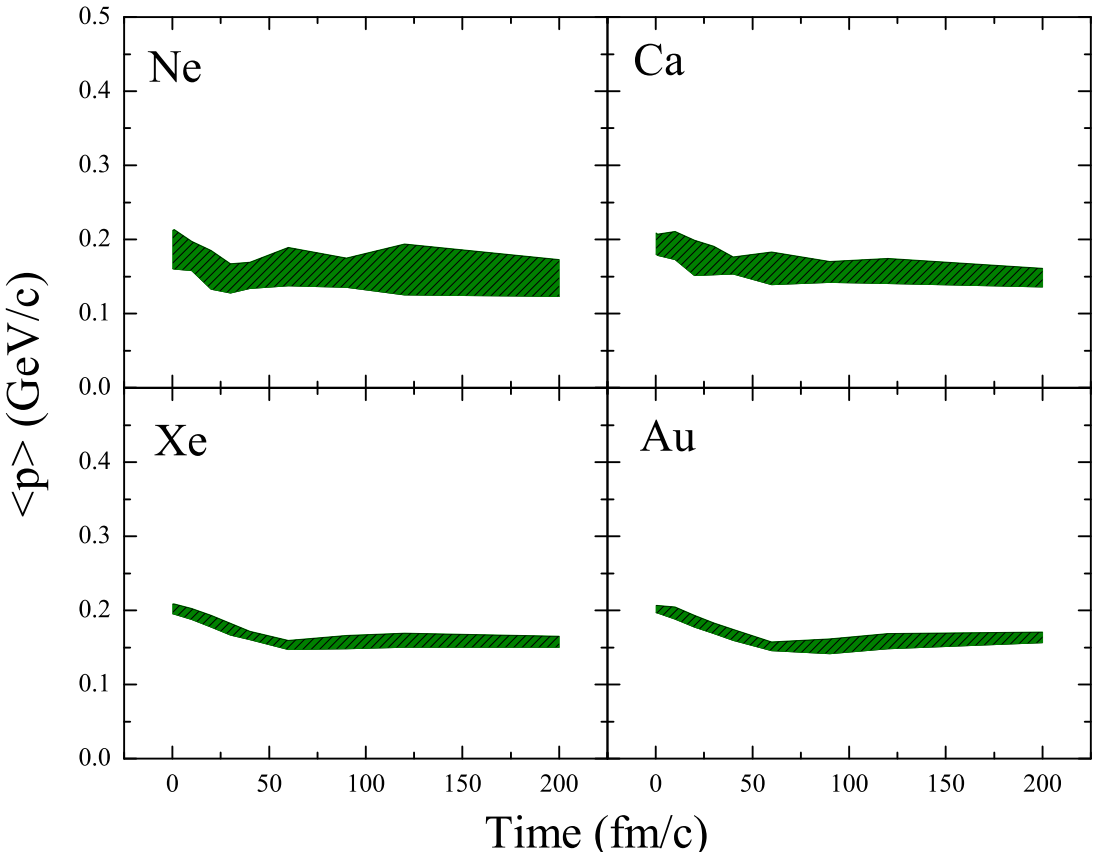

Figure 2.4: Time evolution of the average root mean square momentum of nucleons in IQMD model.

2.5.1 Minimum Spanning Tree Algorithm (MST)

We are familiar with the fact that the molecular dynamical models are widely used to consider the creation of the fragments and their stability in HICs because of the fact that the correlations and fluctuations among the nucleons in these models are preserved. One however, needs secondary algorithms to identify the fragments. Earlier attempts consist of identification of the fragments on the basis of their spatial correlations named as MST algorithm [23].

In order to clusterize the nucleons, the MST method is most extensively used [23, 217, 228–232]. In this method, two nucleons share the same fragment if their centroids are nearer than a specific separation d_{min},

$$|\mathbf{r}_i - \mathbf{r}_j| \leq d_{min}, \tag{2.41}$$

where $\mathbf{r}_i$ and $\mathbf{r}_j$ are the spatial positions of the two nucleons. The minimum distance d_{min} has been utilized as a free-parameter which changes between 2-4 fm for both IQMD and QMD model.

The fundamental drawback of this technique is that only correlations in coordinate space are utilized, disregarding totally the impact of momentum. This approach cannot identify the fragments that are practically overlapping and subsequently, will give a solitary huge fragment at a very early stage in the reaction where density is still high and the nucleonic interactions are still dynamic. Therefore, the MST clusters give inaccurate data when the system is still dense, and are important only at saturation stage, when the system is a dilute blend of free particles and cool fragments.

2.5.2 Minimum Spanning Tree with Momentum Constraints (MSTM)

Along with the confinement in the spatial space of nucleons in Eq. 2.36, another restriction introduced by Kumar *et al.*, [233] is put in the momentum space of nucleons i.e.

$$|p_i - p_j| \leq p_F \tag{2.42}$$

Here, p_F is the average Fermi momentum of nucleons bounded in a nucleus in its ground state for IQMD model ($\approx$ 268 MeV/c) and QMD model ($\approx$ 150 MeV/c).

This impromptu creation checks the development of artificial and unstable fragments by barring those nucleons having relative momenta larger than p_F . Eventually, MST and MSTM methods give distinctive outcomes towards the beginning of a reaction. MST gives one biggest cluster of size ($= A_P + A_T$), while MSTM technique gives two particular clusters of masses A_P and A_T having extensive relative momenta. This algorithm recognizes the largest fragment A_{max} as ahead of schedule as 50-60 fm/c [233].

Chapter 3

Influence of parameterizations on multifragmentation and flow

3.1 Introduction

The HICs at intermediate energies enables us to contemplate various observables that are useful indicators of the properties of the nuclear matter under the exorbitant conditions of density and temperature. During the reaction colliding nuclei compress each other and heat the matter [66, 234] prompting breaking of the matter into many pieces comprising of FNs, LMFs and IMFs and so forth during expansion phase. This breaking of colliding nuclei also led to numerous speculation regarding the occurrence of liquid vapour phase transition of nuclear matter [235]. After extensive study of fragmentation both experimentally [104] and theoretically [236], it has been concluded that fragmentation pattern depends on the size of the colliding accomplices, isospin content, isospin dependent NN cross section, beam energy as well as impact parameter. Theoretically, multi-fragmentation can be studied using various transport models also called primary models along with clusterization techniques that are termed as secondary models. The transport models can be classified broadly on the basis of isospin. Those including isospin effects are:

(i) Isospin Dependent Quantum Molecular Dynamics Model (IQMD) [80]: an isospin dependent version of QMD [23] model which is based on N-body theory and successful in dealing with fragmentation and flow,

(ii) Isospin Dependent Boltzmann Uehling Uhlenbeck Model (IBUU) [181]: an isospin dependent version of BUU model [237] based on Vlasov dynamics and the two body collision term and

(iii) Stochastic Mean Field Model (SMF) [238]: based on mean-field transport theory with the inclusion of stochastic forces.

The models without isospin effects are:
(i) Time Dependent Hartree Fock Theory (TDHF) [198]: a mean field theory,
(ii) Extended Time Dependent Hartree Fock Theory (EDTHF) [200]: an extended version of TDHF and considers residual interactions accountable for two body collisions,
(iii) Boltzmann Uehling Uhlenbeck Model (BUU) [237]: based on semiclassical appproximation of TDHF i.e. Vlasov equation and two body collision term and
(iv) Quantum Molecular Dynamics Model (QMD) [23]: based on a many-body framework which traces the motion of each nucleon and successful in dealing with the phenomena of fluctuation such as the fragment formation to list a few.
Lots of literature is available regarding the relative advantages and shortcomings of dynamical models. A comparative study of transport models with 800 MeV/nucleon La + La data was carried out by rescaling free space NN cross section and modifying collision components indicating a need for modification of nuclear transport properties at high densities in Ref. [239]. Another effort in this direction was made by Toshiki *et al.,* [240] by introducing an effective Pauli potential in the model. Ono *et al.,* [241] has given a concise outline of most generally utilized models and is successful in bringing out their relative merits and shortcomings. The discussion has highlighted the need for the development of quantal transport theory in an efficient manner. Liu *et al.,* [242] studied the impact of medium amendment of an NN cross section (isospin dependent) on multifragmentation within the framework of IQMD model highlighting the reliance of fragmentation on isospin impact. In this chapter, author has concentrated on the numerical realization of QMD and IQMD model by altering various input ingredients. Although IQMD is an extension of QMD model but its implementation is inspired from the VUU-model. Hence it differs slightly from QMD model, in all three aspects namely initialization, propagation and collision. The most important difference of IQMD model with respect to QMD is in its initialization. For the portrayal of energy supplied to each nucleon as a function of density, Skyrme parameterizations are used in both the models. This potential is based on the supposition that there exist two and three body interactions between the nucleons.

The finite range Yukawa term (with $t_3 = -6.7$ MeV) is imperative to achieve the surface stability of a finite nucleus. This potential has short range in IQMD model, with its range $\mu = 0.4$ fm whereas in QMD, the value of μ is 1.5 fm. The momentum dependent part of the NN interaction V_{mdi}, may alternatively be utilized in both the models. In the QMD model, we have used effective charge (Zeff) for all nucleons (without distinguishing between protons and neutrons). On the contrary, in the IQMD model, real charge of nucleons is utilized , for example, $Zproton = 1$ and $Zneutron = 0$, and thus the Coulomb term is treated as isospin-dependent. In addition to these potentials, a symmetry potential has been included in IQMD model which is not included in QMD model.
Besides the parameterizations depicting the NN potential, NN cross sections also play a significant role. In QMD model, collision occurs by respecting the Pauli principle whereas in IQMD model, there is a provision for both isospin explicit and isospin averaged Pauli blocking. The isospin explicit and isospin averaged Pauli blocking shed light on the dependence of NN collision on isospin. In IQMD, the centroids of Gaussian wave packets in a nucleus are arbitrarily dispersed in a phase-space sphere ($r \leq RA^{1/3}$) and ($p \leq p_F$) where R = 1.12 fm for ground state density, $\rho_o = 0.17$ fm $^{-3}$ whereas in QMD, R=1.14 fm corresponding to ground state density of $\rho_o = 0.15\ fm^{-3}$. In IQMD, the Fermi momentum (P_F) is dependent on the initial density without any local constraints, whereas in the QMD model, it is determined by the local binding energy. Another difference in the IQMD with respect to the QMD is in the Gaussian width L of the initialized nucleons, which is a measure of interaction range of the nucleons. In the QMD model, L is independent of system mass, whereas, in the IQMD model, L varies with mass of the system. However, optimization of Gaussian width has been carried out for fragmentation in Ref. [80,204,205,216,222,223,243]. It should be noted here that Gaussian width in both the models is taken to be fixed whereas in actual practice L is time dependent. We are familiar with the fact that the preservation of the interconnection and variations between nucleons aids in contemplating the fragment formation using molecular dynamical models. The study on other phenomena like transverse flow, elliptical flow, triangular flow, quadrupole flow, local thermalization and global nuclear stopping, R_E^{global} also counts on isospin of colliding nucleons.

In the present chapter, the motive of our study is two fold:

(i) To study the effect of initialization parameters on collision dynamics and fragment production using IQMD and QMD models.
(ii) To explain why IQMD model has edge over QMD model in case of multifragmentation and flow.

3.2 Results and discussion

In this work, the reactions ${}^{48}_{20}Ca + {}^{48}_{20}Ca$, ${}^{89}_{36}Kr + {}^{89}_{36}Kr$, ${}^{124}_{50}Sn + {}^{124}_{50}Sn$, ${}^{197}_{79}Au + {}^{197}_{79}Au$, ${}^{40}_{18}Ar + {}^{45}_{21}Sc$, ${}^{86}_{36}Kr + {}^{93}_{41}Nb$, ${}^{58}_{28}Ni + {}^{58}_{28}Ni$ are simulated at different incident energies for central collisions. We have taken neutron rich stable combinations to study the influence of isospin effects due to potentials and NN cross sections. Most of the calculations are carried out at incident energy 400 MeV/nucleon where the role of Pauli blocking is minimum and the impact parameter is kept central for maximum overlap of target and projectile nuclei. Soft EOS alongside energy dependent cross section in QMD as well as isospin dependent cross-section in IQMD have been used. MST method [23] is used to clusterize the phase space created by both IQMD and QMD models. The need for the present investigation is to see the influence of isospin effects due to potentials and NN cross sections.

3.2.1 Allowed collisions and average density

Initially, we focus on how collisions are affected over the time evolution of the reaction. In Fig. 3.1, we display the time evolution of allowed collisions for the system ${}^{197}_{79}Au + {}^{197}_{79}Au$ at bombarding energy of 400 MeV/nucleon and central impact parameter using both QMD and IQMD models. The influence of Pauli blocking on collision dynamics of the reaction has been checked. The isospin explicit and isospin averaged Pauli blocking incase of IQMD model has been depicted by black (dash line) and red (solid line). The isospin explicit Pauli blocking takes into account the isospin effects such that there is a clear distinction between the neutrons and protons whereas the isospin averaged Pauli blocking does not take into account the isospin effects and hence there is no distinction between neutrons and protons. The isospin averaged Pauli blocking in IQMD is similar to the Pauli blocking incorporated in QMD (blue dotted line). As both the models are dynamical models, the number of collisions respecting the Pauli principle (peak value) are almost same. However, the collision time of the reaction varies for both the models. The total passing time of

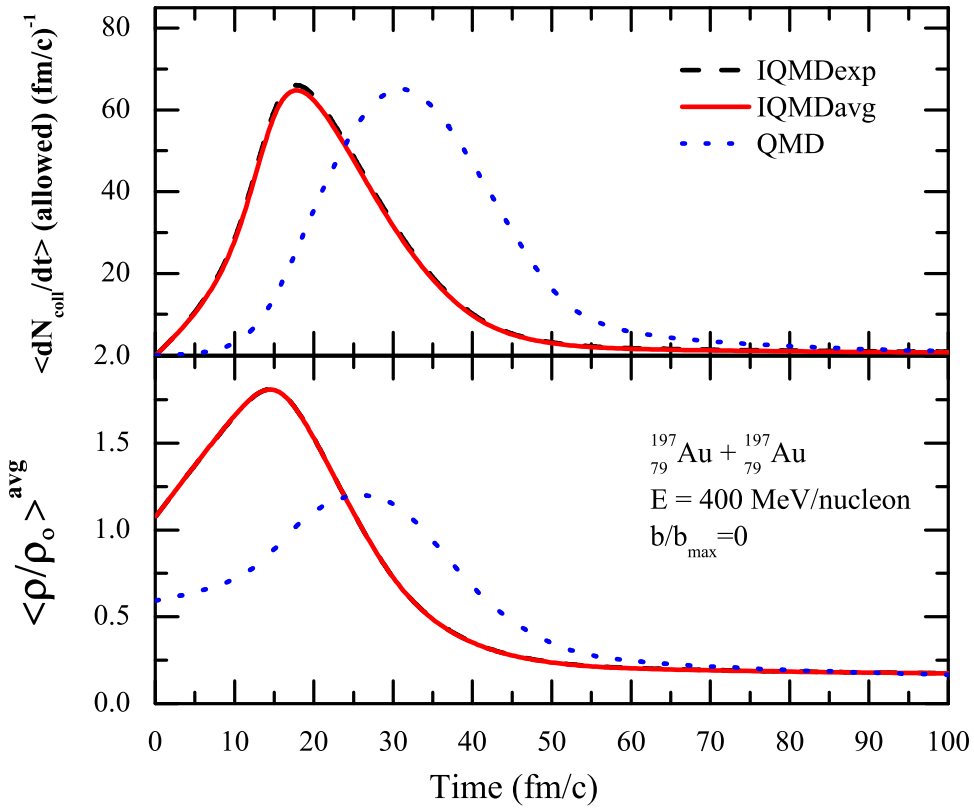

Figure 3.1: Allowed collisions and average density for the reaction $^{197}_{79}Au$+$^{197}_{79}Au$ at incident energy E = 400 MeV/nucleon and scaled impact parameter $\hat{b} = 0$ for both QMD and IQMD model.

the two nuclei is about 25 fm/c. The offset of 14 fm/c of QMD with respect to IQMD is due to the fact that in IQMD there is a boost factor of 0.4. The nucleons are randomly distributed in a momentum space sphere having radius depending on the corresponding Fermi momentum. The average value of Fermi momentum in the case of QMD model is 150 MeV/c whereas in IQMD model it is 268 MeV/c. In the lower panel of the figure, average density of the combined system normalized with normal nuclear matter density, ρ_o is illustrated as a function of time. The density of the i^{th} particle is given as:

$$\rho_i(r,t) = \sum_i^{A_{tot}} \frac{1}{(2\pi L)^{3/2}} e^{-[\mathbf{r}-\mathbf{r_i}(t)]^2/2L}. \tag{3.1}$$

where $r_i(t)$ is the centroid of i^{th} particle in coordinate space and A_{tot}= A_P + A_T. Here

$$\rho(r,t) = \sum_i^{A_{tot}} \rho_i(r,t). \tag{3.2}$$

is the total density in coordinate space. The starting point in the case of both the models represent normal nuclear matter density corresponding to two individual nuclei before collision. At this point there is no overlapping of the two nuclei. The initialization conditions in both the models are different as already discussed in the introduction of this chapter. Thereafter, participant zone starts to build up and is earlier in the case of IQMD model.

3.2.2 Incident energy dependence of NN collisions

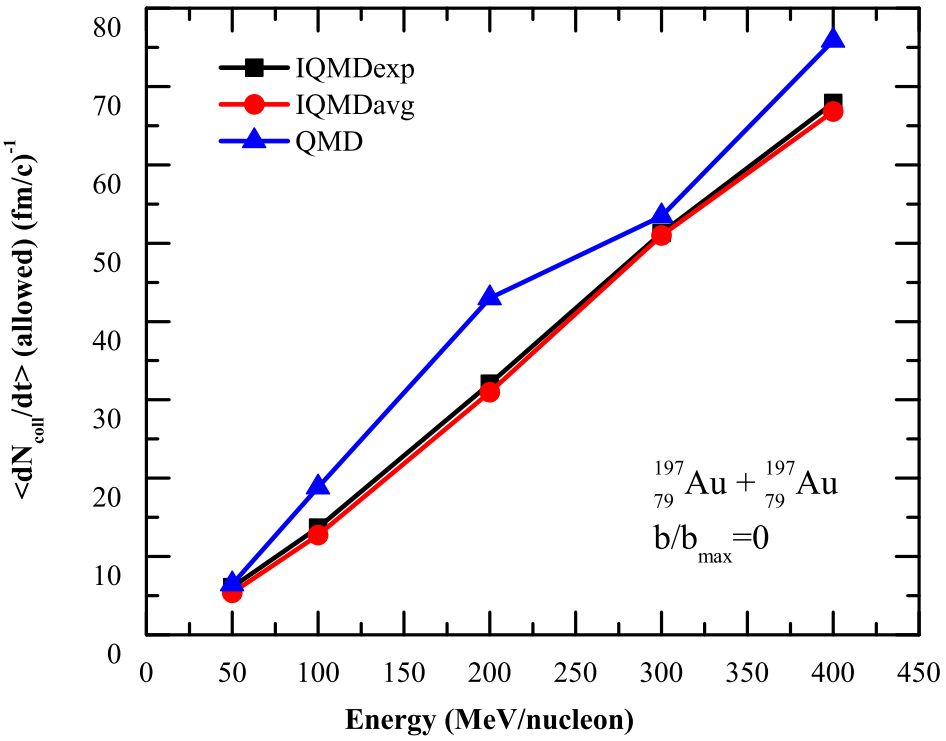

Figure 3.2: Incident energy dependence of allowed collisions for the reaction $^{197}_{79}Au +^{197}_{79} Au$ at scaled impact parameter $\hat{b} = 0$ for both QMD and IQMD model.

In Fig. 3.2, the allowed collisions are plotted against incident energy for the same systems as in Fig. 3.1. Effect of Pauli blocking has been studied at different incident energies. It has been observed that the number of collisions incase of QMD model is more than IQMD model at all incident energies. This is because the modeling of Pauli blocking is different in both the models. Differences may easily result from small differences of

how the occupation of the phase space is calculated. Moreover, the parameterization of Yukawa and Coulomb is different in both the models. The momentum dependent potentials are absent in both the models in the scenario discussed here. Due to large scale along y-axis difference between isospin explicit and isospin averaged Pauli blocking is not visible. More prominent difference due to Pauli blocking can be seen in the next section.

3.2.3 Impact parameter dependence of allowed collisions

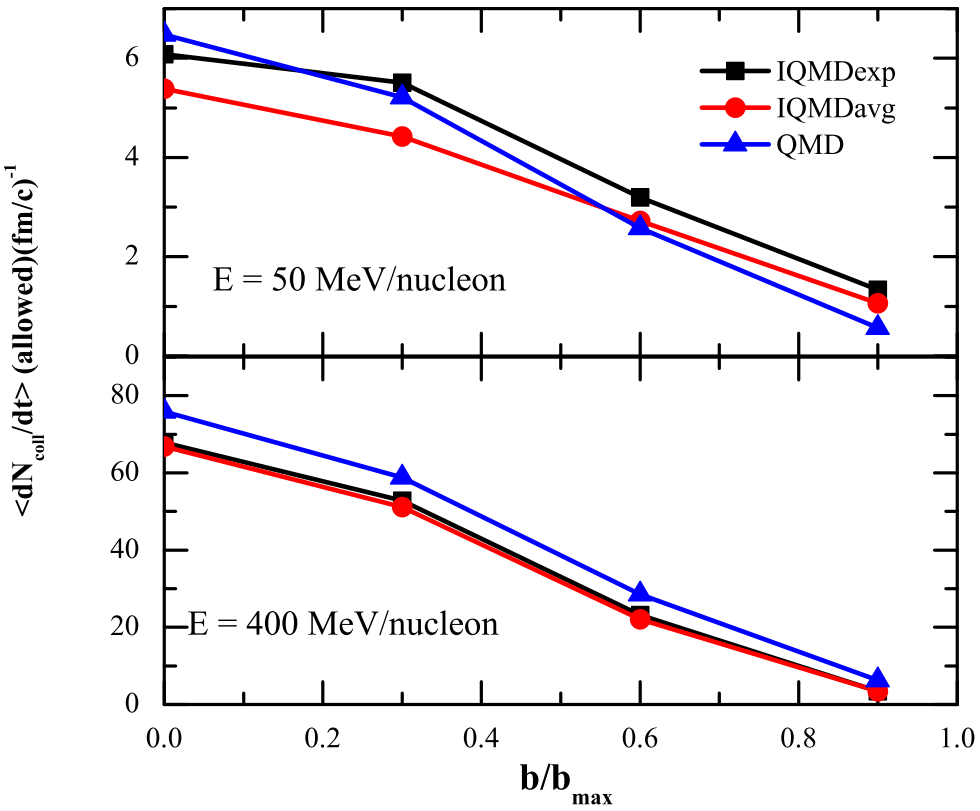

Figure 3.3: Geometry dependence of allowed collisions using both QMD and IQMD model.

The impact parameter dependence of allowed collisions is displayed in Fig. 3.3 highlighting the effect of Pauli blocking at low as well as high energy (E = 50 and 400 MeV/nucleon). It basically shows that at 50 MeV/nucleon most collisions are blocked because the relative shift of the momentum distributions of the two Fermi spheres is not large enough to permit many collisions. As the impact parameter increases, the effect of Pauli blocking decreases at both the energies. With the increase in impact parameter the

overlap between the projectile and target nuclei decreases thereby affecting the overall collisions in the reaction.

3.2.4 System mass dependence of allowed collisions

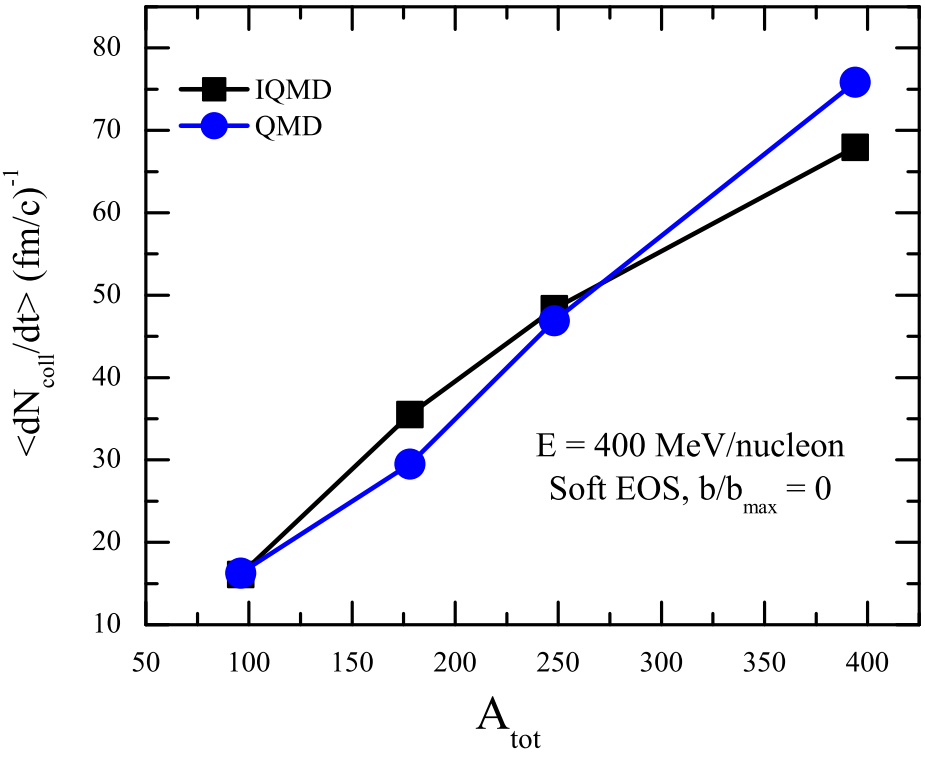

Figure 3.4: System mass dependence of allowed collisions for the ${}^{48}_{20}Ca + {}^{48}_{20}Ca$, ${}^{89}_{36}Kr + {}^{89}_{36}Kr$, ${}^{124}_{50}Sn + {}^{124}_{50}Sn$, ${}^{197}_{79}Au + {}^{197}_{79}Au$ at an bombarding energy of 400 MeV/nucleon and scaled impact parameter, $\hat{b} = 0$ with soft EOS.

It is evident from Fig. 3.4, that the collision rate increases as the system mass increases. This is because in the case of heavier nuclei interaction volume is more for large number of nucleons compared to that of light nuclei. Each nucleon of projectile sees fewer target nucleons and there are fewer projectile nucleons in the case of lighter nuclei. As one move from lighter to heavier systems the collision rate for mass ($A_{tot} = 394$) in IQMD model becomes lesser than the collision rate for the same mass in QMD model. This is because in QMD model the interaction range of the nucleons (Gaussian width) is fixed whereas in IQMD model it is mass dependent. This has been incorporated to achieve maximum stability of nucleus. As the mass of the nucleus increases, the interaction

range of the nucleons also increases, but the increase in the volume of the nucleus is not proportional to the increase in the number of nucleons for a given mass. Since the minimum distance for collision is fixed, the increase in the Gaussian width of nucleons beyond mass ($A_{tot} = 250$) prohibits the collisions due to Pauli blocking and the collision is not successful. The increase in the Gaussian width of nucleons leads to overlapping of the two Gaussians and hence Pauli blocked. Besides Pauli blocking, the variation in the input parameters like incident energy, colliding geometry (radius of the colliding nuclei and impact parameter), different NN cross section and so forth influence the rate of collisions. In IQMD model, isospin dependent cross section is used (σ_{iso}) whereas in QMD model, Cugnon [201] cross section (σ_{cug}) is used, which is an isospin independent cross section. We have also checked for isospin independent cross section (σ_{noiso}) in case of IQMD model and found that in case of IQMD model the rate of collisions becomes closer to QMD model especially for the higher mass. One should note here that the parameterization of Cugnon cross section (σ_{cug}) in QMD model is different from isospin dependent cross section (σ_{iso}) in IQMD model. This implies that the isospin effects are responsible for the variation in the values of observables calculated from IQMD model when compared to QMD model.

3.2.5 System mass dependence of the yield of $A = 4$ fragments

Fig. 3.5, shows the system mass dependence of multiplicity of fragments $< M_{A=4} >$ having mass ($A = 4$). Here the potentials depending on isospin were switched off and then added one by one to see their influence. The fragment yield for IQMD model without Coulomb and Symmetry potential (IQMDcofsof) is being compared to the fragment yield for QMD model without Coulomb potential (QMDcof) in panel (a). The panel (b) depicts the fragment yield for IQMD model without Coulomb potential and with symmetry potential corresponding to stiffness factor ($\gamma = 0.66$) i.e. IQMDcofs0.66 as well as QMD model without Coulomb potential i.e. QMDcof. Here we have chosen the value of stiffness factor ($\gamma = 0.66$) based on the previous theoretical results [244]. The panel (c) depicts the comparison of fragment production with the addition of Coulomb potential and absence of symmetry potential in both the models i.e.,(IQMDconsof and QMDcon). The panel (d) depicts the comparison of fragment production between IQMD model including Coulomb

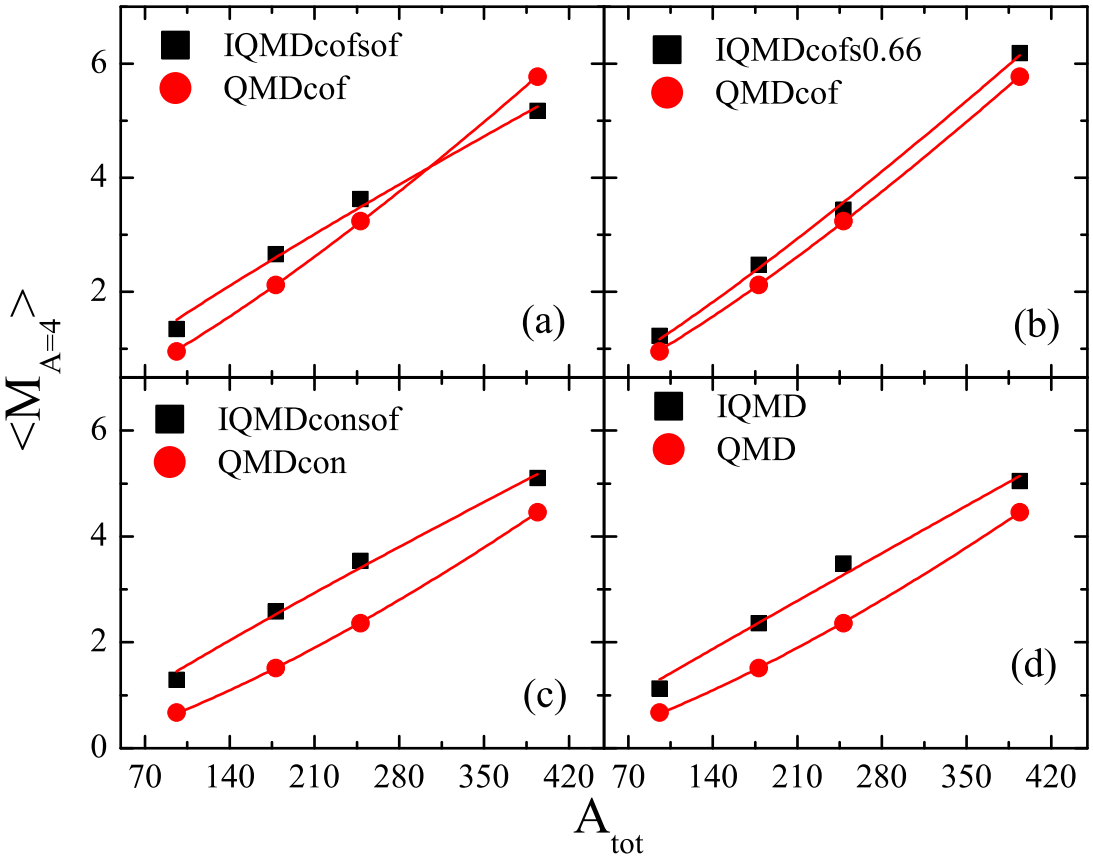

Figure 3.5: System mass dependence of the yield of $A = 4$ fragments for the ${}^{48}_{20}Ca + {}^{48}_{20}Ca$, ${}^{89}_{36}Kr + {}^{89}_{36}Kr$, ${}^{124}_{50}Sn + {}^{124}_{50}Sn$, ${}^{197}_{79}Au + {}^{197}_{79}Au$ at an incident energy of 400 MeV/nucleon and $\hat{b} = 0$ with Soft EOS.

and Symmetry potential (IQMD) and QMD model including Coulomb potential (QMD). Here, rather than opting for fragments of certain mass range, we have taken fragment with mass ($A = 4$) into account. Although the same clustering criteria MST, [23] is implemented on the phase space generated by both the models, but the Fermi momentum associated with nucleons and the distribution of particles in phase space is entirely different in both the models. The Fermi momentum incase of IQMD model is 268 MeV/c whereas incase of QMD model it is 150 MeV/c. The MST method clusterizes the nucleons in such a way that their centroids lie closer than a minimum distance, d_{min}

$$|\mathbf{r}_i - \mathbf{r}_j| \leq d_{min}, \tag{3.3}$$

where $d_{min} = 4fm$. The mass dependence of mass ($A = 4$) fragment clearly depicts power law behaviour for a fixed energy of 400 MeV/nucleon in the present study and is

applicable to all light mass fragments.

We have designated the fragments emitted from hot zone (high density region or participant zone) as mass ($A = 4$) fragment and those emitted from cold zone (low density region or spectator zone) as IMFs ($5 \leq A \leq A_{total}/6$). Due to increase in number of participant, an increase in multiplicity of those fragments will always be observed which originate from the participant zone. However, if we carefully look at the trend from both the transport models, we see that the differences between the calculations is decreased but not eliminated. Because initialization procedure of both models is different. Moreover, the difference keeps on increasing with the addition of different components of potentials as we move from panel (a) to panel (b) followed by panel (c) and finally panel (d). The continous involvement of different potentials give extra repulsion to the impacting nuclei incase of IQMD model leading to production of more lighter mass fragments in comparison to QMD model. This difference in the fragment yield of two models, because of various set of potentials elucidates the criticalness of isospin dependent Coulomb and symmetry potential in HICs. It can be inferred from the figure that the presence of isospin dependent Coulomb and symmetry potential together affect the fragment production [157, 245].

3.2.6 System mass dependence of multiplicity of IMFs ($< M_{IMF} >$) for the same reactions

It would be interesting to also see the influence of input ingredients of both the models on the production of fragments that originated from the spectator zone. In Fig. 3.6, author presents the system mass dependence of multiplicity of IMFs, $< M_{IMF} >$ for the same reactions as in Fig. 3.5. The multiplicity of FNs, light mass fragments and intermediate mass fragments ($< M_{FN} >$, $< M_{LMF} >$ and $< M_{IMF} >$ respectively) exhibit a power law of the form cA_{tot}^{τ} with the system mass autonomous of the mass of the fragments as well as incident energy and impact parameter. Here A_{tot} is the total system mass at all beam energies and colliding geometries [246]. The fragments have been constructed on the basis of spatial correlations of nucleons using MST algorithm. The nucleons are considered to be the part of the same fragment if the distance between their centroids is less than or equal to 4 fm [23]. At high bombarding energies, the NN collisions (with greater momentum transfer) nullify the correlations among the nucleons of the participant zone and only lighter fragments are produced from participant zone. At $\hat{b} = 0$ and 400 MeV/nucleon,

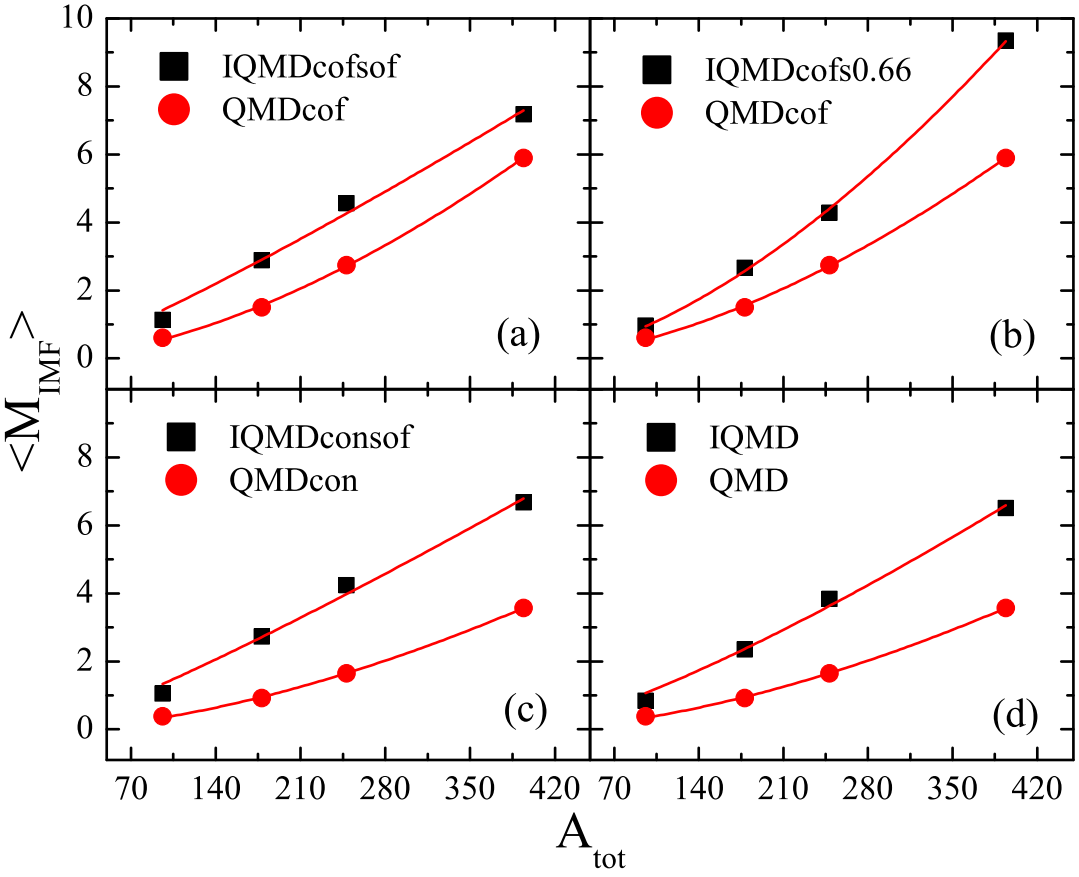

Figure 3.6: System mass dependence of $< M_{IMF} >$ for the same reactions as in Fig. 3.5. The symbols have same meaning as in Fig. 3.5.

there is a larger overlap between the impacting partners and the excitation in the system does not permit the construction of very heavy fragments (A$\geq A_{tot/6}$), hence we observe less number of IMFs. It has been already discussed in [246] about the universality of the power law behaviour for system size effect in multifragmentation. It becomes clear from Fig. 3.6, that the estimations of parameters c and τ rely on the size of fragment, on beam energy and colliding geometry of the reaction as mentioned in [246]. It is interesting here to note that both the models are successful in explaining the universal behaviour of power law in multifragmentation for system size effect. If we compare panel (d) with the panel (a) in Fig. 3.6, the absence of Coulomb and Symmetry potential from both the models in panel (a) bring the results too closer. The difference in the IMFs yield of both the models in panel (d) indicates the different treatment of Coulomb and symmetry potentials. As already mentioned in introduction, the Coulomb potential is isospin dependent in

IQMD model whereas in QMD model it is isospin independent (i.e. charge is averaged). Moreover, symmetry potential is only present in IQMD model and absent in QMD model. It is clear from the panel (d) that the difference is largest at higher system mass. More number of IMFs are produced with IQMD model calculations because number of collisions are less (see Fig. 3.4) in comparison to QMD model, so destruction of correlations among the nucleons is less leading to the formation of heavier mass fragments. In IQMD model the dependence of Gaussian width on system size affects the dynamics and the collision number changes in comparison to QMD model as explained in Fig. 3.4. The generation of LMFs and IMFs is more and that of FNs is less in case of IQMD model when compared to QMD model. This is because, as the number of collisions increases the production of FNs also increases. We have performed simulations for entire colliding geometry and incident energy range for both the models and establish that the results obtained are identical. Thus, an important insight into multifragmentation process is provided by these models and similar other dynamical models. However, it needs to be mentioned here that IQMD model reproduces the measurements of multifragmentation [247, 248], transverse flow [249–251] and nuclear stopping [41, 176] more accurately as compared to QMD model.

.

3.2.7 The composite particle yield ratios, X/p as a function of participant proton multiplicity N_p

After evaluating the part of model input parameters, one needs to compare the outcomes with the experimental information. In Fig. 3.7, author demonstrates the composite particle yield ratios (X/p; X implies A = 4 and p implies number of protons) against multiplicity of participant protons viz. N_p for the reaction $^{197}_{79}Au + ^{197}_{79}Au$. The composite particle yield ratio is $\frac{X}{p} = \frac{Y(A=4)}{p}$ where Y (A = 4) is the number of fragments having mass '4' in one event and p denotes the number of protons such that $p = \frac{Z_P+Z_T}{A_P+A_T}$ $[Y(A = 1)]$ where $A_P + A_T$ and $Z_P + Z_T$ is the total mass and charge of the colliding system.

The square and circle symbols represent calculations from IQMD and QMD respectively. The phase space has been created by both the models and the mechanism of clusterization is done by MST Algorithm. The Z value for the fragments/clusters is not fixed and is similar to what has been done in Ref. [252]. From the figure, author com-

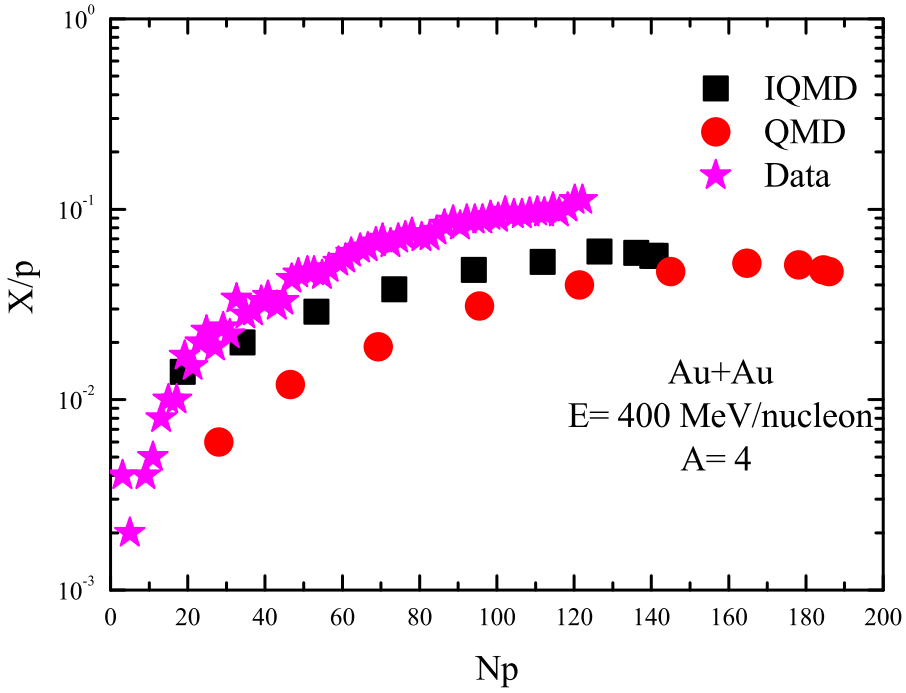

Figure 3.7: The composite particle yield ratios, X/p where X stands for A = 4 as a function of participant proton multiplicity N_p for reaction Au + Au. The star symbols represent the experimental normalized ^4He/p ratios [253].

prehends that X/p ratio increments with N_p or declines with the increase in colliding geometry. The X/p ratio increments distinctly with N_p for semicentral and peripheral impact parameters and achieves asymptotic value for greater estimations of N_p, specifically, for collisions at central geometry. It can be seen that calculations done by the author are in concurrence with the experimental information [252, 253]. Here the participant proton multiplicity in QMD has been calculated by taking average of the total particles participating in the reaction. The overall comparison of the two models indicates that the IQMD model possess all the essential ingredients required for the description of true dynamics behind a nuclear reaction and is therefore closer to the experimental data. Here we have not concentrated on isotopic composition of A=4. The comparison shows that IQMD model is better than QMD model to explain experimental data.

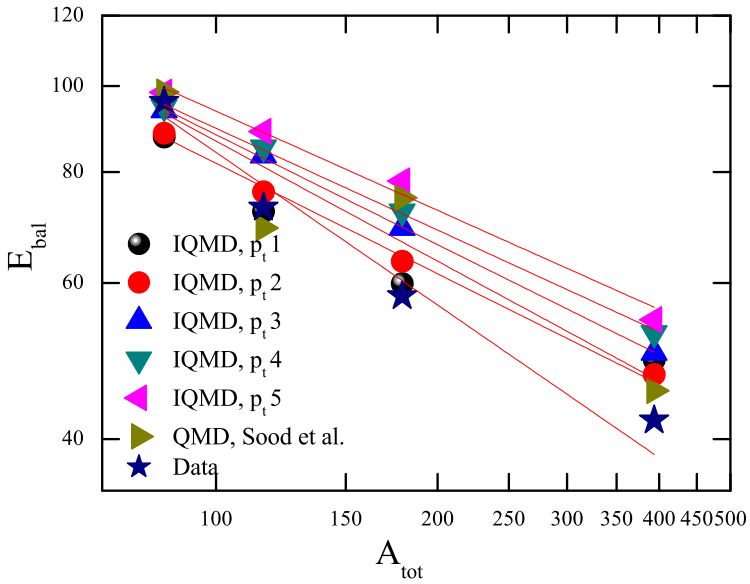

Figure 3.8: Balance energy as a function of combined mass of the system. The experimental points are displayed by solid stars whereas theoretical calculations for both IQMD (for different p_t ranges) and QMD are shown. The lines are the power law $\propto cA^{\tau}$

.

3.2.8 Balance energy as a function of total system mass

As discussed in Chapter 1, the interactions among the colliding nucleons balance at certain energy known as balance energy. In Fig. 3.8, author demonstrates the balance energy (E_{bal}) [71] against combined mass of the system extending from ${}^{40}_{18}Ar + {}^{45}_{21}Sc$ to ${}^{197}_{79}Au + {}^{197}_{79}Au$. For nuclei of lighter and medium mass, E_{bal} rises because of the reciprocation between nucleon scattering and mean field. Nonetheless, for heavier systems, Coulomb interactions are an indispensable ingredient. The Coulomb forces are significantly more grounded in heavier nuclei in comparison to lighter ones thereby causing an an early onset of flow in the former. Besides, a higher collision rate in heavier nuclei additionally contributes towards the early commencement of the flow. The variation in the outcomes of both the models is due to the difference in various input ingredients such as initialization, density distribution, width of the Gaussians, difference in the parameterization of potentials etc. [80, 254]. Till now no study has been reported on the dependence of balance energy with transverse momentum range of nucleons. Here we display the theoretical balance energies

using both IQMD and QMD. The values have been calculated using IQMD model for different transverse momentum ranges:

1. p_t1 = 0 to 0.2 GeV/c
2. p_t2 = 0.2 to 0.4 GeV/c
3. p_t3 = 0.4 to 0.6 GeV/c
4. p_t4 = 0.6 to 0.8 GeV/c
5. p_t5 = 0.8 to 1.0 GeV/c

It can be concluded from the figure that balance energy of nucleons in p_t1 and p_t2 range agree well with the data [255–259]. Therefore, we suggest that the experimentalists should use detectors for these two momentum ranges then they can get more reliable and accurate data.

It should be noted here that, we took mostly fragmentation as one of the observable to describe the theoretical comparison of the two transport models because it is not viable to include all phenomena. Here we are not discussing the microstructure of the fragments by using the two models because in QMD model the identity of nucleons is not known. The differences in the observables are mainly due to technical differences like the coding of the Pauli blocking and symmetry potential that does not exist in the QMD because neutrons and protons are not distinguished. The IQMD is suitable for a study of effects of the symmetry energy in reactions as it includes isospin effects. The parameterizations in IQMD model suffice the need for a correct explanation of isotopic effects in reaction dynamics at intermediate energy as compared to QMD model.

3.3 Summary

Now to summarize, we have analyzed the effect of initialization parameters on multifragmentation and flow by using the two dynamical transport models (QMD and IQMD). We examined the initialization parameters i.e. physics as well as technical parameters. Neither flow nor multifragmentation as a function of the strength of DDSE has been presented here. Isotopic effects on fragmentation have been studied in the past and have

found weak dependence of DDSE. The balance energy has been found to be sensitive to DDSE in the past investigations but here the focus was more on comparison of the models in order to study isospin effects via symmetry energy. Our study concludes that if one has to study isospin effects on the various observables associated with heavy ion collisions, the better candidate would be IQMD model.

Chapter 4

Effect of symmetry energy on fragment production

4.1 Introduction

The fact that the HICs ($A \geq 4$) in the intermediate energy regime (50 MeV/nucleon $<$ $E < 1000$ MeV/nucleon) are a suitable candidate to comprehend the isospin-dependent part of the nuclear EOS [8, 244, 260] has been well established till now. It is however, believed that the output of intermediate energy HICs (fragment production, nuclear flow and particle production) is susceptible to the DDSE. In order to pin down the dynamics associated with HICs and to understand the critical astronomical phenomena the proper constraining of DDSE is essential [157,261–266]. The behavior of nuclear matter at different densities can also be helpful to understand the different phenomena such as big-bang explosions, formation of universe and supernova explosions etc.. It is worth mentioning here that the mutual interactions of baryons inside the colliding system and neutron stars can be more efficiently predicted if the accurate information regarding symmetry energy (density dependent) is available. The present study is focussed on the investigation of the direct influence of DDSE on fragment production subjected to various mass-asymmetric combinations of target and projectile in nuclear reactions. The symmetry energy is given by $E_{\rm symm}(\rho) = E_{\rm symm}(\rho_o)\ \left(\frac{\rho}{\rho_o}\right)^{\gamma}$, where value of γ (stiffness factor) justify the strength of the symmetry energy at densities above and normal nuclear matter density, ρ_0 . The idea is to interpret the behavior of density dependent symmetry energy at different densities particularly low densities ($\rho \leq \rho_0, \rho_0 = 0.16$ fm^{-3}). The simulations have been carried out for various symmetric/asymmetric heavy-ion reactions at different colliding geometries for different symmetry energy strengths corresponding to γ = 0.5, 0.66, 0.9, 1.33, 1.5. In

other words, author has made effort to study the role of DDSE in reaction dynamics (via fragmentation) for one particular set of mass-asymmetric reactions (N/Z and total mass of colliding nuclei is fixed).

It is worth specifying that the DDSE is found to play a different role in the dynamics of the mass asymmetric reactions compared to symmetric reactions [267]. Previous investigations using molecular dynamical approach, had indicated the correlation between multifragmentation and reaction conditions (model ingredients) in symmetric and asymmetric HICs [47, 268]. Some fair predictions regarding the symmetry energy behavior at low-density are available in literature also [269–271]. The investigations for the symmetry energy behavior at high-density were far away to provide an appropriate and much acceptable form till recent years. Of late some predictions of the transport models wherein neutron and proton elliptic flows have been studied throw some light on the sensitivity of these observables to DDSE at supra saturation densities [272–274]. Due to mass asymmetry of the reaction, the participant zone will change that will lead to different values of densities. The aim for the present analysis [275] is to identify the influence of DDSE in multi-fragmentation (especially in the region of low-density) for different mass-asymmetric HICs.

It is expected that density achieved in mass asymmetric reactions is different, therefore role of different strengths of DDSE can be seen in fragment production. Production of light and heavy mass fragments can be correlated with stellar nucleosynthesis. So far any study regarding exploration of DDSE via multifragmentation particularly regarding the asymmetric target/projectile collisions is not available in the literature. Comparison with the experimental data is also shown.

4.2 Results and Discussion

In this investigation, author has simulated ${}^{80}_{36}Kr + {}^{80}_{36}Kr$ ($\tau = 0$), ${}^{72}_{30}Zn + {}^{88}_{40}Zr$ ($\tau = 0.1$), ${}^{54}_{26}Fe + {}^{106}_{48}Cd$ ($\tau = 0.3$), ${}^{40}_{20}Ca + {}^{120}_{52}Te$ ($\tau = 0.5$), ${}^{24}_{13}Al + {}^{136}_{57}La$ ($\tau = 0.7$) reactions having different mass asymmetries with mass-asymmetry factor $\tau \left(= \frac{A_T - A_P}{A_T + A_P}\right)$. Here, A_T and A_P represent the mass of target and projectile. The isotopic asymmetries ($\delta_A = (N - Z)/A$), of the chosen systems are of the order of 0.1. Therefore the influence due to isospin content of the colliding partners cannot be seen. The present work focuses on the varying mass and

not isospin content of colliding partners. The idea is to pin down the comparative role of DDSE in mass symmetric and mass-asymmetric reactions thereby exploiting the density of the combined system when compressed matter is formed. Author optimized various forms of symmetry energy (density dependent) in different mass-asymmetric reactions (but with same system mass and nearly same N/Z content varying between 0.08 to 0.13). The inclusion of momentum dependence of EOS is necessary to deduce the authentic reaction picture as the phenomenon of fragmentation (at peripheral impact parameters) is highly affected by it. Considering this very fact, author performed the present analysis with SMD EOS as described in Chapter 2.

4.2.1 Time evolution of mean numbers of FNs, LMFs and IMFs.

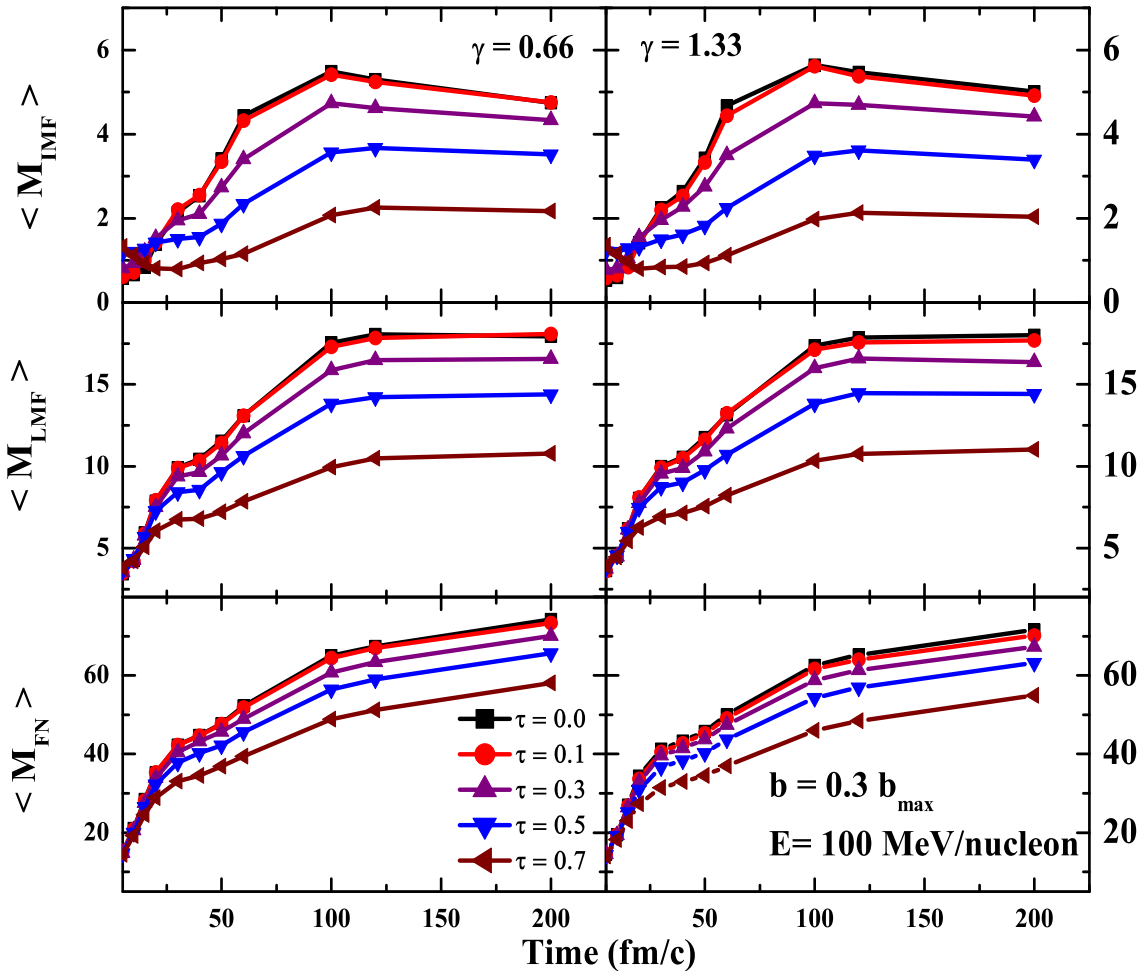

Figure 4.1: Time evolution of the mean number of FNs, LMFs and IMFs for stiffness factor (0.66 and 1.33) at an incident energy 100 MeV/nucleon and scaled impact parameter, $\hat{b} = 0.3$.

In Fig. 4.1, author presents the time evolution for multiplicity of different fragments and FNs for different mass asymmetric reactions at E_{inc} = 100 MeV/nucleon for stiffness factor (0.66 and 1.33) using soft EOS. The average multiplicity for FNs (A=1) $< M_{FN} >$, for LMFs (2 $\leq$A$\leq$ 4) $< M_{LMF} >$ and for IMFs (5 $\leq$A$\leq A_{tot}/6$) $< M_{IMF} >$ are displayed. With the passage of time there is an enhancement in the multiplicity of FNs, LMFs and IMFs. The FNs continue to be emitted depicting the cooling down of hot fragments. The LMFs also depict the well known trend of rise in their multiplicity, whereas IMFs depict a rise and a slight fall with the passage of time. It is evident from the figure that nuclear matter due to highly mass asymmetric collisions saturates slowly compared to mass symmetric collisions. This is because the participant zone decreases with the increase in mass asymmetry and therefore it takes longer time for nuclear matter to equilibrate. As evident from the figure, there is a minor effect of stiffness factor,γ on the multiplicity of FNs ($< M_{FN} >$), LMFs ($< M_{LMF} >$) and IMFs ($< M_{IMF} >$) and this has been proved in earlier studies as well [276,277]. It ought to be noted here that the yields of different fragments gets saturated and binary collisions terminate at the saturation phase. The onset of multi fragmentation, which may be identified to the nuclear liquid-gas phase transition, relies upon the incompressibility of nuclear matter also.

4.2.2 Excitation energy dependence of mean numbers of FNs and $A_{\max}$

In Fig. 4.2, the mean number of FNs ($< M_{FN} >$) and largest mass fragment, $< A_{\max} >$ are depicted against the excitation energy subjected to various strengths of DDSE. Based on the calculation of our recent communication [267] that the DDSE plays a different role in mass asymmetric reactions, author has performed the present study for a symmetric (τ = 0) and an extreme mass-asymmetric (τ = 0.7) nuclear reaction. Here, the total mass (A) and N/Z ratio (isospin content) is same in both the reacting systems. From the figure, it is evident that the multiplicity of FNs increase with the incident energy. At central impact parameters, almost all the nucleons take part in the collision, and simultaneously the number of binary collisions increase with an increase in the energy of the projectile. Also with an increase in incident energy the effect of Pauli blocking tends to decrease and the correlations among the nucleons are destroyed which prompts the production of more number of FNs. Also the role of the strength of DDSE on the

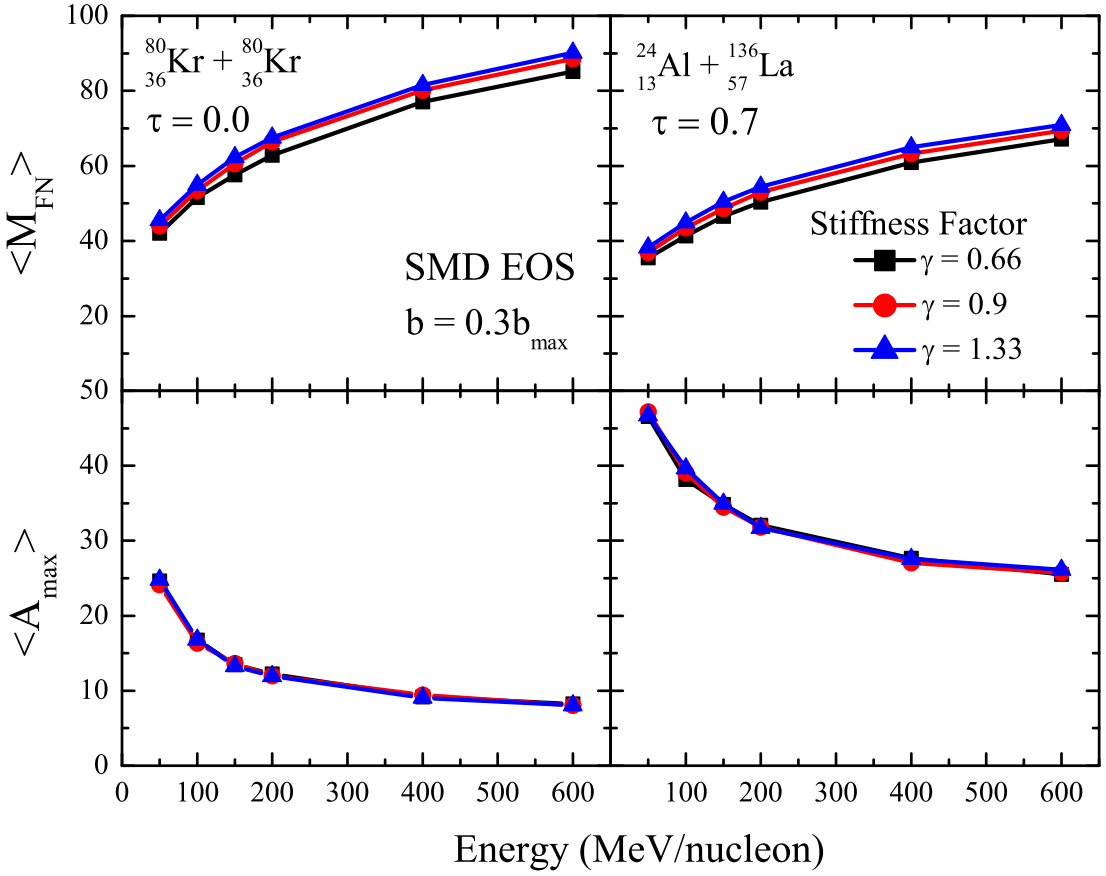

Figure 4.2: The excitation energy dependence of mean number of free nucleons (upper panel) and $< A_{max} >$ (lower panel) for the system $^{80}_{36}$Kr + $^{80}_{36}$Kr and $^{24}_{13}$Al + $^{24}_{13}$Al at the colliding impact parameter of $b = 0.3b_{max}$.

multiplicity of FNs is visible for both mass symmetric and mass asymmetric reactions. Recent investigation showed that considering π^+/π^- ratio at minimal incident energies, the role of NN cross section is more than symmetry energy [278]. Although, neutron-rich and neutron-poor isotopes with same system mass completely nullifies the effects of NN in-medium cross section [278].

The emission of FNs at this energy is assumed to be similar to the vaporization of nuclear matter [44, 279]. The largest composite mass $< A_{\rm max} >$ tends to decrease due to dissociation into much smaller masses as the incident energy increases. Because of more compression at higher energies, the collision of symmetric nuclei drives matter into participant zone (where a nucleon suffers at least one binary collision) and, as a result, the size of $< A_{\rm max} >$ becomes small at the final stage of the reaction. In case of mass

asymmetric reactions, the overlapping of projectile and target is incomplete due to which the participant zone is small and the spectator zone (where a nucleon does not suffer any collision) is larger leading to the formation of a bigger composite mass with an increase in incident energy. The mass-asymmetric reactions give rise to a comparatively minor thermalization of the nuclear matter [64, 66, 177, 245].

4.2.3 Influence of strength of symmetry energy on fragmentation

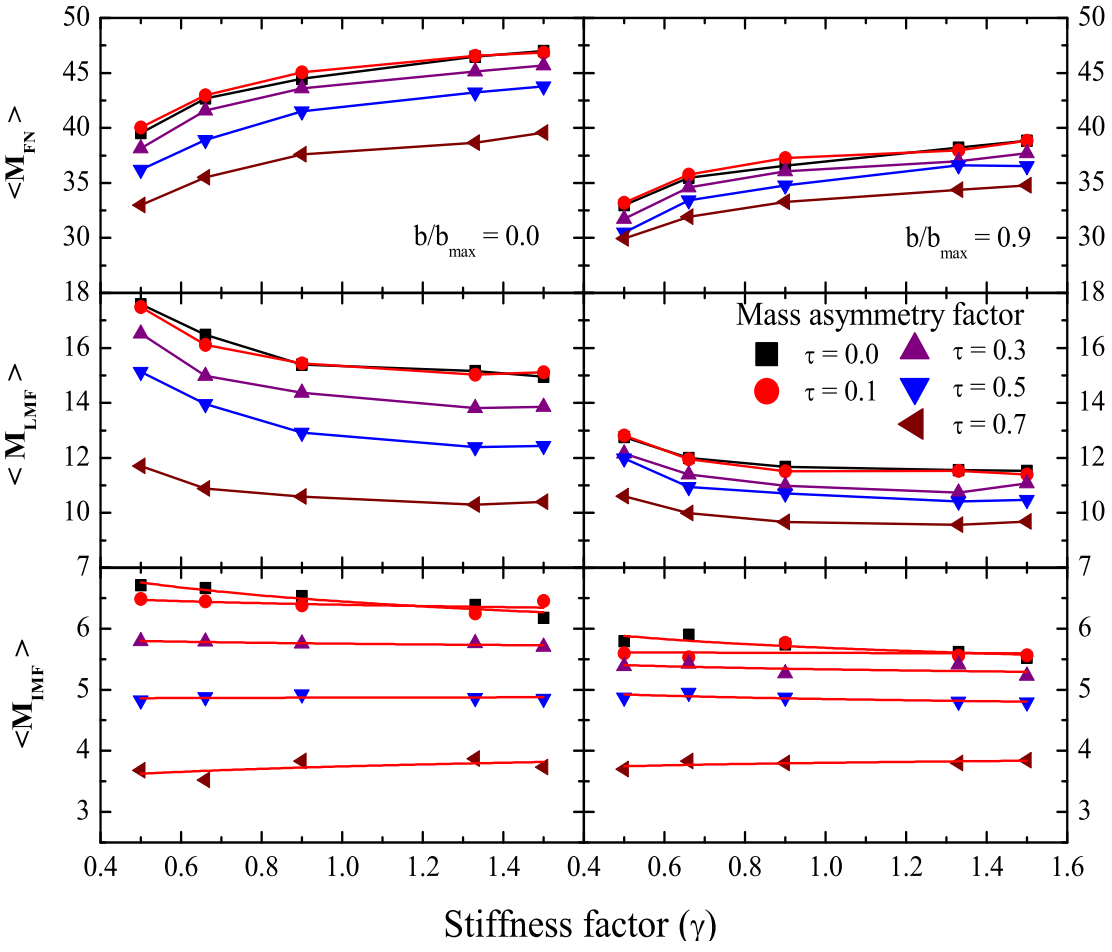

Figure 4.3: Dependence of fragment production on stiffness factor, γ.

The impact of DDSE on fragmentation and reaction dynamics for symmetric intermediate energy heavy-ion collisions based on molecular dynamical approach has shown encouraging results. In the present chapter [275] , we attempt to make much more in-depth analysis for the DDSE with reference to fragment production in mass-asymmetric target-

projectile reactions. In Fig. 4.3, we display the mean multiplicity for FNs ($< M_{FN} >$), LMFs ($< M_{LMF} >$) and IMFs ($< M_{IMF} >$) as a function of stiffness factor, gamma (γ) at central (left panel) and peripheral colliding geometries (right panel) at $E = 50$ MeV/nucleon. For all the forms of DDSE, the mean IMFs multiplicities $< M_{IMF} >$ scale with respect to mass asymmetry of the colliding pairs when the system mass is constant. Lowest IMF yield is obtained for the extreme mass-asymmetric reactions ($\tau = 0.7$) for both the impact parameters (central and peripheral). At $E = 50$ MeV/nucleon, even for $b = 0.9\ b_{\rm max}$ i.e., at extreme peripheral collisions, where overlapping region is very less, high sensitivity of IMFs production towards mass asymmetry (τ) is observed. At both impact parameters, a negligible role of DDSE on IMFs production is observed for the different forms of DDSE. Recent detailed analysis on the IMFs production for symmetric reactions has also predicted a moderate dependence of IMFs multiplicities on stiffness factor [245]. Also, one cannot see any abrupt change in the IMFs yield for any particular colliding system (τ value). Also, the average production of LMFs is much more sensitive towards DDSE than the heavier fragments and FNs (protons and neutrons). This is due to the fact that IMFs being originated from the spectator zone does not experience much variation in density. However, FNs are emitted from the central collision zone where the violent interactions demonstrate the effect of DDSE.

LMFs originate from the participant zone, and also some contribution from the spectator zone. It can be concluded that the heavier fragments such as IMFs cannot give any direct or concrete information regarding the strength of DDSE. Also, from the heavier fragments it is hard to verify the fact that whether the DDSE plays any dissimilar role in reactions having different mass asymmetries. Therefore, one should look for the yield of smaller fragments instead of heavier fragments to interpret the DDSE behavior at sub-supra saturation densities.

4.2.4 Neutron-to-proton $<N/P>$ ratio as a function of stiffness factor, γ.

One must understand the fact that emission of smaller fragments from participant zone is more sensitive to the stiffness factor of DDSE. In Fig. 4.4, we display the mean neutron-to-proton $<N/P>$ ratio for various colliding pairs vs stiffness factor γ. The different γ values justify the magnitude of DDSE in the region of low-density which can affect the

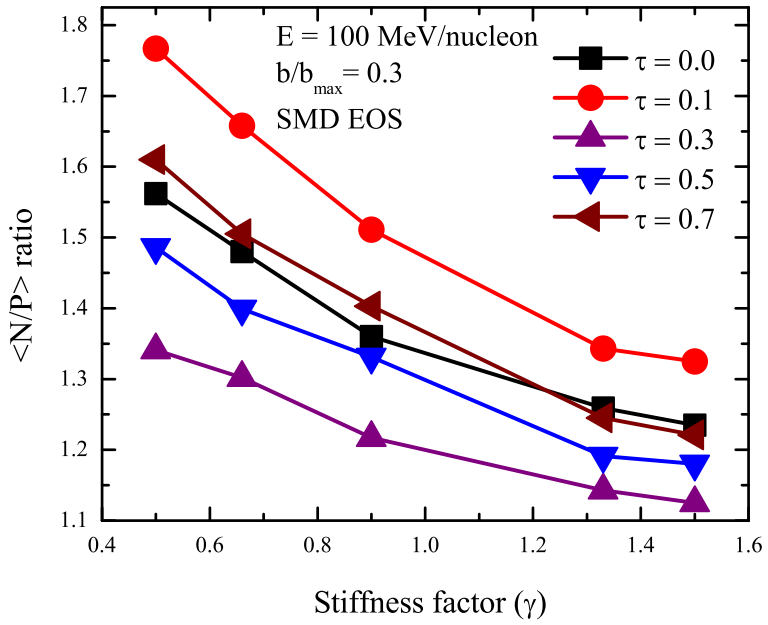

Figure 4.4: Neutron/Proton ($<N/P>$) ratio as a function of stiffness factor γ for different colliding pairs at an incident energy of 100 MeV/nucleon.

fragment production. It is evident that the large mass asymmetric reactions leads to lesser average density/temperature reached during the overlapping phase. At E = 100 MeV/nucleon the variation in the $<N/P>$ ratio with respect to γ is very high for all τ values. The $<N/P>$ ratio decreases for more stiff dependence of symmetry energy. The similar trend is observed for the different mass-asymmetric target-projectile colliding pairs. The Coulomb interaction induces repulsion between the protons. At the same time, the symmetry energy tends to induce the repulsion between the neutrons. Even for the extreme mass-asymmetric nuclear reactions the visible change in the neutron emission is observed. The neutron/proton ratio first increases and then decreases as we go towards higher mass asymmetry of the reactions. This is due to the insufficient overlap of projectile and target for higher mass asymmetries. There is no regular trend for neutron/proton ratio because of the difference in the compression achieved in the participant(compressed) zone of the colliding nuclei. The different strengths of DDSE is due to densities away from normal nuclear matter density. In case of stiff dependence, DDSE tends to increase at supra-densities ($\rho > \rho_o$) and in case of soft dependence, it decreases above the normal nuclear matter density [244, 280]. This dependence of the neutron/proton emission on

symmetry energy does not show any regular trend for the different values of stiffness factor because variation of density incase of the above mass asymmetric combinations does not show a regular trend. The symmetry energy is inversely monotonic above and below the saturation density. Hence, the neutron emission resulting from the compressed participant zone does not follow a regular pattern so does the neutron/proton ratio. However, the multiplicity of light fragments and the observables associated with the participant zone (such as $<N/P>$ ratio) are sensitive towards DDSE for all τ values.

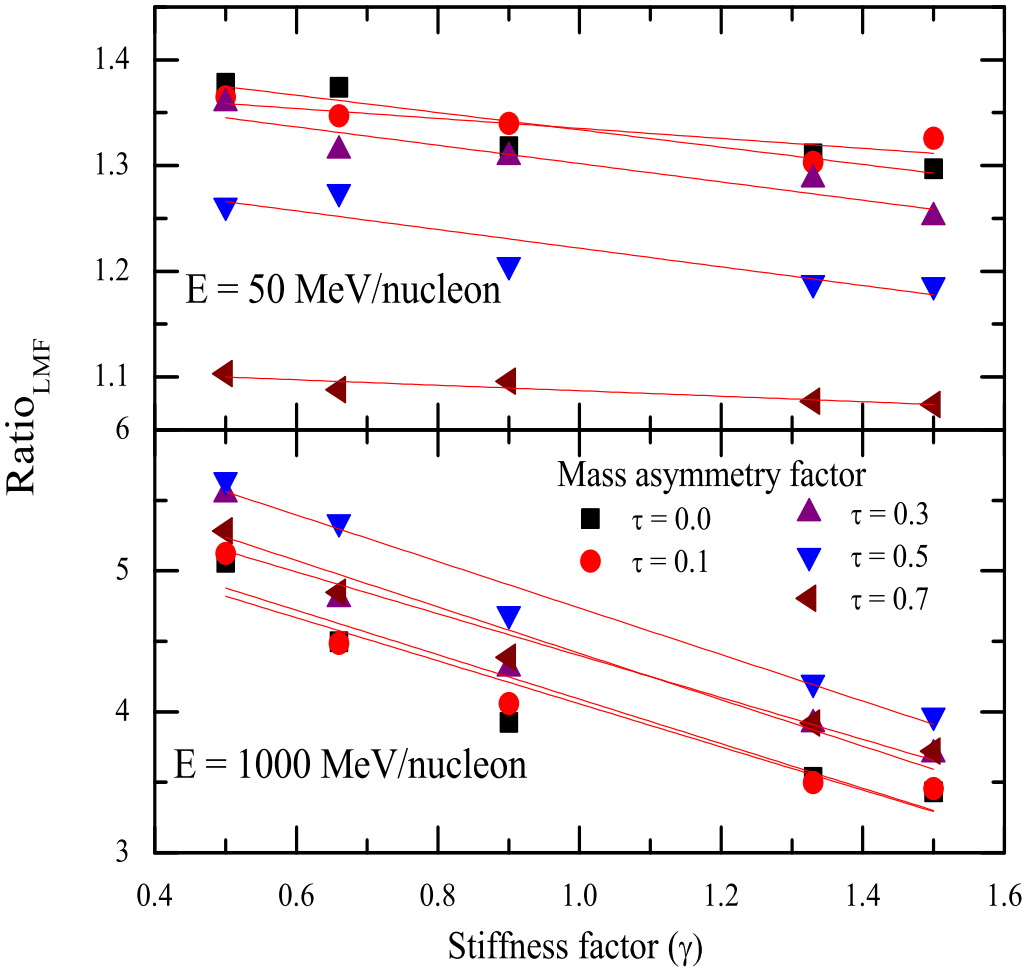

Figure 4.5: Ratio $(\frac{<M_{LMF}>(\hat{b}=0)}{<M_{LMF}>(\hat{b}=0.9)})$ of LMF multiplicity for central impact parameter $b = 0.0b_{max}$ and peripheral impact parameter $b = 0.9b_{max}$ at incident energy E = 50 MeV/nucleon (upper panel) and E = 1000 MeV/nucleon (lower panel).

In Fig. 4.5 we display the ratio of LMFs multiplicity $(\frac{<M_{LMF}>(\hat{b}=0)}{<M_{LMF}>(\hat{b}=0.9)})$ at central impact parameter $b = 0.0b_{max}$ and peripheral impact parameter $b = 0.9b_{max}$ at beam energy E

= 50 MeV/nucleon (upper panel) and E = 1000 MeV/nucleon (lower panel). The LMFs multiplicity at central impact parameter is more than the multiplicity at peripheral impact parameter for both the energies. The slope of the ratio is negative for both the energies. This implies that at lower values of stiffness factor there is a huge difference between the multiplicity of light mass fragments at central geometry and at peripheral geometry. At higher values of stiffness factor this difference in the multiplicity gradually decreases. However the slope is more steep in case of 1000 MeV/nucleon than 50 MeV/nucleon. At higher energy, the matter is more excited and energy pumped in the participant zone is more. As a result, the matter will shatter leading to the emission of more LMFs incase of peripheral impact parameter in comparison to central impact parameter where evaporation is more. Moreover, the repulsive nature of symmetry energy is more at higher values of stiffness factor.

4.2.5 Z_{bound} dependence of mean multiplicity of IMFs ($< M_{IMF} >$)

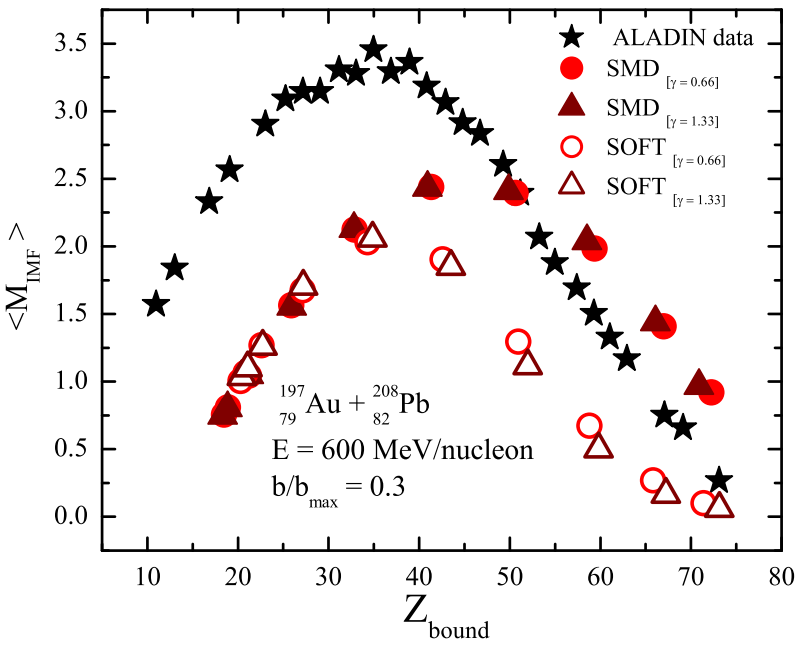

Figure 4.6: Z_{bound} dependence of mean intermediate mass fragment multiplicity ($< M_{IMF} >$) for $^{197}_{79}$Au + $^{208}_{82}$Pb at incident energy of 600 MeV/nucleon and comparison with data [44].

In Fig. 4.6, the mean multiplicity of IMFs is plotted as a function of $Z_{\rm bound}$ for the reaction $^{197}_{79}$Au + $^{208}_{82}$Pb at 600 MeV/nucleon and comparison with experimental data is indicated [44]. The quantity Z_{bound} is characterized as the sum of all atomic numbers (Z_i) of all fragments with $Z_i \geq 2$. Infact, it gives us a decent assurance of the colliding geometry. Z_{bound} gives the magnitude of violence of the collision and of the energy saved in the energized spectator. It is clearly evident from the figure that the mean IMFs multiplicity ($< M_{IMF} >$) observed with the ALADIN spectrometer first increases up to a maximum value of 3.5 at $Z_{\rm bound} \approx 40$ and then decreases up to $Z_{\rm bound} \approx 80$. In case of soft EOS, there is a shift in the value of maxima towards smaller values of $Z_{\rm bound}$ whereas in case of SMD EOS the maximum is at $Z_{\rm bound} \approx 45$ which is very close to the experimental data. Therefore, in case of mass asymmetric colliding system the role of DDSE in the estimation of IMFs production is not prominent and the production of heavier fragments is dependent more on the impact parameter of the concerned reaction and momentum dependence of the nuclear EOS. Undoubtedly, theoretical estimations with SMD EOS yield much better concurrence with experimental findings. The SMD EOS is suitable to justify the experimental data especially at peripheral collisions as also mentioned in [44, 281, 282].

Most of the nuclear matter in central collisions is contained in the participant zone and hence the energy transferred to the spectator matter is least. Using multifragmentation as a tool, the low-energy reactions are capable to provide much authentic picture of the DDSE as well as of the reaction outcome. In all, for all the symmetry energy forms, the values of fragment multiplicities calculated in the present study show a drastic variation with respect to mass asymmetry factor τ, but negligible with different strengths of symmetry energy.

4.2.6 Impact parameter dependence of $Z_{\rm max}$

In Fig. 4.7 we display the Z_{max} along the whole impact parameter range for SOFT as well as SMD EOS. The quantity Z_{max} is defined as the average charge of the largest fragment [44, 282]. It shows the similar behaviour as that of A_{max}. In the figure, the Z_{max} increments with impact parameter of the reaction. As the impact parameter is

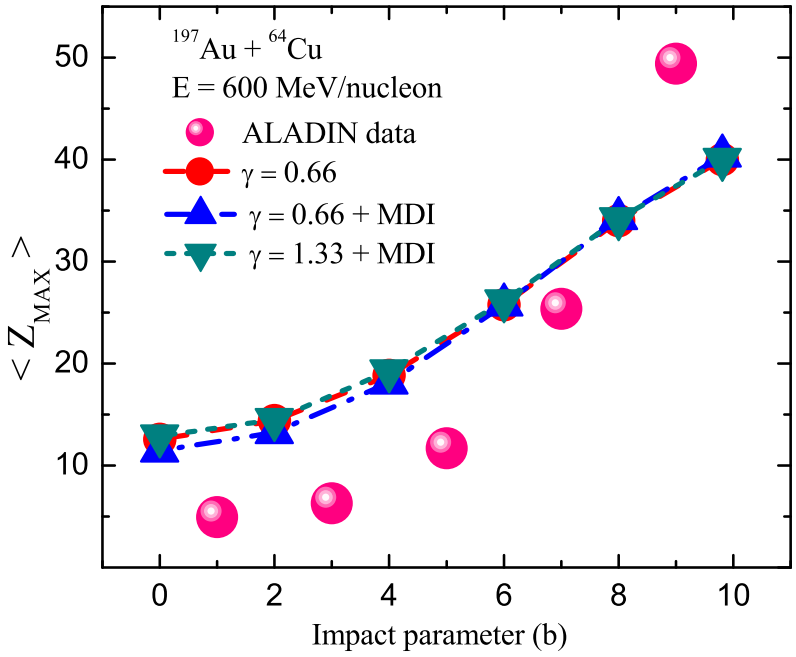

Figure 4.7: Z_{max} as a function of impact parameter at an incident energy of 600 MeV/nucleon and comparison with experimental data [44].

increased, participant region reduces and spectator region enhances prompting a further rise in the generation of heavier fragments and henceforth increase in the estimation of Z_{max}. The symmetric colliding nuclei respond more to the impact parameter reliance of Z_{max} when compared to the asymmetric colliding nuclei. This prompts the likelihood of IMFs generation even at central collisions. The change in the impact parameter does not modify excessively the creation of IMFs in mass asymmetric colliding nuclei compared to symmetric ones.

4.3 Summary

Study of different mass-asymmetric reactions, using different parameterizations of density-dependent symmetry energy is summarized as follows:

1. Intermediate mass fragment production is highly sensitive to the mass-asymmetry factor (τ) for both central and peripheral collisions.

2. One cannot rely on the yield of heavy fragments to interpret the strength of symmetry energy in case of extreme mass-asymmetric as well as symmetric HICs.

3. Analyzing multifragmentation at lower incident energies one can extract information regarding isospin dependence of nucleonic interactions. Yield of smaller fragments (like neutron/proton emission) can be much suitable to verify the behavior of symmetry energy even in extreme mass-asymmetric reactions. Free nucleons shows minor sensitivity to various density dependent strengths compared to heaviest fragment $< A_{\max} >$ which shows almost no sensitivity at $E = 50$ MeV/nucleon.

Chapter 5

Influence of symmetry energy on local and global nuclear stopping

5.1 Introduction

The principle inspirations of studying the HICs at intermediate energies is to gain indispensable information regarding the nuclear EOS. The predictions of the microscopic transport models when compared with experimental data streamline our comprehension of the fundamental ingredients of such models: in particular the in-medium properties of the NN interactions and nuclear EOS. The most debatable issue, in this framework is the thermalization of the system in strongly dissipative as well as weakly dissipative collisions in view of their correlation with liquid-gas phase transition. The key observable to consider the level of thermalization (equilibration) achieved in HICs is the nuclear stopping. The nuclear reactions offer fascinating isospin dependent situation where in-medium NN collisions, Coulomb potential and symmetry potential are all present at the same time. However, the influence of isospin dependent mean field potentials (including symmetry potential) on nuclear stopping has not been well determined so far for mass asymmetric reactions. On the one hand, the form and strength of DDSE especially at supra-saturation densities needs to be understood completely to unfold the thermodynamical properties of nuclear matter and on the contrary, it assumes a pivotal role in deciding the structure, configuration of neutron stars [8, 283–285] and various other astronomical phenomena (GDR, PDR, neutron skin thickness) [286–288]etc.. Symmetry energy can be expressed as a function of density; $E_{symm}(\rho) = E_{symm}(\rho_o)\ \left(\frac{\rho}{\rho_o}\right)^{\gamma}$ [49, 280, 289–292] where the value of γ legitimize the stiffness (or strength) of the symmetry energy at various densities. Various investigations have been accounted for on the role of DDSE and the extent of

thermalization reached in symmetric reactions in the past [172, 176]. Additionally investigations from the last few decades had concluded that nuclear stopping can be utilized as a probe to consider the dissemination phenomena with reference to energy and isospin transport by taking symmetry energy into account [119, 176]. Interestingly, there is no systematic study accessible in the literature on the influence of isospin effects by means of DDSE on stopping due to fragments from the participant zone over the whole energy range. Liu *et al.* [167] indicated that, nuclear stopping is profoundly affected by the isospin dependence of in medium NN cross section, considering the energy domain extending from Fermi energy to 150 MeV/nucleon, but remains unaffected by symmetry potential. However underneath Fermi energy, stopping is responsive to symmetry potential as well as in-medium NN cross section. Li and Li [168] contemplated the incident energy dependence of quadrupole moment (Q_{zz}/nucleon) and anisotropy ratio (R) on system size, neutron-proton ratio and the medium correction of two body NN cross sections. The results were however, insensitive towards the symmetry potential. Puri *et al.* [41] studied the relation between global nuclear stopping and fragment production without considering isospin of the system and concluded that there is a high correlation between light charge particles emission and global nuclear stopping. Later on Kumar *et al.* [232] performed the similar study by taking into account isospin of the system via DDSE and isospin dependent cross section. One of our coworkers [174] examined the impact of isospin dependence of NN cross-section on nuclear stopping for isobaric series and concluded that stopping relies emphatically on the cross section. Also, it has now been established that the degree of stopping is influenced by binary collisions and the in-medium impacts, for example, Fermi motion and Pauli blocking [119, 120]. The global nuclear stopping, $< R_E^{global} >$ prompts randomization of one body momentum space or momentum transfer amid the break down of initial correlations between the nucleons of target and projectile nuclei. The colliding partners compress each other along with heating of the matter [181]. At central collisions for mass symmetric systems, the initial correlations between nucleons breaks and hence global stopping takes place. The extent of $< R_E^{global} >$ depends on incident energy, the mass of colliding nuclei and impact parameter. We assume the asymmetry parameter $\tau \left(= \frac{A_T - A_P}{A_T + A_P} \right)$, as discussed in Chapter 4 [293]. Various mass asymmetric colliding systems (with fixed total system mass as well as constant N/Z ratio) are chosen in order

to bring forth an ideal analysis regarding the role of isospin (symmetry energy) at intermediate energies. Formulation of radioactive ion beam facilities in present times in numerous laboratories has additionally made it feasible to ponder the neutron or proton rich HICs. The present chapter [294] specifically highlights the role of DDSE on local $< R_E^{local} >$ (of light mass fragments ($A_f \leq 4$) obtained from the participant zone) and on global $< R_E^{global} >$ stopping for mass asymmetric reactions. The nucleons from the target and projectile which suffer at least one collision are considered to be a part of participant zone and those which do not suffer any collision are considered to be from spectator part. The experimental investigations and their comparison with theoretical predictions may lead to a much better picture and understanding of the results obtained via theoretical IQMD [80] model based calculations. To be precise, the present study aims at:
To investigate the influence of DDSE :
(i) on $< R_E^{global} >$ and $< R_E^{local} >$ in mass asymmetric nuclear reactions.
(ii) and interpretation of experimental data with theoretical results.

5.2 Results and discussion

Considering $\tau \left(= \frac{A_T - A_P}{A_T + A_P} \right)$ as the factor indicating mass asymmetry, we presented results for the intermediate energy collisions for the systems ${}^{80}_{36}Kr + {}^{80}_{36}Kr$ ($\tau = 0$), ${}^{72}_{30}Zn + {}^{88}_{40}Zr$ ($\tau = 0.1$), ${}^{54}_{26}Fe + {}^{106}_{48}Cd$ ($\tau = 0.3$), ${}^{40}_{20}Ca + {}^{120}_{52}Te$ ($\tau = 0.5$), ${}^{24}_{13}Al + {}^{136}_{57}La$ ($\tau = 0.7$), same total mass ($A_{TOT} = A_P + A_T = 160$) for an extensive range of beam energies and colliding geometries. Here, A_T and A_P are mass of the target and projectile. Most of the calculations have been performed $b = 0.3\ b_{max}$, where $b_{max} = 1.12(A_P^{1/3} + A_T^{1/3})$ fm.

The role of symmetry energy has been checked at densities far from $\rho_0 = 0.16\ fm^{-3}$, corresponding to stiffness parameters ($\gamma = 0.5$, 0.66 , 0.9, 1.33 and 1.5). Calculations for stopping parameter by using phase space of the nucleons/fragments have been performed at saturation time i.e. 200 fm/c. The $< R_E^{global} >$ can be defined as:

$$R_E^{global} = \frac{1}{2} \sum_i |E_t(i)| / \sum_i |E_l(i)| \tag{5.1}$$

where $E_t(i)$ and $E_l(i)$ give transverse and longitudinal energies for i^{th} particle in the center of mass frame. Here author has calculated the $< R_E^{local} >$ in the participant matter. The idea is to also analyze the influence of DDSE in the participating nuclear matter only via

light mass fragments with mass, ($A_f \leq 4$). Because the density reached in participant zone is more than normal nuclear matter density, therefore symmetry energy can act as probe for $< R_E^{local} >$. The stopping calculated using participant zone is denoted as $< R_E^{local} >$ whose mathematical form is same as equation 5.1.

5.2.1 Time evolution of global stopping

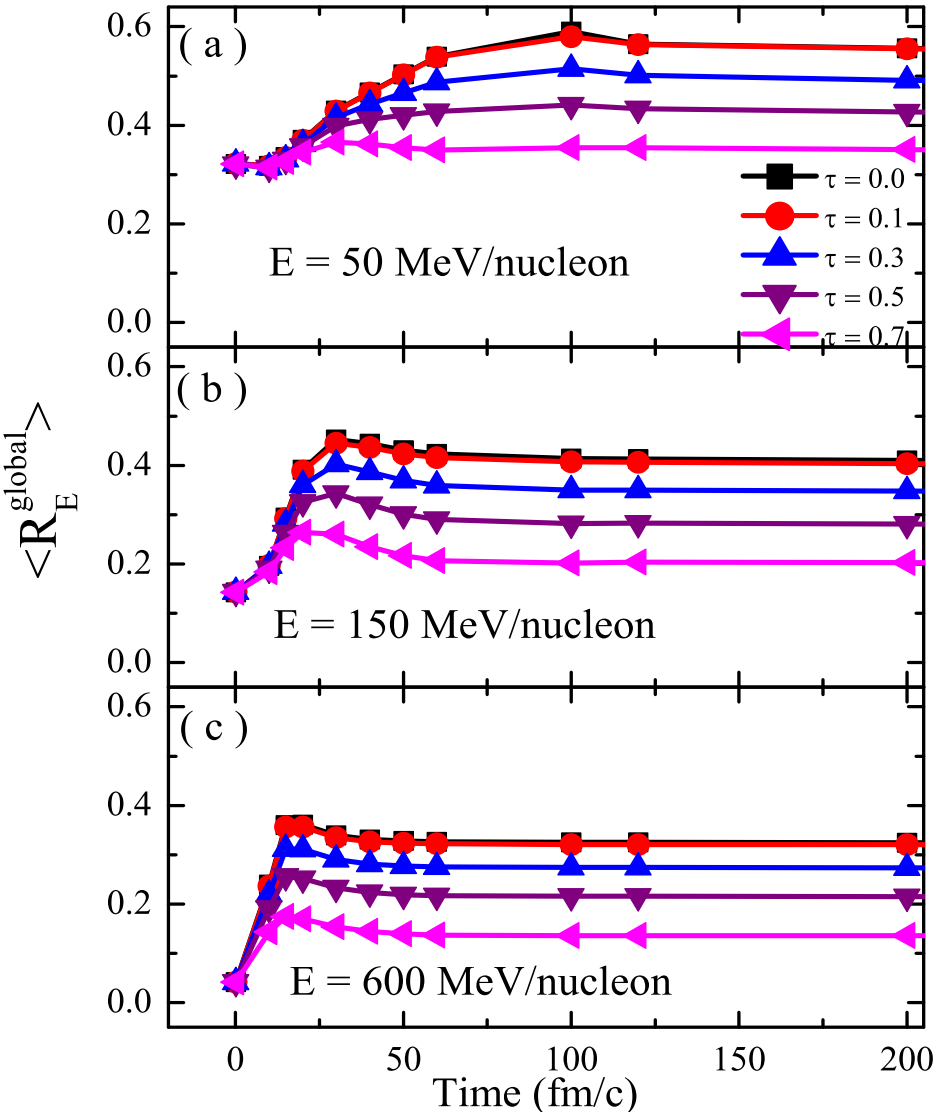

Figure 5.1: Time evolution of global stopping parameter ($< R_E^{global} >$) at incident energy of 50 MeV/nucleon, 150 MeV/nucleon and 600 MeV/nucleon and colliding geometry, $\hat{b} = 0.3$ for stiffness factor, $\gamma = 0.66$ for soft equation of state.

Fig. 5.1 (panel a, b and c), depicts the dynamics of both the types of reactions mass symmetric as well as mass asymmetric through $< R_E^{global} >$. As the reaction proceeds the

collision between the nucleons keep on decreasing. The rate of nucleons in which result in slight peak around 20-40 fm/c. The peak is missing at low energy due to the small number of collisions. But as energy increases the value of peak increases due to large number of collisions. But further increase in energy leads to transparency and hence decrease in peak value around 20-40 fm/c. One can see that maximum value of $< R_E^{global} >$ is obtained for $\tau = 0$. This is due to maximum overlap of target and projectile nuclei. Also the time at which $< R_E^{global} >$ saturates is maximum for $\tau = 0.7$.

Due to incomplete compression, the nuclear matter takes longer time to equilibrate. With the increase in mass asymmetry, the participant zone decreases as a result of which $< R_E^{global} >$ decreases. Also, the value of stopping is maximum at low energy (panel (a)) and then decreases (panel (b) and panel (c)). The dynamics at low energy, is administered by mean field since Pauli blocking suppresses the collisions among nucleons. With the increase in energy, NN collisions increase and the nucleons drift in the transverse direction which leads to more stopping. In mass asymmetric reactions, the lesser overlapping of target and projectile leads to a nonuniform distribution of nuclear matter after the collision phase. The $< R_E^{global} >$ for the reactions under consideration depends directly on the relative size of target and projectile. The value of nuclear stopping $< R_E^{global} >$ saturates after the participant and spectator matter hardly make an impact on each other and the interactions among the nucleons are negligible.

5.2.2 Density profiles of participant and spectator matter

The thermodynamical properties of the system can be measured using density, temperature and pressure. Fig. 5.2, show the density profiles [229, 295] of the participant matter (where nucleons suffer at least one collision) in panels (a and b) and spectator matter (nucleons with no collisions) in panels (c and d) for both symmetric $^{80}Kr +^{80} Kr$ ($\tau = 0$) and mass asymmetric $^{24}Al +^{136} La$ ($\tau = 0.7$) reactions using the equation

$$\rho_i(r,t) = \sum_i^{A_{tot}} \frac{1}{(2\pi L)^{3/2}} e^{-[\mathbf{r}-\mathbf{r_i}(t)]^2/2L}. \tag{5.2}$$

Here $r_i(t)$ defines the centroid of i^{th} particle in coordinate space and $A_{tot}= A_P + A_T$. The z axis is taken as beam direction and the density profiles have been plotted in three dimensional coordinate space. The very first collisions rapidly build up the participant

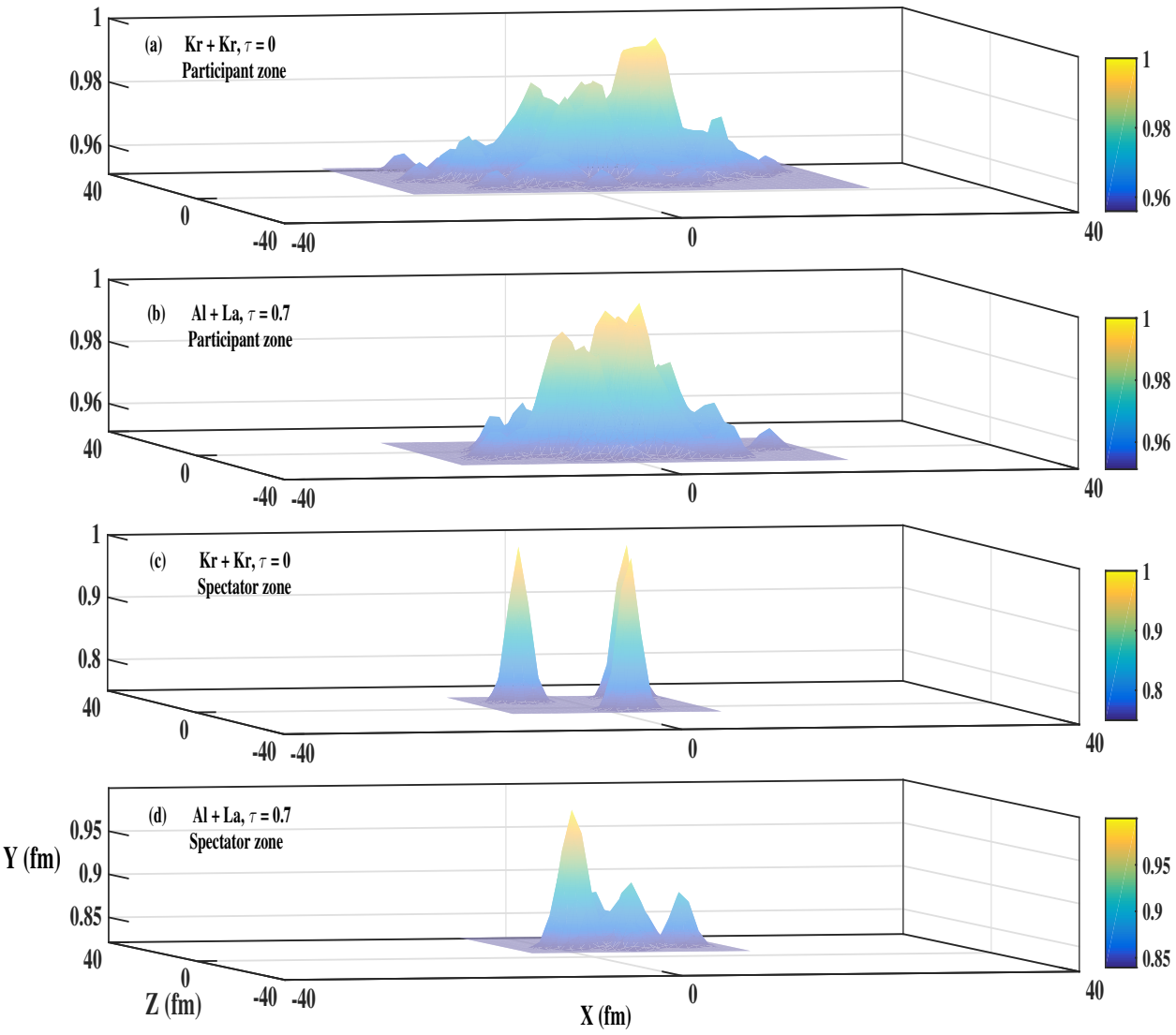

Figure 5.2: Density profiles of the participant and spectator matter at time $t = 40fm/c$. The plots are at $\hat{b} = 0$ and incident energy 400 MeV/nucleon for stiffness factor, $\gamma = 0.66$ for soft equation of state for a single event. The yellow portion at the centre correspond to highest density.

zone upto t = 40 fm/c. These participant nucleons act as an interface between target and projectile and there is no longer any direct interaction between spectator of target and projectile. There is a significant difference between the participant as well spectator zone of symmetric reaction when compared to mass asymmetric reaction. In symmetric reaction $^{80}Kr+^{80}Kr$ ($\tau = 0$) the participant zone is more dense than asymmetric reaction $^{24}Al+^{136}La$ ($\tau = 0.7$). The remnants of spectator for symmetric reaction do not survive for a longer time (at t = 40 fm/c) in comparison to asymmetric reaction for the same time. Also the bombardment of projectile on target in case of asymmetric reaction leads

to some amount of destruction of the projectile as can be seen for the present energy (E = 400 MeV/nucleon) at central collisions ($b = 0\ b_{max}$). Therefore, thermalization achieved is more incase of mass symmetric reaction. The nucleons from the participant zone are sufficient to provide significant information regarding EOS because here the distortion of the information due to spectators is less. One more interesting thing to note here is the rotational behaviour of the nuclear matter incase of mass asymmetric colliding system. The phenomenon of rotation of projectile and target is easily observed at semi central and peripheral collisions and has been reported by one of our collaborators in Ref. [296]. Moreover, for mass asymmetric colliding system participant zone and spectator zone can be differentiated using rapidity dependence of the nucleons falling in specific rapidity bins based on the mass asymmetry and the same observation can be verified by experimentalists.

5.2.3 Mass asymmetry dependence of density and allowed collisions

Fig. 5.3, show the maximum value of density normalized with normal nuclear matter density,ρ_o (upper panel) and allowed collisions (lower panel) for all mass asymmetries. The peak values show variation with respect to mass asymmetry due to the variation in the overlapping zone.

Additionally, the larger incident energy relates to more pressure and in this way brings about a rise in the maximum value of density. The peak value of allowed collisions follow the similar trend as that of density. The peak value of NN collisions signifies a phase having high density in the reaction. As the mass asymmetry increases, the peak value of allowed collisions decreases due to less availability of collisions.

5.2.4 Dependence of global and local nuclear stopping on incident energy

The $< R_E^{global} >$ as well as $< R_E^{local} >$ (of light mass fragments ($A_f \leq 4$) obtained from the participant zone) are significantly influenced by incident energy. At low energy, because of Pauli blocking the NN collisions are subdued which leads to more stopping. The scenario is quite different at higher energies, where two body NN collisions perform a dominant role. At higher energies, fragment phase space becomes similar to the nucleon phase

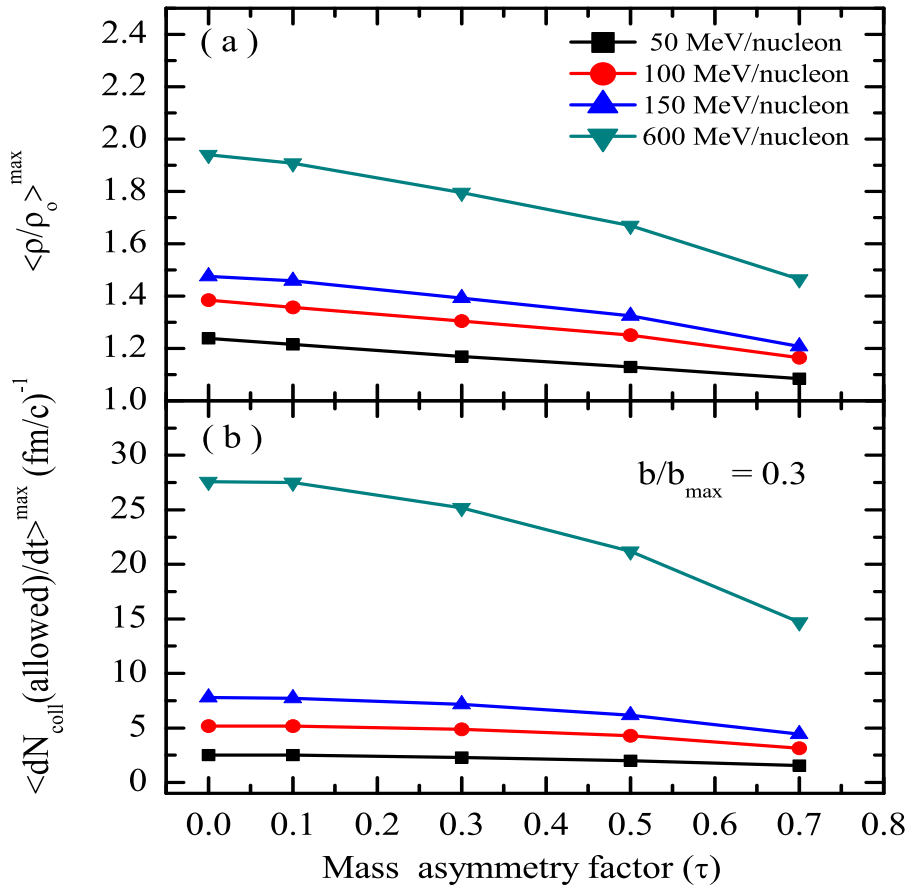

Figure 5.3: Mass asymmetry dependence of maximum value of density and allowed collisions for stiffness factor, $\gamma = 0.66$.

space [164]. Fermi motion plays a dominant role at higher energies, therefore it has been suggested that at intermediate energies, one should calculate the stopping using fragment phase space.

For studying the influence of incident energy on nuclear stopping due to mass asymmetry and DDSE, we have opted for $< R_E^{global} >$ and $< R_E^{local} >$. Fig. 5.4(a), represent $< R_E^{global} >$ plotted against incident energy. One can see that there is more stopping in participant zone ($< R_E^{local} >$), but still full stopping is not achieved. One can see a decrease in stopping with an increase in energy for a given mass asymmetry. As the mass asymmetry increases, stopping further decreases at a given energy. Minimum stopping is observed for highest mass asymmetric nuclear reactions. Since the collisions have been performed at scaled impact parameter $\hat{b} = 0.3$, there would be a possibility of dissipation of energy through the rotational effect of nuclear matter. The number of nucleons

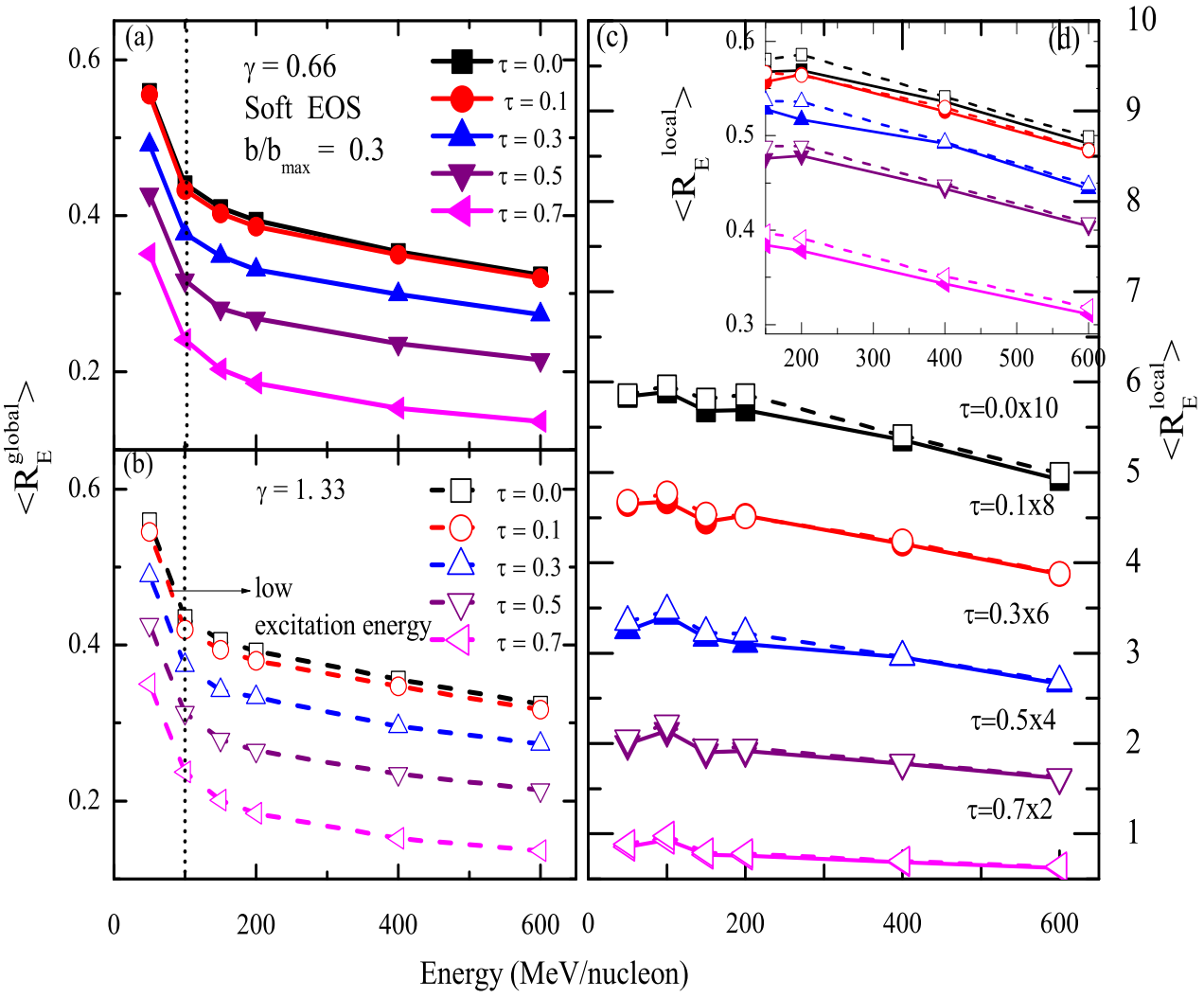

Figure 5.4: Incident energy dependence of global nuclear stopping $< R_{Eg}^{global} >$ (left panels) and local nuclear stopping $< R_E^{local} >$ (right panels) for scaled impact parameter, $\hat{b} = 0.3$ and stiffness parameter, $\gamma = 0.66$ and $\gamma = 1.33$. The inset graph is from 150 MeV/nucleon to 600 MeV/nucleon. The solid and open symbols are for $\gamma = 0.66$ and $\gamma = 1.33$ respectively.

suffering deflection in transverse direction decreases and hence stopping decreases with increase in mass asymmetry. Also in mass asymmetric nuclear collisions, the maximum value of density is less compared to mass symmetric nuclear collisions. The influence of density-dependent symmetry energy corresponding to two different stiffness constants ($\gamma = 0.66$ (panel a) and $\gamma = 1.33$ (panel b)) cannot be seen clearly from Fig. 5.4(a and b). Therefore, in Fig. 5.4 (c), the $< R_E^{local} >$ due to light mass fragments ($A_f \leq 4$) have

been shown, which are originated from participant zone only. Since the density reached in participant zone or collision zone (local density) is higher than global density due to compression, therefore the influence of stiffness factors cannot be seen clearly in case of $< R_E^{global} >$. To display the variation more clearly, the $< R_E^{local} >$ due to participant zone fragments have been scaled by constant factors.

Inset Fig. 5.4(d) show the variation more clearly in $< R_E^{local} >$ due to two different values of stiffness factors (i.e. $\gamma = 0.66$ and $\gamma = 1.33$), here the values of $< R_E^{local} >$ are not scaled.

5.2.5 Stiffness factor and mass asymmetry factor dependence of global and local nuclear stopping

Further, to extract the role of symmetry energy on nuclear stopping, we have displayed $< R_E^{global} >$ and $< R_E^{local} >$ for different values of stiffness constants and mass asymmetry factors in Fig. 5.5(a, b, c and d). $< R_E^{global} >$ is influenced least by the stiffness constants and the role of mass asymmetry is dominating as shown in Fig. 5.5(a and b). But if one concentrate on $< R_E^{local} >$, the influence of different values of stiffness constants can be clearly seen as shown in Fig. 5.5(c and d). This shows that theory is capable of showing the effect of different strengths of symmetry energy. But since isotopic asymmetry for the reactions undertaken is very small (~ 0.1), therefore one can see the extremely small effect. Although one cannot calculate the nuclear stopping experimentally directly, but by choosing the participant zone based on midrapidity criteria, one can calculate the local stopping.

5.2.6 Mass asymmetry dependence of the slopes

Since the influence of symmetry energy can be seen at higher energies, therefore we have fitted the $< R_E^{global} >$ and $< R_E^{local} >$ values in Fig. 5.4 and results have been displayed in Fig. 5.6 in the following manner :

(i) upto E = 150 MeV/nucleon in Fig. 5.6(a and b),

(ii) above E = 150 MeV/nucleon in Fig. 5.6(c and d) and

(iii) over whole energy range under consideration in Fig. 5.6 (e and f) respectively.

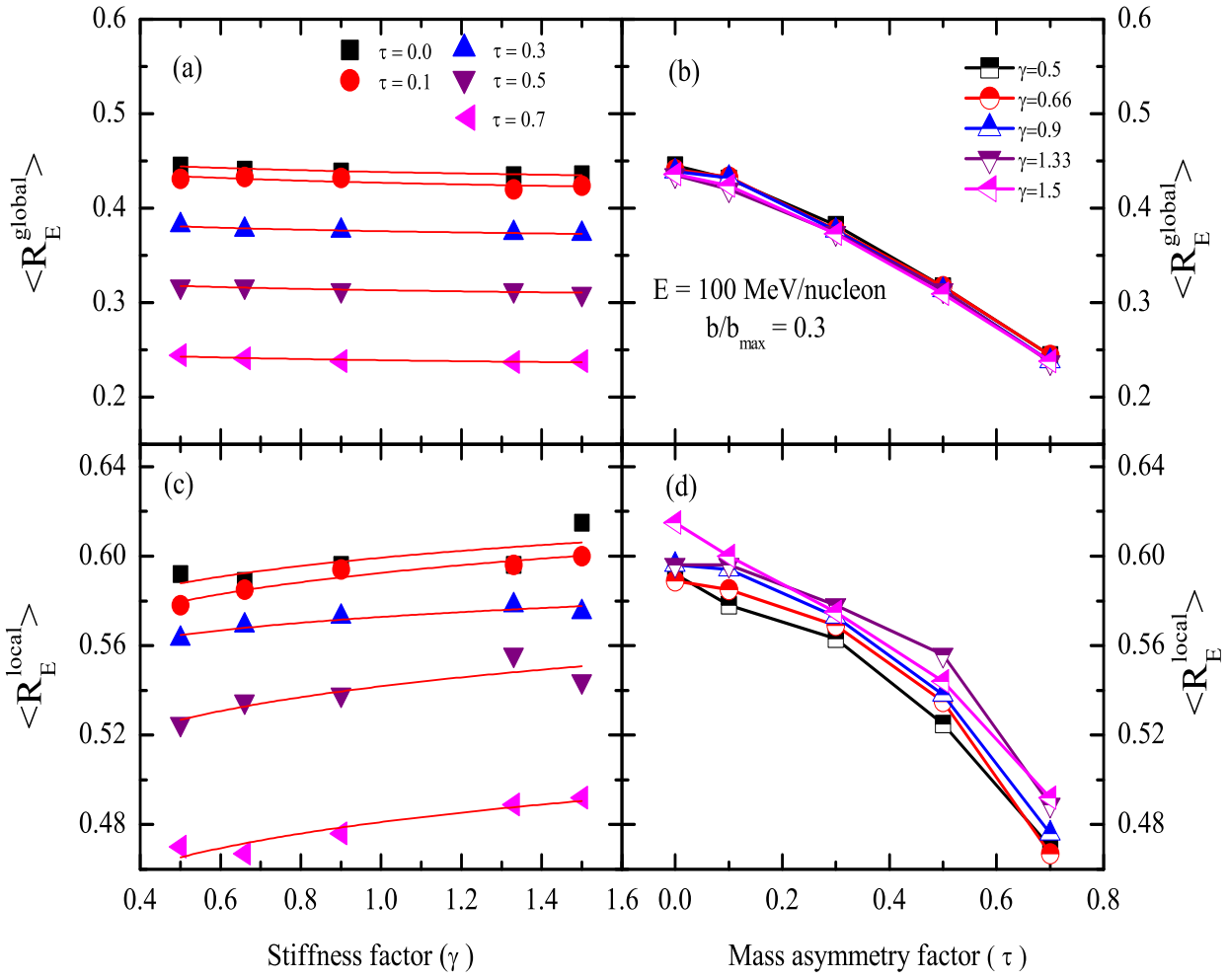

Figure 5.5: Stiffness factor and mass asymmetry factor dependence of global nuclear stopping $< R_E^{global} >$ and local nuclear stopping $< R_E^{local} >$ at incident energy of 100 MeV/nucleon and $\hat{b} = 0.3$

In Fig. 5.6 (a and b), for energies up to 150 MeV/nucleon, there is a small variation in the slopes of $< R_E^{global} >$ and $< R_E^{local} >$, indicating satisfactory role of symmetry energy. The slope of $< R_E^{global} >$ is larger for higher mass asymmetry whereas it is smaller in case of $< R_E^{local} >$ for the same mass asymmetry. Below 150 MeV/nucleon, the rate of change of $< R_E^{global} >$ is not more. This implies stopping is not more and rotation of matter is taking place as we go towards higher mass asymmetry. The rate of change of $< R_E^{local} >$ decreases as mass asymmetry increases. The variation in the slope of stopping with mass asymmetry factor for energies above 150 MeV/nucleon is more for $< R_E^{global} >$ compared

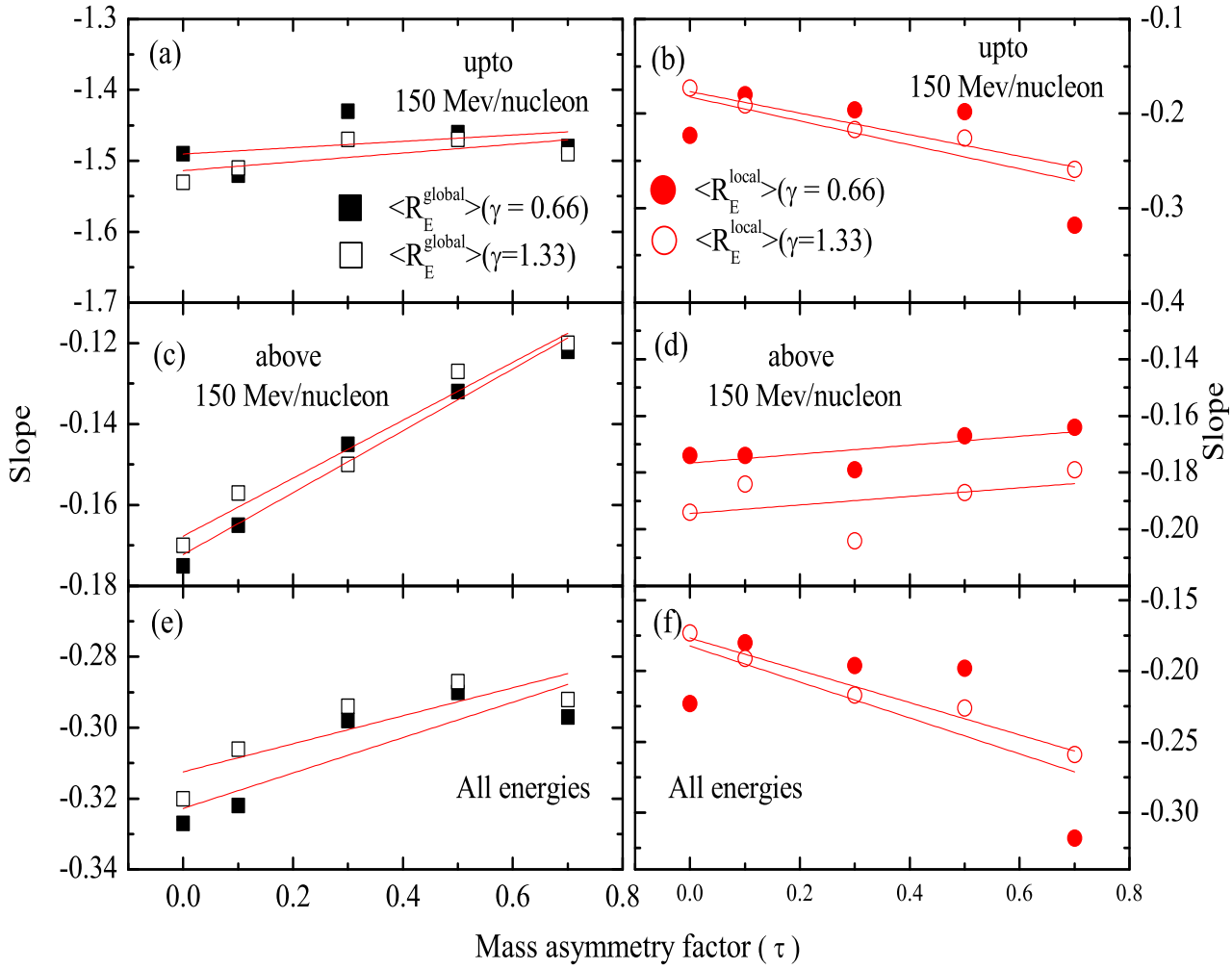

Figure 5.6: Mass asymmetry dependence of the slopes of $< R_E^{global} >$ and $< R_E^{local} >$ for energies upto 150 MeV/nucleon (a and b) , above 150 MeV/nucleon (c and d) and whole energy range (e and f) for $\gamma = 0.66$ and $\gamma = 1.33$ at $\hat{b} = 0.3$.

to $< R_E^{local} >$ as shown in Fig. 5.6(c and d). The rate of change of $< R_E^{global} >$ is more at higher mass asymmetry. This is due to the reason that the matter gets scattered in different directions. It shows that global stopping is influenced more by mass asymmetry than local stopping. But the influence of stiffness factor can be clearly seen in local stopping. The density of the combined system is specifically comparable to the beam energy. As a result, it influences the strength of symmetry energy at densities above and underneath saturation density. In Fig. 5.6 (e and f), the influence of symmetry energy is more for $< R_E^{local} >$ for whole energy range considered. Also the relative change in stopping is more incase of $< R_E^{global} >$ in comparison to $< R_E^{local} >$.

5.2.7 Impact parameter dependence of the global nuclear stopping parameter $< R_E^{global} >$

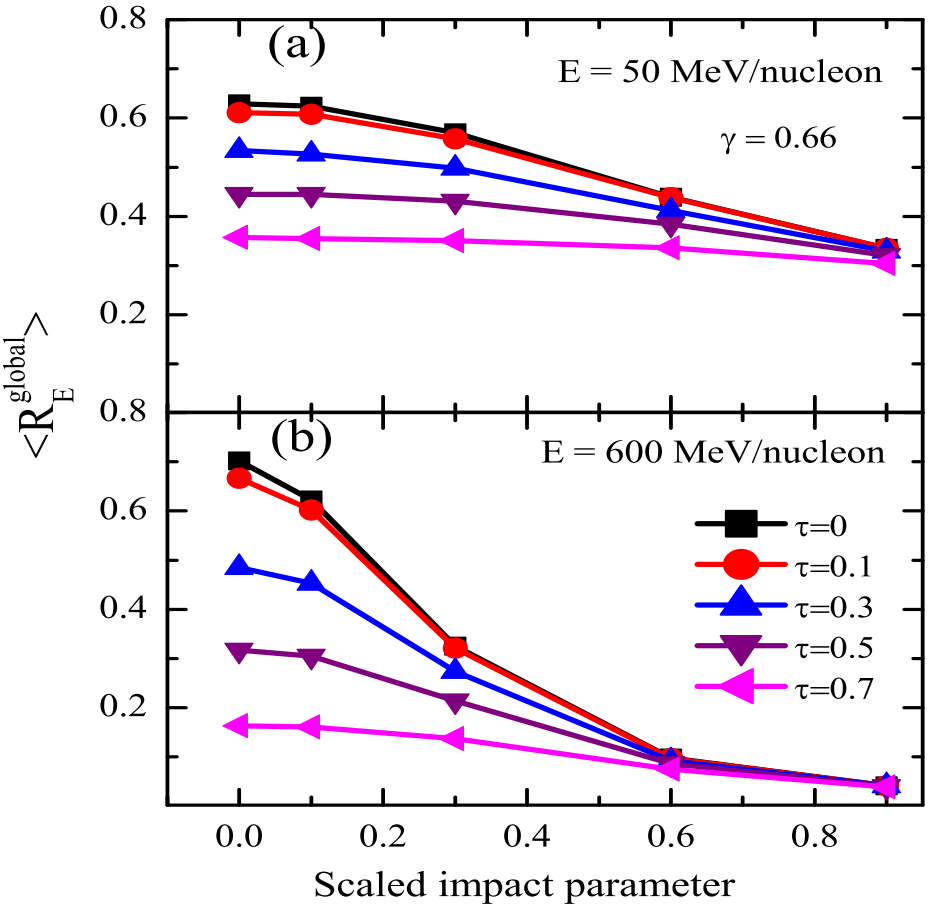

Figure 5.7: Impact parameter dependence of the global nuclear stopping parameter $< R_E^{global} >$ at an incident energy of 50 MeV/nucleon and 600 MeV/nucleon for $\gamma = 0.66$.

The nuclear stopping is additionally affected by impact parameter. The impact parameter dependence of $< R_E^{global} >$ at 50 MeV/nucleon and 600 MeV/nucleon for the soft density dependence of symmetry energy i.e. $\gamma = 0.66$ has been displayed in Fig. 5.7. As the impact parameter increases one can see a non-linear decrease in the $< R_E^{global} >$ at both the incident energies. At smaller impact parameter, there is a large participant matter which corresponds to smaller contribution of the longitudinal (p_l) momentum of particles and larger magnitude of transverse (p_t) momentum of particles resulting in an increase in nuclear stopping. However, the larger impact parameter tends to increase the role of spectator matter due to which longitudinal momentum of the particles dominates

and the value of stopping decreases for all the mass asymmetric reactions. The present results indicates that at extreme peripheral geometries (impact parameter), the participant zone becomes very small. At all colliding geometries, except for the extreme peripheral geometries, $< R_E^{global} >$ shows a significant dependence on τ.

The lesser $< R_E^{global} >$ of the system in extreme mass asymmetric heavy ion reactions can be considered as a significant evidence that the average density will be very much different along the whole system zone (participant and spectator matter) compared to the symmetric heavy ion reactions. The equilibration of the system is achieved when NN collisions cause the transfiguration of the initial longitudinal motion in different directions. The significant part played by the incident energy, NN cross section and DDSE disappear if impact parameter is increased. As the participant zone reduces with increment in colliding geometry, the stopping also decreases. The degree of stopping has been correlated with colliding geometry in the literature [232].

5.2.8 Comparison with experimental data

The theoretical results compared with experimental data verify the accuracy of the adopted approach. Using the same approach one can predict the results, which can be verified by experimentalists. In Fig. 5.8, author shows the incident energy vs $< R_E^{global} >$ and compared results with data from experiments [119]. The nuclear stopping for complete fragment phase space ($A >1$) has been shown in order to show a better comparison with the data [164]. It is evident from the figure that stopping of fragment phase space yields better results. The outcomes acquired through our theoretical estimations utilizing soft form of DDSE ($\gamma = 0.66$) yields a decent concurrence with the experimental data especially at higher energies. Recent investigations have proved that the most suitable strength of symmetry energy corresponds to stiffness factor ($\gamma = 0.69$). This strength of DDSE presents a better understanding of nuclear EOS. Many of the properties of neutron stars and a compressibility $K \sim 230$ MeV and 0.21 fm as the neutron skin thickness for ^{208}Pb nuclei [297] also correspond to stiffness factor ($\gamma = 0.69$).

In Fig. 5.8 (a), the calculations comply with INDRA data above 60 MeV/nucleon (for panel (a) and panel (b)) and at lower energies the IQMD model overestimates the experimental results by giving higher value of stopping. At lower energies, i.e below 25

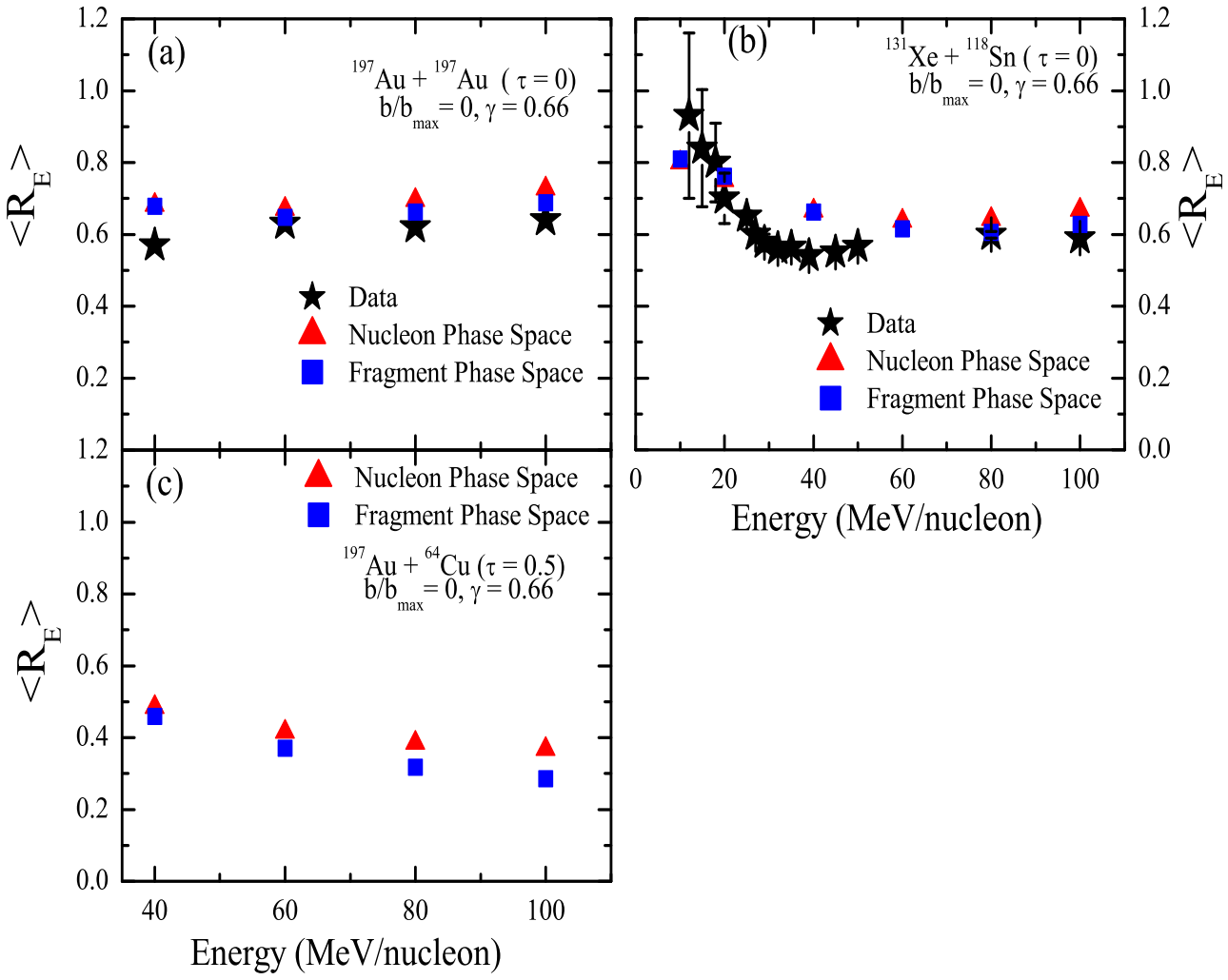

Figure 5.8: The comparison of experimental data with theoretical values of $< R_E^{global} >$ for Au + Au , Xe + Sn and Au + Cu reactions for central geometry and stiffness parameter,$\gamma = 0.66$

MeV/nucleon, the theoretical values of stopping predict complete nuclear stopping and therefore it becomes independent of symmetry energy and the NN cross sections, whereas experimental estimations do not attain complete stopping till the bombarding energy reaches 10 MeV/nucleon [298].

The minima of nuclear stopping in the data is around 40 MeV/nucleon (panel (a) and (b)) corresponding to a smooth transition from a mean-field behaviour to a two-body dissipation energy regime. At energies lower than the Fermi energy, there is a supremacy of the mean field as a consequence the longitudinal momentum associated with nucleons increments and stopping decreases. Nevertheless, phase space broadens for

in-medium two-body collisions above the Fermi energy. This culminates in the transfer of longitudinal component of nucleon momentum in transverse direction and leads to an increase in stopping. At very high energy, the NN collisions prompts lesser transfer of longitudinal component in transverse direction. Hence, stopping again decreases and transparency comes into picture. In IQMD calculations, below Fermi energy nuclear stopping declines **less** promptly than that of experiment for soft EOS and the values remain constant above Fermi energy. No minima is seen for nuclear stopping in the results shown here. As the incident energy increases nuclear stopping caused by the mean field weakens due to which allowed collisions are increasing and hence the nuclear stopping increases gradually. There is a transition from nucleus-nucleus collision to NN collision with increasing energy. Since the experimental data for highly asymmetric collisions is not available, therefore we have shown the prediction for $^{197}_{79}Au +^{64}_{29}Cu$ reaction. Here, the $< R_E^{global} >$ especially for fragment phase space using soft density dependence of symmetry energy along with experimental data can give a real picture of the dynamics in mass asymmetric reactions. Our observations depend on the incident energy beneath 100 MeV/nucleon, where a tremendous variation in the density and symmetry energy is not prominent. However, in case of mass asymmetric reactions the role of DDSE becomes more complex. Thus, theoretical and experimental based investigations on the determination of density dependent symmetry energy may compulsorily take care of this complexity in case of asymmetric heavy ion reactions.

5.2.9 Incident energy dependence of stopping ratio (100S) and mean free path

In Fig. 5.9, author display the stopping ratio for the reaction $^{131}_{54}Xe+^{118}_{50}Sn$ and compared the theoretical values with the experimental values given by Lopez *et al.*, [120]. The stopping ratio can be defined as a normalized quantity S which gives the estimate for the stopping reached in a given dataset. It can be mathematically represented as :

$$S = \frac{R_E^p - R_E(\alpha = 1)}{R_E(\alpha = 0) - R_E(\alpha = 1)} \tag{5.3}$$

This quantity is always positive since $R_E^p > R_E(\alpha = 1)$ and $R_E(\alpha = 0) > R_E(\alpha = 1)$. When the isotropy ratio is compared at two extreme values ($\alpha = 1$ and $\alpha = 0$), the ex-

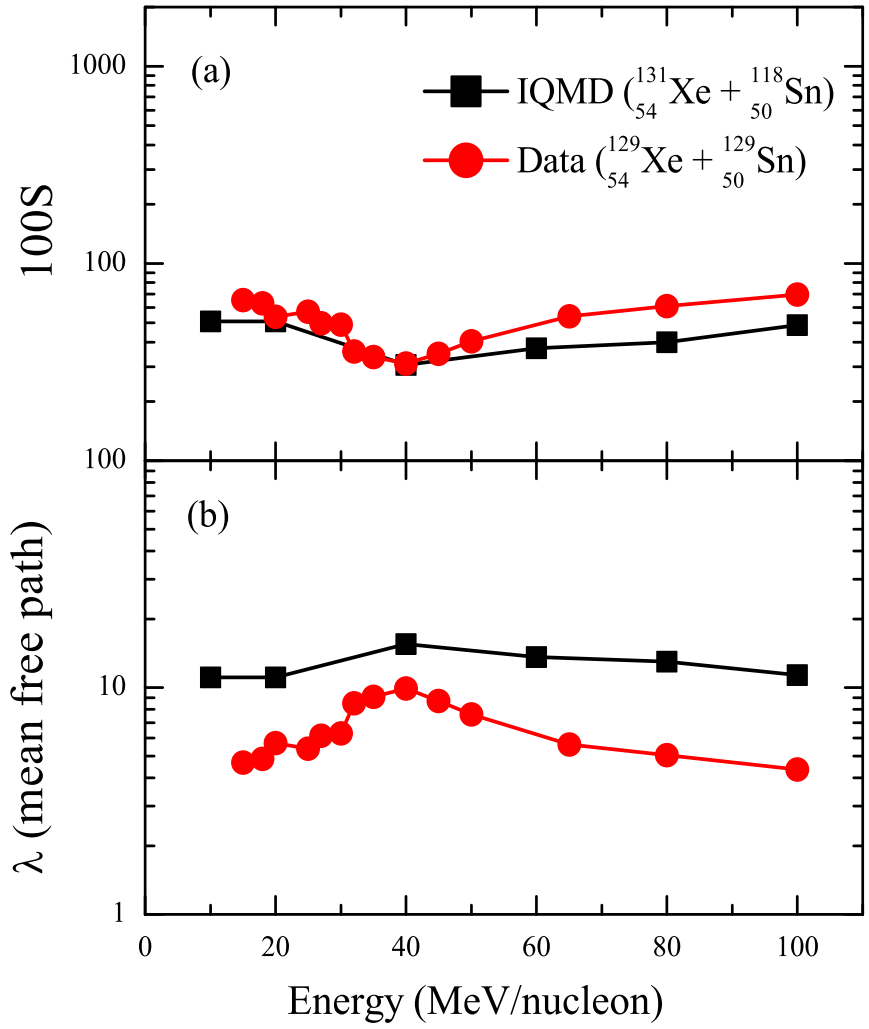

Figure 5.9: The incident energy dependence of stopping ratio (100S) and mean free path for nearly symmetric reaction and comparison with experimental data.

pression helps in extracting a more quantitative value for stopping. The parameter $\alpha = 1$ corresponds to complete transparency (no dissipation) and $\alpha = 0$ corresponds to full stopping. The theoretical values for the isotropy ratio, $R_E(\alpha)$ were calculated by putting the experimental values of α given by Lopez *et al.*, [120] in the following expression:

$$R_E(\alpha) = \frac{1}{1 + 5x\alpha/4} \tag{5.4}$$

where $x = E_{inc}/E_{Fermi}$ and $E_{Fermi} = 38$ MeV is the Fermi energy at saturation density.

The mean-free path, λ, of a nucleon in the nuclear medium is a fundamental transport coefficient and an essential ingredient of many theoretical and experimental findings [299].

In the lower panel, we show λ of a nucleon in nuclear matter against incident energy. Author finds that λ is maximum around E= 35 - 45 MeV/nucleon thus corresponding to a minimum value for stopping as seen in the upper panel of Fig. 5.9 and reaches $\lambda = (9\pm2)$ fm. The theoretical values lie too close to the experimental data of stopping ratio and λ. This portrays the fact that the Pauli principle stifles NN collisions to an expansive degree at low bombarding energy and subsequently builds λ around the Fermi energy. The abatement seen at lower incident energy here is credited to mean-field impacts, for which the dissipation mechanism is for the most part given by 1-body rather than 2-body dissipation [120]. If we now concentrate in the intermediate energy region, i.e. above the Fermi energy, we take note of a constant lessening of NN collisions, irrespective of the system size, toward an asymptotic value akin to $\lambda = (5 \pm 1)$ fm.

In Fig. 5.10, we display the stopping ratio and bring attention to the location of the minimal stopping value in the range E = 45 - 100 MeV/nucleon. In the figure, stopping ratio for mass symmetric and mass asymmetric reactions have been given. The stopping ratio for mass symmetric reaction (τ=0.0) has a larger minima in the energy range E = 45 - 100 MeV/nucleon. As the mass asymmetry increases the minima decreases for the same energy range. After 150 MeV/nucleon, the stopping ratio again decreases further.

In the lower panel, we display λ of a nucleon travelling through nuclear matter for mass symmetric and asymmetric systems. The maxima of λ lies in the energy range E = 45 - 100 MeV/nucelon and is highest for mass symmetric reaction. The maxima gradually decreases with the increase in mass asymmetry of the reaction. If the radius of the target nucleus is huge regarding the λ of the projectile then there will be numerous scatterings of the nucleons. If the scattering λ for a neutron or proton traversing nuclear matter becomes comparable to the nuclear radius, transparency comes into picture. The λ for a nucleon travelling through nuclear matter (colliding with the surrounding nucleons) may likewise be identified with the effective, isospin averaged cross section for a NN collision through the expression: $\lambda = 1/\sigma\rho$. The density has been chosen because the two nuclei strongly overlap each other in coordinate space. At higher energy, λ builds on account of the smaller NN cross section. If the λ is larger than the inter nucleon distance d, the scattering from various nucleons in the nucleus can be thought to be roughly autonomous of each other. Both the nuclear transparency and the nucleon mean free path are seen to

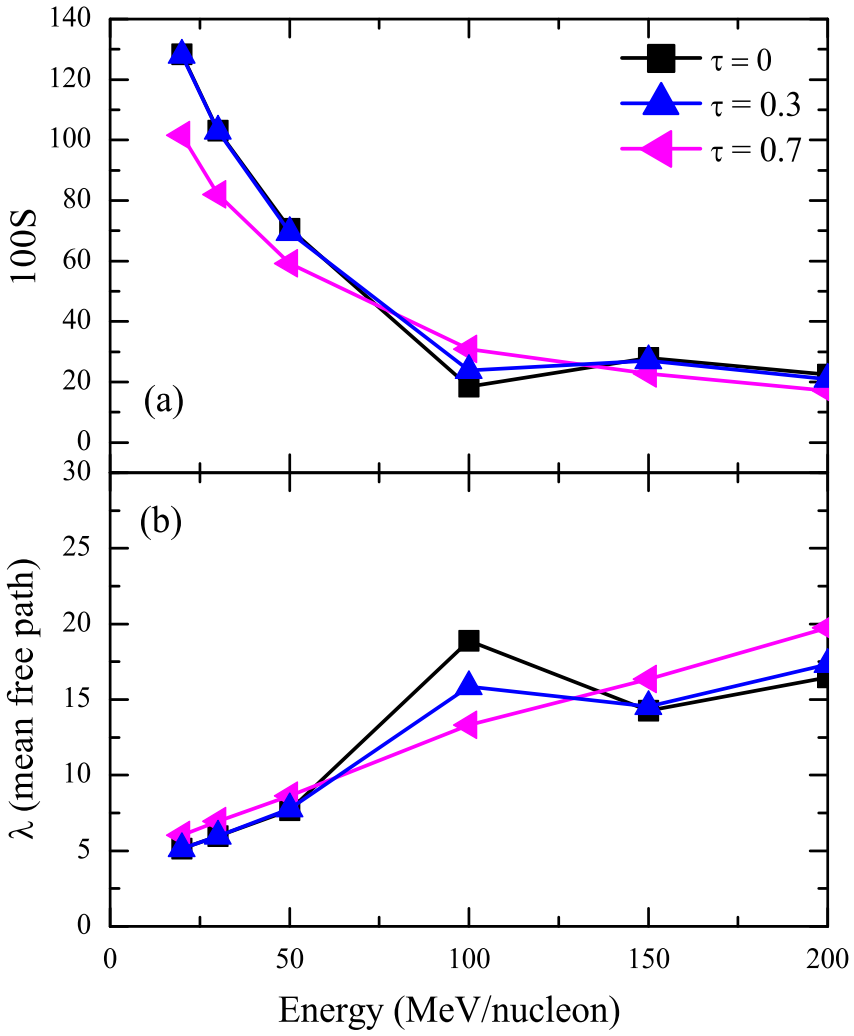

Figure 5.10: The incident energy dependence of 100S and mean free path (λ) for mass asymmetry 0, 0.3 and 0.7.

increase with energy. The λ is essentially similar for all nuclei [300, 301].

5.3 Summary

We summarize the fact that the $< R_E^{global} >$ of the system is drastically affected by the mass asymmetry factor of the colliding partners (target and projectile) in intermediate energy HICs. The incident energy, stiffness factor γ and mass asymmetry dependence of stopping parameters clearly indicates that the dynamics of mass asymmetric reactions is very much different from mass-symmetric reactions.

(i) The symmetry energy (density dependent) does not produce any noticeable change in

$< R_E^{global} >$ of the system during the whole time span of the reaction (for all τ values) which have also been predicted in many previous theoretical results. Although, different τ values affect the $< R_E^{global} >$ on a large scale but $< R_E^{global} >$ fails to elaborate the role of symmetry energy. However, influence of density dependent symmetry energy can be seen more clearly in $< R_E^{local} >$.

(ii) A quantum of experimental data about fragment yield for mass symmetric reactions is available in the literature. However, the comparison of theoretical predictions with experimental finding (for asymmetric reactions) may lead to much more fundamental, though indirect understanding of the thermodynamical state of nuclear matter at initial as well as at later stages of the reaction. Further study in this domain can surely provide greater clarity about the thermodynamical properties, nuclear interactions/correlations and isospin dependent part of nuclear EOS (symmetry energy) in mass asymmetric reactions at intermediate energies. Theoretical results discussed in this chapter can be verified in the experiments in which light mass projectile can be used e.g. VECC Kolkata (India) and RIKEN (Japan).

(iii) Stopping ratio (S) and mean free path give important information that reaction dynamics of mass asymmetric collisions is entirely different from mass symmetric collisions.

Chapter 6

Summary and outlook

This thesis contains a theoretical investigation of mass symmetric and mass asymmetric nuclear reactions exploring the role of the DDSE. At first, author analyzed the influence of initialization parameters on multi fragmentation and flow by utilizing the two dynamical transport models (QMD and IQMD). Author has examined the initialization parameters i.e. physics as well as technical parameters and inferred that the observables like multi fragmentation and flow depend on mean field potential parameters, Coulomb and symmetry potentials (isospin dependent) as well as the initialization conditions of the models. It has been concluded that reaction dynamics is significantly influenced by initialization parameters. The present study infers that considering the present scenario IQMD (isospin effects) has edge over QMD model in explaining the different observable associated with HICs.

Keeping in mind the above said conclusions, study of different mass-asymmetric reactions using different parameterizations of DDSE is performed. It is observed that intermediate mass fragment <IMF> production is highly sensitive to the mass-asymmetry factor (τ) for both central and peripheral collisions. One cannot rely on the yield of heavy fragments to decipher the strength of DDSE, in case of extreme mass-asymmetric as well as symmetric HICs. Analyzing multifragmentation at low incident energies one can extract information regarding isospin dependence of nucleonic interactions. Yield of smaller fragments (like neutron/proton emission) is observed to be more appropriate to verify the behavior of DDSE even in extreme mass-asymmetric reactions. Free nucleons indicate minor affectability to various density dependent parameterizations compared to heaviest fragment $< A_{\max} >$ which demonstrates almost no affectability at $E = 50$ MeV/nucleon.

Lastly, we summarize the fact that the global nuclear stopping of the system is inordinately affected by the mass asymmetry factor of the colliding accomplices (target and projectile) in intermediate energy HICs. The incident energy, stiffness factor γ and mass asymmetry dependence of stopping parameters clearly indicates that the dynamics of mass asymmetric reactions is very much different from mass-symmetric reactions. The DDSE does not produce any perceptible change in global nuclear stopping of the system amid the whole time span of the reaction (for all τ values) which was also anticipated in numerous theoretical outcomes. Albeit, different τ values influence the global nuclear stopping $< R_E^{global} >$, but it fails to elaborate the role of DDSE. However, influence of DDSE can be seen more clearly in local nuclear stopping, $< R_E^{local} >$. A quantum of experimental data about fragment yield for mass symmetric reactions is available in the literature. However, the comparison of theoretical predictions with experimental finding (for asymmetric reactions) may prompt a much more fundamental, though indirect understanding of the thermodynamical state of nuclear matter at introductory as well as later phases of the reaction.

Further study in this domain can surely provide more noteworthy clarity about the thermodynamical properties, nuclear interactions/correlations and isospin dependent part of nuclear EOS in mass asymmetric reactions at intermediate energies. Theoretical outcomes discussed in this chapter can be verified in the experiments in which light mass projectile can be used e.g. VECC Kolkata (India) and RIKEN (Japan). In the case of extreme mass-asymmetric as well as symmetric HICs, the better candidate to rely upon is participant zone. In this manner, one can profoundly explore the dynamics of symmetric and mass asymmetric reactions by taking participant zone into account. One can incorporate the pairing energy in the primary model, since it will give better stability to final stage fragments. Also calculation of density of only participant zone using rapidity bins in mass asymmetric reactions will open new domain in this direction. Author expects that present study would be helpful to comprehend the reaction dynamics of mass asymmetric collisions. Additionally present study would be useful to produce stable isotopes which can be utilized in medical science (eg. hadron beam therapy for treating cancer).

Bibliography

[1] B. K. Agrawal, R. Kumar and S. K. Dhiman, Phys. Rev. D **77**, 087301 (2008).

[2] A. Bohnet *et al.*, Phys. Rev. C **44**, 2111 (1991).

[3] A. Faessler, W. H. Dickhoff and M. Trefz, Nucl. Phys. A **428**, 271c (1981).

[4] J. Aichelin *et al.*, Phys. Rev. Lett. **58**, 1926 (1987).

[5] Li. Zhuxia *et al.*, Phys. Rev. C **44**, 824 (1991).

[6] D. J. Magestro, Ph. D. Thesis, Michigan State University (2000).

[7] S. Voloshin and Y. Zhang, Z. Phys. C **70**, 665 (1996).

[8] P. Danielewicz, R. Lacey and W. G. Lynch, Science **298**, 1592 (2002).

[9] R. T. de Souza *et al.*, Eur. Phys. J. A **30**, 275 (2006).

[10] S. Kubis and M. Kutschera, Nucl. Phys. A **720**, 189 (2003).

[11] S. Kubis, Phys. Rev. C **76**, 025801 (2010).

[12] H. Müller and B. D. Serot, Phys. Rev. C **72**, 2072 (1995).

[13] http://www.fair-center.eu/public/what-happens-at-fair/basic-science/nuclear-matter-physics.html

[14] A. B. Migdal, Phys. Lett. B **45**, 448 (1973).

[15] P. Cejnar, J. Jolie and R. F. Casten, Rev. Mod. Phys. **82**, 2155 (2010).

[16] B. Borderie, M. F. Rivet *et al.*, Prog. Part. Nucl. Phys. **61**, 551 (2008).

[17] J. M. Lattimer and Andrew W. Steiner, Eur. Phys. J. A **50**, 40 (2014).

[18] P. B. Demorest *et al.*, Nature **467**, 1081 (2010).

[19] J. Antoniadis *et al.*, Science **340**, 1233232 (2013).

[20] C. F. Weizsacker, Z. Phys. **96**, 431 (1935).

[21] H. A. Bethe and R. F. Bacher, Rev. Mod. Phys. **8**, 82 (1936).

[22] J. L. Basdevant, J. Rich and M. Spiro, Fundamentals in nuclear physics, Springer,(2005).

[23] J. Aichelin, Phys. Report **202**, 233 (1991).

[24] G. F. Bertsch and S. Das Gupta, Phys. Rep. **4**, 189 (1988).

[25] M. Lopez-Quelle *et al.,* Nucl. Phys. A **483**, 479 (1988)

[26] T. Li *et al.,* Phys. Rev. Lett. **99**, 162503 (2007).

[27] U. Garg *et al.,* Nucl. Phys. A **788**, 36 (2007).

[28] M. M. Sharma *et al.,* Phys. Rev. C **38**, 2562 (1988).

[29] S. Shlomo and D. H. Youngblood, Phys. Rev. C **47**, 529 (1993).

[30] C. J. Pethick *et al.*, Nucl. Phys. A **584**, 675 (1995).

[31] C. P. Lorenz *et al.*, Phys. Rev. Lett. **70**, 379 (1993).

[32] M. M. Sharma *et al.*, Phys. Lett. B **312**, 377 (1993).

[33] Y. Sugahara *et al.*, Nucl. Phys. A **579**, 557 (1994).

[34] P. G. Rheinhard *et al.*, Z. Phys. A **323**, 13 (1986).

[35] J. P. Blaizot *et al.*, Nucl. Phys. A **591**, 435 (1995).

[36] I. Hamamoto, H. Sagawa and X. Z. Zhang, Phys. Rev. C **56**, 3121 (1997).

[37] David S. Falk and Lawrence Wilets, Phys. Rev. **124**, 1887 (1961).

[38] B. Jakobsson *et al.*, Nucl. Phys A **509**, 195 (1990).

[39] H. W. Barz *et al.*, Nucl. Phys A **548**, 427 (1992).

[40] D. Sisan, W. Bauer, O. Bjarki *et al.*, Phys. Rev. C **63**, 027602 (2001).

[41] J. K. Dhawan and R. K. Puri, Phys. Rev. C **75**, 057901 (2007).

[42] Y. G. Ma and W. Q. Shen, Phys. Rev. C **51**, 710 (1995).

[43] S. R. Souza *et al.*, Nuc. Phys. A **571**, 159 (1994).

[44] M. Begemann-Blaich, W. F. J. Müller, J. Aichelin *et al.*, Phys. Rev. C **48**, 610 (1993).

[45] K. J. Eskola *et al.*, Nucl. Phys. B **323**, 37 (1989).

[46] O. Hartmann, Dissertation, TU Darmstadt (2003).

[47] V. Kaur and Suneel Kumar, Phys. Rev. C **81**, 064610 (2010).

[48] J. Gosset *et al.*, Phys. Rev. C **16**, 629 (1977).

[49] Bao-An Li, Lie-Wen Chen, Che Ming Ko, Phys. Rep. **464**, 113 (2008).

[50] A. W. Steiner *et al.*, Phys. Rep. **411**, 325 (2005).

[51] B. A. Li, C. M. Ko, and W. Bauer, Int. J. of Mod. Phys. E **7**, 147 (1998).

[52] K. A. Brueckner *et al.*, Phys. Rev. B **134**, 722 (1964).

[53] B. A. Li and X. Han, Phys. Lett. B **727** 276 (2013).

[54] C. J. Horowitz *et al.*, J. Phys. G **41**, 093001 (2014).

[55] S. Kowalski *et al.*, Phys. Rev. C **75**, 014601 (2007).

[56] P. Russotto *et al.*, Phys. Lett. B **697** 471 (2011).

[57] P. Russotto *et al.*, Phys. Rev. C **94** 034608 (2016).

[58] I. I. Gurevich *et al.*, Dokl. AN SSSR. **18**, 169 (1938)

[59] E. Schopper, Naturwiss. **25**, 557 (1937).

[60] O. V. Lozhkin *et al.*, Zh. Eksp. teor. Fiz. **31**, 913 (1956).

[61] N. Buyukcizmeci, R. Ogul and A. S. Botvina, Eur. Phys. J. A **25**, 57 (2005).

[62] http://www.nupecc.org

[63] V. Baran *et al.*, Phys. Rep. **410**, 335 (2005).

[64] D. T. Khoa *et al.*, Nucl. Phys. A **542**, 671 (1992).

[65] D. T. Khoa *et al.*, Nucl. Phys. A **548**, 102 (1992).

[66] R. K. Puri *et al.*, Nucl. Phys. A **575**, 733 (1994).

[67] M. B. Tsang *et al.*, Phys. Rev. Lett. **57**, 559 (1986).

[68] P. Danielewicz *et al.*, Phys. Lett. B **157**, 146 (1985).

[69] P. Danielewicz *et al.*, Phys. Rev. C **38**, 120 (1988).

[70] K. G. R. Doss *et al.*, Phys. Rev. Lett. **59**, 2720 (1987).

[71] G. F. Bertsch *et al.*, Phys. Lett. B **157**, 146 (1985).

[72] K. G. R. Doss *et al.*, Phys. Rev. Lett. **57**, 302 (1986).

[73] W. Scheid, H. Müller and W. Greiner, Phys. Rev. Lett. **32**, 741 (1974).

[74] C. A. Ogilvie *et al.*, Phys. Rev. C **40**, 2592 (1989).

[75] S. Goyal *et al.*, Nucl. Phys. A **853**, 164 (2011).

[76] J. Lukasik and W. Trautmann, in Proceedings of the International Nuclear Physics Conference, INPC2007 (Tokyo) 2, 513 (2008).

[77] B. Hong *et al.*, Phys. Rev. C **66**, 034901 (2000).

[78] Q. Pan and P. Danielewicz , Phys. Rev. Lett. **70**, 2062 (1993).

[79] J. Lukasik *et al.*, Phys. Lett. B **608**, 223 (2005).

[80] C. Hartnack *et al.*, Eur. Phys. J. A **1**, 151 (1998).

[81] R. W. Minich *et al.*, Phys. Lett. B **118**, 458 (1982).

[82] J. E. Finn *et al.*, Phys. Rev. Lett. **49**, 1321 (1982).

[83] J. Hubele *et al.*, Z. Phys. A **340**, 263 (1991).

[84] S. C. Jeong *et al.*, Phys. Rev. Lett. **72**, 3468 (1994).

[85] J. P. Alard *et al.*, Phys. Rev. Lett. **69**, 889 (1992).

[86] P. Desesquelles *et al.*, Phys. Rev. C **48**, 1828 (1993).

[87] R. T. de Souza *et al.*, Phys. Lett. B **268**, 6 (1991).

[88] G. F. Peaslee *et al.*, Phys. Rev. C **49**, R2271 (1994).

[89] E. Plagnol, Nouv. Ganil **44**, 3 (1993).

[90] A. S. Hirsch *et al.*, Phys. Rev. C. **29**, 508 (1984).

[91] V. V. Avdeichikov *et al.*, Yad. Fiz. **48**, 1736 (1988).

[92] A. I. Warwick *et al.*, Phys. Rev. C **27**, 1083 (1983).

[93] L. Phair *et al.*, Phys. Rev. Lett. **75**, 213 (1995).

[94] L. Phair, L. G. Moretto and G. J. Wozniak, Phys. Rev. Lett. **77**, 822 (1996).

[95] T. C. Sangster *et al.*, Phys. Rev. C **46**, 1404 (1992).

[96] D. R. Bowman *et al.*, Nucl. Phys. A **523**, 386 (1991).

[97] P. R. Chomaz *et al.*, Nucl. Phys. A **552**, 508 (1993).

[98] J. B. Elliott, L. G. Moretto and L. Phair, Phys. Rev. C **71**, 024607 (2005).

[99] B. K. Srivastva *et al.*, Phys. Rev. C **65**, 054617 (2002).

[100] http://www-aladin.gsi.de.

[101] S. Piantelli *et al.*, Nucl. Phys. A **809**, 111 (2008)

[102] S. Piantelli *et al.*, Phys. Lett. B **627**, 18 (2005).

[103] J. Lukasik *et al.*, Phys. Rev. C. **55**, 1906 (1997).

[104] A. Schüttauf *et al.*, Nucl. Phys. A **607**, 457 (1996).

[105] J. Hubele *et al.*, Z. Phys. A **340**, 263 (1991).

[106] C. A. Ogilvie *et al.*, Phys. Rev. Lett. **67**, 1214 (1991).

[107] R. Ogul *et al.*, Phys. Rev. C **83**, 024608 (2011).

[108] H. Imal *et al.*, Phys. Rev. C **91**, 034605 (2015).

[109] D. R. Bowman *et al.*, Phys. Rev. Lett. **67**, 1527 (1991).

[110] C. Y. Wong, Introduction to High-Energy Heavy-Ion Collisions (World Scientific, Singapore, 1994).

[111] B. A. Li and C. M. Ko, Nucl. Phys. A **601**, 457 (1996).

[112] B. Hong, N. Herrmann, J. L. Ritman *et al.*, Phys. Rev. C **57**, 244 (1998).

[113] F. Rami *et al.*, Phys. Rev. Lett. **84**, 1120 (2000).

[114] B. Hong *et al.*, Phys. Rev. C **66**, 034901 (2002).

[115] W. Reisdorf *et al.*, Phys. Rev. Lett. **92**, 232301 (2004).

[116] W. Reisdorf *et al.*, Nucl. Phys. A **848**, 366 (2010).

[117] A. Andronic *et al.*, Phys. Rev. C **64**, 041604(R) (2001).

[118] A. Andronic *et al.*, Eur. Phys. J. A **30**, 31 (2006).

[119] G. Lehaut *et al.*, Phys. Rev. Lett. **104**, 232701 (2010).

[120] O. Lopez *et al.*, Phys. Rev. C **90**, 064602 (2014).

[121] H. Ströbele *et al.*, Phys. Rev. C **27**, 1349 (1983).

[122] A. Baden *et al.*, Nucl. Instr. Meth. **203**, 189 (1982).

[123] R. E. Renfordt *et al.*, Phys. Rev. Lett. **53**, 763 (1984).

[124] R. Pak *et al.*, Phys. Rev. Lett. **78**, 1022 (1997); *ibid* **78**, 1026 (1997).

[125] C. A. Ogilvie *et al.*, Phys. Rev. C **42**, R10 (1983).

[126] D. Krofcheck *et al.*, Phys. Rev. Lett. **63**, 2028 (1989).

[127] A. Andronic *et al.*, Phys. Rev. C **67**, 034907 (2003).

[128] W. Trautmann *et al.*, Prog. Part. Nucl. Phys. **62**, 425 (2009).

[129] Z. Kohley *et al.*, Phys. Rev. C **83**, 044601 (2011).

[130] J. Cugnon, P. Deneye and A. Lejeune, Z. Phys. A **328**, 409 (1987).

[131] I. Bombaci and U. Lombardo, Phys. Rev. C **44**, 1892 (1991).

[132] W. Zuo, A. Lejeune, U. Lombardo, J. F. Mathiot, Eur. Phys. J. A **14**, 469 (2002).

[133] B. D. Serot and H. Uechi, Ann. Phys. (NY) **179**, 272 (1987).

[134] H. Müther, M. Prakash and T. L. Ainsworth, Phys. Lett. B **199**, 469 (1987).

[135] H. Huber, F. Weber and M. K. Weigel, Phys. Lett. B **317**, 485 (1993).

[136] H. Huber, F. Weber and M. K. Weigel, Phys. Rev. C **50**, R1287 (1994).

[137] C. Fuchs, T. Waindzoch, A. Faessler and D. S. Kosov, Phys. Rev. C **58**, 2022 (1998).

[138] Z. Y. Ma, J. Rong, B. Q. Chen, Z. Y. Zhu and H. Q. Song, Phys. Lett. B **604**, 170 (2004).

[139] H. Müther and A. Polls, Prog. Part. Nucl. Phys. **45**, 243 (2000).

[140] Y. Dewulf, D. Van Neck and M. Waroquier, Phys. Rev. C **65**, 054316 (2002) .

[141] J. Carlson, J. Morales Jr., V. R. Pandharipande and D. G. Ravenhall, Phys. Rev. C **68**, 025802 (2003).

[142] B. Friedman and V. R. Pandharipande, Nucl. Phys. A **361**, 502 (1981).

[143] R. B. Wiringa, V. Fiks and A. Fabrocini, Phys. Rev. C **38**, 1010 (1988).

[144] A. Akmal, V. R. Pandharipande and D. G. Ravenhall, Phys. Rev. C **58**, 1804 (1998).

[145] F. Zhang, C. Li, L. Zhu, H. Liu and F. S. Zhang, Phys. Rev. C **91**, 034617 (2015).

[146] J. Y. Liu, W. J. Guo, Y. Z. Xing, X. G. Li and Y. Y. Gao, Phys. Rev. C **70**, 034610 (2004).

[147] J. Y. Liu *et al.*, Phys. Rev. C **63**, 054612 (2001).

[148] G. Peilert, T. C. Sangster, M. N. Namboodiri and H. C. Britt, J. Phys. G **20**, 105 (1994).

[149] M. Di Toro, V. Baran, M. Colonna, S. Maccarone, M. Zielinska-Pfabe and H. H. Wolter, Nucl. Phys. A **681**, 426 (2001).

[150] M. Colonna, J. Rizzo, Ph. Chomaz and M. Di Toro, Nucl. Phys. A **805**, 454 (2008).

[151] B. A. Li, Phys. Rev. C **69**, 034614 (2004).

[152] K. S. Vinayak and Suneel Kumar, Jour. Phys. Conf. Series **381**, 012032 (2012).

[153] A. Sharma, A. Bharti, S. Gautam and R. K. Puri, Nucl. Phys. A **945**, 95 (2016).

[154] A. Sharma and A. Bharti, Eur. Phys. J. A **52**, 42 (2016).

[155] R. K. Puri, J. Singh and S. Kumar, Pramana J. Phys. **59**, 19 (2002).

[156] Suneel Kumar, Ph.D. Thesis, Panjab University, Chandigarh (India) 1999.

[157] Q. Wu *et al.*, Phys. Rev. C **91**, 014617 (2015).

[158] S. Kumar and R. K. Puri, Phys. Rev. C **60**, 054607 (1999).

[159] Y. K. Vermani and R. K. Puri, DAE Symposium on Nuclear Physics, IIT Roorkee (India), 22-26 December (2008).

[160] V. Baran, M. Colonna, M. D. Toro and V. Greco, Phys. Rev. Lett. **86**, 4492 (2001).

[161] H. Zheng, G. Bonasera, J. Mabiala, P. Marini, and A. Bonasera, Eur. Phys. J. A **50**, 167 (2014).

[162] W. Bauer, Phys. Rev. Lett. **61** 2534 (1998).

[163] G. F. Bertsch *et al.*, Nucl. Phys. A **490**, 745 (1988).

[164] G. Q. Zhang *et al.*, Phys. Rev. C **84**, 034612 (2011).

[165] E. Bonnet *et al.*, Phys. Rev. C **89**, 034608 (2014).

[166] B. A. Li *et al.*, Phys. Rev. C **71**, 054603 (2005).

[167] J. Y. Liu *et al.*, Phys. Rev. Lett. **86**, 975 (2001).

[168] Q. Li *et al.*, Chin. Phys. Lett. **19**, 321 (2002).

[169] Y. Zhang *et al.*, Phys. Rev. C **75**, 034615 (2007).

[170] Fen Fu *et al.*, Phys. Lett. B **666**, 359 (2008).

[171] Yang Yan-Fang *et al.*, Chin. Phys. Lett. **18**, 1040 (2001).

[172] S. Kumar *et al.*, Chin. Phys. Lett. **27**, 062504 (2010).

[173] S. Kumar, Suneel Kumar and R. K. Puri, Phys. Rev. C **81**, 014601 (2010).

[174] A. Jain, Suneel Kumar and R. K. Puri, Phys. Rev. C **84**, 057602 (2011).

[175] A. Jain and Suneel Kumar, J. Phys. G **41**, 105105 (2014).

[176] K. S. Vinayak and Suneel Kumar, J. Phys. G **39**, 095105 (2012).

[177] K. S. Vinayak and Suneel Kumar, Eur. Phys. J. A **48**, 96 (2012).

[178] V. Kaur, S. Kumar and R. K. Puri, Nucl. Phys. A **861**, 37 (2011).

[179] Jun Su and Feng-Shou Zhang, Phys. Rev. C **87**, 017602 (2013).

[180] Horst Stöcker, Jouchim A. Maruhn and Walter Greiner, Phys. Rev. Lett. **44**, 725 (1980).

[181] B. A. Li and S. J. Yennello, Phys. Rev. C **52**, R1746 (1995).

[182] L. W. Chen, F. S. Zhang and G. M. Jin, Phys. Rev. C **58**, 2283 (1998).

[183] B. A. Li, C. M. Ko and G. Q. Li, Phys. Rev. C **54**, 844 (1996).

[184] S. A. Voloshin, Phys. Rev. C **55**, R1630 (1997).

[185] A. D. Sood and R. K. Puri, Eur. Phys. J. A **30**, 571 (2006).

[186] S. Gautam, A. D. Sood, R. K. Puri and J. Aichelin, Phys. Rev. C **83**, 034606 (2011);

[187] S. Gautam, R. Kumari and R. K. Puri, Phys. Rev. C **86**, 034607 (2012).

[188] A. Jain, K. S. Vinayak and S. Kumar, Ann. of Phys. **334**, 334 (2013).

[189] M. D. Toro *et al.*, Nucl. Phys. A **782**, 267c (2007).

[190] R. Bansal and S. Gautam, Phys. Rev. C **91**, 024615 (2015).

[191] J. W. Negele, Rev. Mod. Phys. **54**, 913 (1982)

[192] F. Sakata *et al.*, Phys. Rev. C **50**, 138 (1994).

[193] D. Lacroix. and P. Chomaz, Phys. Rev. C **58**, 1604 (1998).

[194] A. S. Umar and D. Oberacker, Phys. Rev. C **74**, 024606 (2006)

[195] S. S. Chandel, S. K. Dhiman and R. Shyam, Phys. Rev. C **68**, 054320 (2003).

[196] P. Quentin and H. Flocard, Annu. Rev. Nucl. Sci. **28**, 523 (1978) and references therein.

[197] K. T. R. Davies and S. E. Koonin, Phys. Rev. C **23**, 2042 (1981).

[198] H. Stöcker and W. Greiner, Phys. Rep. **137**, 277 (1986).

[199] H. Sorge, H. Stöcker and W. Greiner, Ann. Phys. (N.Y.) **192**, 266 (1989).

[200] E. Suraud, C. Gregoire and B. Tamain, Prog. Part. Nucl. Phys. **23**, 357 (1989).

[201] J. Cugnon, T. Mizutani and J. Vandermeulen, Nucl. Phys. A **352**, 505 (1981).

[202] Y. Yariv and Z. Fraenkel, Phys. Rev. C **20**, 2227 (1979).

[203] J. Aichelin and H. Stöcker, Phys. Lett. B **176**, 14 (1986).

[204] C. Hartnack *et al.*, Nucl. Phys. A **495**, 303c (1989).

[205] C. Hartnack, J. Aichelin, H. Stöcker and W. Greiner, Phys. Lett. B **336**, 131 (1994).

[206] S. Soff, S. A. Bass, C. Hartnack, H. Stöcker and W. Greiner, Phys. Rev. C **51**, 3320 (1995).

[207] H. Feldmeier and J. Schnack, Prog. Part. Nucl. Phys. **39**, 393 (1997)

[208] H. Feldmeier, Nucl. Phys. A **515**, 147 (1990).

[209] A. Ono, H. Horiuchi, T. Maruyama and A. Ohnishi, Phys. Rev. Lett. **68**, 2898 (1992)

[210] A. Ono and H. Horiuchi, Phys. Rev. C **51**, 299 (1995).

[211] M. Jaminan, C. Mahaux and H. Ngo, Nucl. Phys. A **440**, 228 (1985)

[212] M. Jaminan, C. Mahaux and H. Ngo, Nucl. Phys. A **452**, 445 (1986).

[213] S. W. Huang, Ph. D thesis, Univ. of Tubingen, Tubingen, Germany (1994).

[214] J. Molitoris, J. B. Hoffer, H. Kruse and H. Stöcker, Phys. Rev. Lett. **53**, 899 (1984)

[215] S. M. Kiselew and Y. E. Polrowskil, Sov. Journ, Nucl. Phys. **38**, 46 (1983).

[216] G. Peilert, H. Stöcker, W. Greiner, A. Rosenhauer, A. Bohnet and J. Aichelin, Phys. Rev. **C 39**, 1402 (1989).

[217] A. Bohnet, N. Ohtsuka, J. Aichelin, R. Linden, and A. Faessler, Nucl. Phys. A 494, 349 (1989).

[218] G. Batko, J. Randrup and T. Vetter, Nucl. Phys. A **536**, 786 (1992)

[219] G. Batko, J. Randrup and T. Vetter, Nucl. Phys. A **546**, 761 (1992).

[220] R. K. Puri *et al.*, Phys. Rev. C **54**, R28 (1996).

[221] C. David, C. Hartnack and J. Aichelin, Nucl. Phys. A **650**, 358 (1999).

[222] C. Hartnack Ph.D thesis, GSI- Report 93-5 (1993).

[223] C. Hartnack *et al.*, Phys. Rep. **510**, 119 (2012) .

[224] S. A. Bass, C. Hartnack, H. Stöcker and W. Greiner, Phys. Rev. C **51**, 3343 (1995).

[225] B. J. VerWest and R. A. Arndt, Phys. Rev. C **25**, 1979 (1982).

[226] P. Danielewicz and G. F. Bertsch, Nucl. Phys. A **533**, 712 (1991).

[227] J. Huber and J. Aichelin, Nucl. Phys. A **573**, 587 (1994).

[228] L. Neise, M. Berenguer, C. Hartnack, G. Peilert, H. Stöcker and W. Greiner, Nucl. Phys. A **519**, 375 (1990).

[229] M. Berenguer, C. Hartnack, G. Peilert, H. Stöcker and W. Greiner, J. Phys. G **18**, 655 (1992).

;

[230] J. Singh, S. Kumar and R. K. Puri, Phys. Rev. C **65**, 024602 (2002)

[231] S. Kumar, S. Kumar and R. K. Puri, Phys. Rev. C **78**, 064602 (2008).

[232] S. Kumar, S. Kumar and R. K. Puri, Phys. Rev. C **81**, 014601 (2010).

[233] S. Kumar and R. K. Puri, Phys. Rev. C **58**, 320 (1998).

[234] P. B. Gossiaux and J. Aichelin, Phys. Rev. C **56** 2109 (1997).

[235] J. Pochodzalla *et al.*, Phys. Rev. Lett. **75**, 1048 (1995).

[236] J. K. Dhawan and R. K. Puri, Phys. Rev. C **75**, 057601 (2007).

[237] G. F. Bertsch, H. Kruse and S. Das Gupta, Phys. Rev. C **29** (1984) R673.

[238] M. Colonna *et al.*, Phys. Rev. C **57**, 1410 (1998).

[239] J. Aichelin *et al.*, Phys. Rev. Lett. **62**, 1461 (1989).

[240] Toshiki Maruyama *et al.*, Phys. Rev. C **53**, 297 (1996).

[241] A. Ono *et al.*, Eur. Phys. J. A **30**, 109 (2006).

[242] Liu *et al.*, Chin. Phys. Lett. **20**, 832 (2003).

[243] T. Maruyama, A. Bonasera, M. Papa and S. Chiba, Eur. Phys. J. A **14**, 191 (2002).

[244] D. V. Shetty *et al.*, Phys. Rev. C **76**, 024606 (2007).

[245] K. S. Vinayak and Suneel Kumar, Pramana-J. Phys. **82**, 515 (2014).

[246] J. Singh *et al.*, Phys. Lett. B **519**, 46 (2001).

[247] Yogesh K. Vermani and R. K. Puri, J. Phys. G **36**, 105103 (2009).

[248] Sukhjit Kaur and R. K. Puri, Phys. Rev. C **87**, 014620 (2013) .

[249] A. Sood and R. K. Puri ,Phys. Rev. C **73**, 067602 (2006).

[250] S. Gautam *et al.*, J. Phys. G **37**, 085102 (2010).

[251] R. Bansal it et al., J. Phys. G **41**, 035103 (2014).

[252] Sukhjit Kaur and R. K. Puri, Phys. Rev. C **90**, 037602 (2014).

[253] K. G. R. Doss *et al.*, Phys. Rev. C **37**, 163 (1988).

[254] D. Klakow, G. Welke and W. Bauer, Phys. Rev. C **48**,1982 (1993).

[255] G. D. Westfall *et al.*, Phys. Rev. Lett. **71**, 1986 (1993).

[256] D. J. Magestro, W. Bauer and G. D. Westfall, Phys. Rev. C **62**, 041603(R) (2000).

[257] D. J. Magestro, W. Bauer, O. Bjarki, J. D. Crispin, M. L. Miller, M. B. Tonjes, A. M. Vander Molen, G. D. Westfall, R. Pak, and E. Norbeck, Phys. Rev. C **61**, 021602(R) (2000).

[258] A. Buta *et al.*, Nucl. Phys. A **584**, 397 (1995).

[259] H. Zhou, Z. Li, and Y. Zhuo, Phys. Rev. C **50**, R2664 (1994).

[260] Z. G. Xiao *et al.*, Phys. Rev. Lett. **102**, 062502 (2009)

[261] Wein-Mei Guo, Gao-Chan Young and Wei Zuo, Phys. Rev. C **90**, 044605 (2014).

[262] Jian-Ye Liu *et al.*, Phys. Lett. B **540**, 213 (2002).

[263] Hajime Sotani *et al.*, Phys. Rev. C **91**, 015805 (2015).

[264] N. Wang *et al.*, Phys. Rev. C **91**, 044308 (2015).

[265] B. A. Li *et al.*, Phys. Rev. C **91**, 044601 (2015).

[266] B. A. Li, L. W. Chen and C. M. Ko, Phys. Rep. **464**, 113 (2008).

[267] K. S. Vinayak and Asis K. Chaudhari, J. Phys. G **42**, 025108 (2015).

[268] J. Singh, S. Kumar and R. K. Puri, Phys. Rev. C **63**, 054603 (2011)

[269] M. B. Tsang *et al.*, Prog. Part. Nucl. Phys. **66**, 400 (2011)

[270] K. S. Jeong and S. H. Lee, Nucl. Sci. Tech. **24**, 050506 (2013)

[271] M. B. Tsang *et al.*, Phys. Rev. C **86**, 015803 (2012).

[272] M. D. Cozma *et al.*, Phys. Rev. C **88**, 044912 (2013).

[273] P. Russotto *et al.*, Eur. Phys. J. A **50**, 38 (2014).

[274] W. Trautmann and H. H. Wolter, arXiv:1712.03093.

[275] A. Kaur, Deepshikha, K. Vinayak and Suneel Kumar, Phys. Atomic. Nucl. **79**, 474 (2016).

[276] K. S. Vinayak and Suneel Kumar, Jour. of Phys. Conf. Series **381** 012032 (2012).

[277] K. S. Vinayak and Suneel Kumar, Phys. Part. Nucl. Lett. **9** 583 (2012).

[278] W. M. Guo, G. C. Yong and W. Zuo, Phys. Rev. C **90**, 044605 (2014).

[279] M. B. Tsang *et al.*, Phys. Rev. C **71**, 1502 (1993).

[280] D. V. Shetty, S. J. Yenello and G. A. Souliotis, Phys. Rev. C **76**, (2007) 034602.

[281] Y. K. Vermani, S. Goyal and R. K. Puri, Phys. Rev. C **79**, 064613 (2009).

[282] C. Sfienti *et al.*, Phys. Rev. Lett. **102**, 152701 (2009).

[283] J. M. Lattimer and M. Prakash, Phys. Rep. **442**, 109 (2007).

[284] J. M. Lattimer and M. Prakash, Science **304**, 536 (2004).

[285] M. Prakash *et al.*, Phys. Rep. **280**, 1 (1997).

[286] J. M. Lattimer and M. Prakash, Phys. Rep. **333**, 121 (2000).

[287] E. Khan *et al.*, Phys. Rev. C **82**, 024322 (2010).

[288] T. Li *et al.*, Phys. Rev. C **81**, 034309 (2010).

[289] C. Xu, B. A. Li and L. W. Chen, Phys. Rev. C **82**, 054607 (2010).

[290] Y. Zhang *et al.*, Phys. Lett. B **664**, 145 (2008).

[291] M. B. Tsang *et al.*, Phys. Rev. Lett. **102**, 122701 (2009).

[292] P. Russotto *et al.*, Phys. Lett. B **697**, 471 (2011).

[293] J. Singh and R. K. Puri, J. Phys. G **27**, 2091 (2001).

[294] K. Amandeep and K. Suneel, Indian J. Phys. **91**, 1095 (2017).

[295] M. Di Toro *et al.*, J. Phys. G **37**, 083101 (2010).

[296] Kamaldeep Kaur and Suneel Kumar, Nucl. Phys. A **973**, 149 (2018).

[297] D. V. Shetty *et al.*, Nucl. Instrum. Methods Phys. Res. B **261**, 990 (2007).

[298] M. H. Zhao *et al.*, Phys. Rev. C **89**, 037001 (2014).

[299] W. H. Dickhoff and D. Van Neck, Many-Body Theory Exposed (World Scientific, Singapore, 2005), 1st ed.

[300] J. N. Ginnochio, Phys. Rev. C **17**, 195 (1978).

[301] A. Nadasen *et al.*, Phys. Rev. C **23**, 1023 (1981).